LBL-1876

c.2

I. GENERATION OF FAR-INFRARED RADIATION BY OPTICAL RECTIFICATION OF PICOSECOND LIGHT PULSES AND BY MIXING OF TWO TUNABLE DYE LASERS
II. THEORETICAL STUDY OF COHERENT PHONON GENERATION BY OPTICAL MEANS IN A ONE-DIMENSIONAL SUPERLATTICE

Kei-Hsiung Yang
(Ph. D. thesis)

December, 1974

Prepared for the U. S. Atomic Energy Commission
under Contract W-7405-ENG-48

TWO-WEEK LOAN COPY

This is a Library Circulating Copy
which may be borrowed for two weeks.
For a personal retention copy, call
Tech. Info. Division, Ext. 5545

LAWRENCE BERKELEY LABORATORY
UNIVERSITY OF CALIFORNIA
BERKELEY

LBL-1876

c.2

DISCLAIMER

This document was prepared as an account of work sponsored by the United States Government. While this document is believed to contain correct information, neither the United States Government nor any agency thereof, nor the Regents of the University of California, nor any of their employees, makes any warranty, express or implied, or assumes any legal responsibility for the accuracy, completeness, or usefulness of any information, apparatus, product, or process disclosed, or represents that its use would not infringe privately owned rights. Reference herein to any specific commercial product, process, or service by its trade name, trademark, manufacturer, or otherwise, does not necessarily constitute or imply its endorsement, recommendation, or favoring by the United States Government or any agency thereof, or the Regents of the University of California. The views and opinions of authors expressed herein do not necessarily state or reflect those of the United States Government or any agency thereof or the Regents of the University of California.

I. GENERATION OF FAR-INFRARED RADIATION BY OPTICAL RECTIFICATION OF PICOSECOND LIGHT PULSES AND BY MIXING OF TWO TUNABLE DYE LASERS
II. THEORETICAL STUDY OF COHERENT PHONON GENERATION BY OPTICAL MEANS IN A ONE-DIMENSIONAL SUPERLATTICE

Contents

Abstract v

Chapter I

I. Introduction 1

II. Generation of Far-Infrared Radiation by Picosecond Light Pulses in $LiNbO_3$ 7

A. Theory 7

B. Experiments and Results 13

C. Conclusions and Discussions 20

III. Phase-Matched Far-Infrared Generation by Mixing Two Dye Lasers . 23

A. Theory 23

1. Double Refraction 25

2. Boundary Conditions 26

3. Effects of Finite Beam Cross Section, Divergence, and Diffraction 28

4. Finite Far-Infrared Linewidth 29

5. The Dispersions of the Dielectric Constant and the Second Order Nonlinear Susceptibility 30

B. Experimental Techniques 35

1. Dual-Frequency One Dye Cell Scheme 35

2. Two-Dye-Cell Scheme 37

3. Far-Infrared Detection 39

4. Crystal Preparation 43

5. Phase-Matching Methods 44

C. Results of Experiments and Comparison with Theory 44

D. Conclusions and Discussions 53

1. Conclusions 53

2. Discussion 54

Chapter II

I. Introduction 65

II. First Order Interaction via Piezoelectric Effects 68

III. Second-Order Interaction via Electrostrictive Couplings 76

IV. Discussions and Conclusions 78

Acknowledgements 82

Appendix 83

A. Calculation of Fabry-Perot Interference Fringes 83

B. The Dispersion of $\chi^{(2)}$ 85

C. Phonon Generation via Piezoelectric Constants in a Superlattice 90

D. Phonon Generation via Electrostrictive Coupling in a Superlattice 91

References 120

Figure Captions 127

Figures 132

CHAPTER I

GENERATION OF FAR-INFRARED RADIATION BY OPTICAL RECTIFICATION OF PICOSECOND LIGHT PULSES AND BY MIXING OF TWO TUNABLE DYE LASERS

Kei-Hsiung Yang

Inorganic Materials Research Division, Lawrence Berkeley Laboratory
and Department of Physics; University of California
Berkeley, California

ABSTRACT

We have observed far-infrared radiation generated in a $LiNbO_3$ crystal by picosecond light pulses from a mode-locked Nd: glass laser. The output spectra were analyzed by a Michelson interferometer and a Fabry-Perot interferometer. In one experiment a 0.77 mm thick $LiNbO_3$ crystal was used to rectify the laser pulses. The resulting spectrum showed peaks of descending power at 2, 6.5, and 10.5 cm^{-1}. This shape can be roughly understood as the product of an ω^2 radiation efficiency, a phase-matching curve centered at zero frequency, and a Gaussian envelope corresponding to a 1.8 picosecond laser pulsewidth. In a second experiment the $LiNbO_3$ was oriented to obtain forward phase-matching at 13.5 cm^{-1} and backward phase-matching at 6.5 cm^{-1}. Both peaks were observed and were in agreement with the theoretical calculation. The far-infrared power observed in the rectification case was about 200W for a peak laser power density of 0.2GW/cm^2 and a train of 30 pulses. We also used dual-frequency dye laser systems to generate continuously tunable far-infrared radiation from 20 to 190 cm^{-1}. We have investigated both the collinear (forward and backward) and non-collinear phase-matching in $LiNbO_3$ over most of this frequency range

and the forward collinear phase-matching in ZnO, ZnS, CdS, and CdSe at selected frequencies. We measured the generated far-infrared power versus frequency in $LiNbO_3$ as well as the far-infrared linewidth of 3 cm^{-1}. We also obtained the absorption constant of the far-infrared O-ray in $LiNbO_3$ from the phase-matching curves. We deduced the dispersion of $\chi_{24}^{(2)}$ in $LiNbO_3$ from the experiment which agreed well with the theoretical calculation. A plane wave theory using the Green's function method was developed to explain the spectra obtained in the picosecond pulse experiments. This plane-wave approximation was then modified to calculate the far-infrared power produced by mixing two dye lasers in $LiNbO_3$ in both collinear and non-collinear phase-matching schemes.

CHAPTER II

THEORETICAL STUDY OF COHERENT PHONON GENERATION BY OPTICAL MEANS IN A ONE-DIMENSIONAL SUPERLATTICE

ABSTRACT

With the help of the lattice momentum, phase-matched optical generation of coherent phonons with frequencies higher than 50 GHz appears feasible. We have calculated two cases: (i) Direct conversion of millimeter or submillimeter photons in a piezoelectric superlattice, (ii) Optical mixing of two laser beams in a non-piezoelectric superlattice. In the first case, an efficiency of 10^{-4} for photon-to-phonon power conversion can be achieved using an epitaxial GaAs:GaP superlattice of 100 unit cells. The piezoelectric superlattices can be constructed

from multilayer epitaxially grown crystals, partially oriented sputtered films, and naturally grown polytypic crystals. In the second case, longitudinal phonon power of 1 mW can be generated by the mixing of two 10 MW/cm^2-laser beams in a KCl:CdS superlattice of 100 vacuum deposited layers. We have also calculated the first-order effect on the generated phonon power due to ±2% random errors in the periodicity of the superlattice. In both cases, the high-order unklapp processes which involve shorter phonon wavelengths are most sensitive to such imperfection. In both cases, the acoustic power generated under phase-matching conditions is proportional to the square of the total number of unit cells in the superlattice.

CHAPTER I

I. INTRODUCTION

Since Zernike and Berman[1] observed radiation near 100 cm^{-1} resulting from the mixing of unknown number of modes from a single pulsed neodymium glass laser in crystal quartz, many groups have been trying to achieve tunable far-infrared (FIR) radiation by mixing two lasers in different non-linear crystals. We can classify all of this work into three categories according to the type of lasers used for the experiments. In the first category, two CO_2 gas lasers were used to mix in various semiconductors. Zernike[2] and Van Tran and Patel[3] reported the generation of radiation in the 100 cm^{-1} range by mixing the 9.6μ and 10.6μ CO_2 laser transition in InSb. Recently, quite a few experiments belonging to this category have been conducted.[4-9] One interesting experiment was done by Van Tran Nguyen and Bridges[8] who used the n-type InSb at 15°K in a strong magnetic field as a mixing crystal. The enhancement of the second-order resonant optical nonlinearity due to conduction-electron spins was observed. Boyd, Bridges, Patel, and Buehler[7] used $ZnGeP_2$ as a mixing crystal to produce phase-matched step-wise tunable radiation from 70 to 110 cm^{-1}. Recently, Aggarwal, Lax, and Favrot[9] reported the noncollinear phase-matching in GaAs to produce step-wise (0.1 cm^{-1}) tunable far-infrared radiation. In the second category of experiments, two solid state lasers were used. The first observation of the continuously tunable FIR radiation was reported by Faries, Gehring, Richards, and Shen.[10] In this experiment, two R_1 ruby lasers with one of the laser rods cooled were mixed in $LiNbO_3$ to produce radiation in the frequency range from 1.2 to 8.1 cm^{-1}. Later,

by mixing a R_1 ruby laser with a R_2 ruby laser (temperature cooling in either of the laser rods), a continuously tunable radiation from 20 to 38 cm^{-1} was achieved. The third category was the experiments of mixing two dye lasers. Yang, Morris, Richards, and Shen[11] reported the generation of the continuously tunable radiation from 20 to 190 cm^{-1} by mixing two dye lasers in $LiNbO_3$ and ZnO. Auston, Glass, and LeFur[12] also observed tunable radiation from 2 to 50 cm^{-1} using a reduced (black) $LiNbO_3$ as a mixing crystal.

There are two main reasons for attempting to generate tunable far-infrared radiation by mixing two laser beams. First, it offers the possibility of providing a useful source to do spectroscopy in the far-infrared region. Second, it provides understanding of the nonlinear interaction of the electromagnetic radiation with matter.

Exploratory spectroscopic studies in the region between 3 and 200 cm^{-1} began more than 50 years ago, but the development has lagged well behind that in other parts of the spectrum by the lack of suitable bright source.[13] Electron beam devices such as klystrons, back wave oscillators,[14] etc., can generate coherent narrow line-width radiation with limited tunability which is useful for the high resolution spectroscopy below 25 cm^{-1}. By using harmonic generation,[14] this radiation source can be extended to higher frequencies with a great loss of efficiency. On the other hand, the grating spectrometer and the Michelson interferometer,[15] both with a hot black body as a radiation source, are used for higher frequencies.

The most widely-used far-infrared source in the Michelson interferometer is the Rayleigh-Jeans region of the black body spectrum

emitted by a high pressure mercury arc lamp. The intensity of the radiation emitted by the lamp varies approximately by two, and the total power radiated by the lamp used in our laboratory into the 1:1.5 optics of the Michelson interferometer, in the region 0-100 cm^{-1}, is 2×10^{-5} W, while in the region 0-30 cm^{-1} is of the order 10^{-8} W. The newly invented polarization interferometer[16,17] has improved the 0-100 cm^{-1} region because the grid beam splitters of high efficiency are used. The lack of energy of the source limits the resolution or lengthens the measuring time for a reasonable signal-to-noise ratio. For comparison, the far-infrared peak power per unit frequency over the region 0-100 cm^{-1} generated by mixing two dye lasers is three to four orders of magnitude larger than that produced by a mercury arc lamp. High peak powers are necessary in order to investigate transient and nonlinear phenomena in the far-infrared region, and also possibly, in using room temperature detectors.

In choosing a spectroscopic technique for a particular application, several major considerations must be weighted against each other, including in particular, the spectral resolution required, the range of frequency to be scanned, the time available for recording, the ease of operation, and the expense or availability of the components. The recent development of small compact digital computers, which can be interfaced to compute the spectrum from the interferogram has increased the usefulness of the Michelson interferometer and the polarization interferometer. They have the advantages of a reasonably good resolution, a broad range of frequency scanning, and a fast speed of measurements.[15] They have become the most frequently used tool for the

spectroscopical investigation in the far-infrared region. At the present stage, tunable far-infrared radiation by mixing two laser beams in nonlinear crystals can not compete with the Fourier transform spectroscopy as a spectroscopic tool. Much engineering effort is needed before it can be put into practical usage. However, in the long run, with further engineering development, it might become cheaper in construction, easier in operation, and better in resolution than the Michelson interferometer.

In this thesis, we will describe two experiments related to the tunable far-infrared generation by mixing two lasers in nonlinear crystals. In the first experiment,[18] mode-locked picosecond pulses which have broad spectral contents were mixed in $LiNbO_3$ (a birefringent crystal). We first derive a theoretical description using a Green's function method in the plane-wave approximation. We calculate the far-infrared power spectrum produced for two different crystal orientations. When the picosecond optical field is parallel to the c-axis and the two surfaces of a crystal slab, the resulting spectrum can be understood as the product of an ω^2 radiation efficiency, a phase-matching factor centered at zero frequency, and a Gaussian pulse frequency envelope. When the c-axis of the crystal tilts at an angle away from the normal of the crystal slab, and the optical field propagates along that normal with equal components in the ordinary and extraordinary rays, the resulting spectrum shows two different phase-matching peaks, one forward and the other backward, multiplied by ω^2 and Gaussian pulse envelope. We then describe the experimental arrangements. The far-

infrared signals was separated into two beams, one for normalization, the other passing through a Michelson interferometer[20] for spectral analysis. Interferograms were Fourier transformed to obtain the far-infrared spectra. We then discuss the agreement between the experimental results and the simple theoretical calculations in general shapes of the spectra, the exact locations of peaks and valleys, and the phase-matching frequencies. We fit our experimental results with Gaussian laser pulse length of 1.8 or 2.3 picoseconds, which differs from the two-photon fluorescence measurement of 5 picoseconds. We explain this discrepancy and compare with other picosecond optical pulse experiments in the discussion.

In the second experiment,[21] a dual-frequency dye laser system was used to generate continuously tunable radiation over the frequency range from 20 to 160 cm^{-1} in $LiNbO_3$ and at selected frequencies in ZnO, ZnS, CdS, and CdSe. Phase-matching was achieved by using the birefringent crystals in the collinear scheme and by forming a closed triangle with three wavevectors in the noncollinear scheme. Although many experiments have been done in mixing two laser beams to generate difference frequency radiation, a complete detailed theoretical description of the physical process, including the use of focusing lenses, is still not available. In principle, such a description should be possible if not too tedious and time consuming, given the temporal and spatial behavior of the two input laser beams, the frequency dependent dielectric constants, and the nonlinear coefficients of the mixing crystal. Unfortunately, in our experiments of mixing two dye

lasers, the transverse modes of the laser beams are not known, making the exact theoretical description almost impossible. Hence, in this thesis, we try to calculate the far-infrared power generated under collinear and noncollinear phase-matched schemes using the Green's function method in the plane wave approximation. We then discuss the effects on the far-infrared power of the following factors which are relevant to our experimental conditions: the double refraction, boundary conditions, finite beam cross-section, laser divergence, far-infrared diffraction, finite far-infrared linewidth, and the dispersions of the dielectric constant and the second order nonlinear susceptibility. The derivations of the formulas showing the dispersion of the second-order nonlinear susceptibility are included in Appendix B. We then describe our experimental techniques, one-dye cell dual-frequency scheme, two-dye cell schemes, far-infrared detection, the crystal preparations, and phase-matching methods in detail. After summarizing the experimental results, we show the comparisons between theoretical and experimental results for the far-infrared power generated by collinear and noncollinear phase-matching schemes, in the far-infrared O-ray absorption constants, and in the dispersion of $\chi_{24}^{(2)}$ for $LiNbO_3$. We also show that the formulas used to calculate the dispersion of $\chi_{24}^{(2)}$ in $LiNbO_3$ can be generalized to calculate the dispersion of the nonlinear susceptibility in InSb (free electrons in magnetic field) and CoF_2 (magnon mode).

II. GENERATION OF FAR-INFRARED RADIATION BY PICOSECOND LIGHT PULSES IN $LiNbO_3$

A. Theory

From the uncertainty principle $\Delta\nu\tau \sim 1$, a one picosecond mode-locked optical pulse should contain a bandwidth of 33 cm^{-1}. Because of its broad spectral content, a picosecond laser pulse can generate far-infrared radiation in a nonlinear crystal as a result of beating between its various frequency components. Theoretically, Gustafson et al.[22] have investigated the interaction of intense picosecond pulses with electro-optical material. They have calculated the rectified field for an infinite plane wave, in the limit that the optical and far-infrared phase velocities differ negligibly. The difference in phase velocities is important in explaining the power spectrum of the generated far-infrared, as later verified by the experimental results. In their calculations, the reflection and refraction at the crystal boundaries was also neglected. Later, Morris and Shen[23] carried out a more realistic calculation which included the various effect due to a finite beam cross section, crystal boundaries, and the significantly different optical and far-infrared phase velocities. In order to compare with the experimental results, they calculated numerically the results of rectification of the mode-locked Nd:glass laser pulses in $LiNbO_3$. Two different phase-matching conditions were investigated. In the first case, when the optical field was an extraordinary ray (e-ray), the generated far-infrared radiation propagated also as an e-ray. In this case, the nonlinear coefficient $\chi_{33}^{(2)}$ was responsible

for the far-infrared generation (phase-matched at zero frequency). In the second case, the optical field had equal components in the e-ray and the ordinary ray (o-ray). The generated far-infrared was in the o-ray and the nonlinear coefficient $\chi_{24}^{(2)}$ was mainly responsible for this process (phase-matched at finite frequency). In this section, a very simple theoretical calculation plus some intuitive physical arguments which are believed to be adequate to explain the experimental results will be described. For the complete detailed theoretical calculations refer to reference 24.

Assuming a monochromatic electromagnetic wave in an insulator, Maxwell's equations reduce to the wave equation[25]

$$\underset{\sim}{\nabla} \times (\underset{\sim}{\nabla} \times \underset{\sim}{E}) - \frac{\overleftrightarrow{\varepsilon}}{c^2} \frac{\partial^2 E}{\partial t^2} = - \frac{4\pi}{c^2} \omega^2 \underset{\sim}{P}^N \qquad (1)$$

where $\overleftrightarrow{\varepsilon}$ is the dielectric constant tensor and $\underset{\sim}{P}^N$ is the nonlinear polarization resulting from the nonlinear coefficient of the material. In the case of the picosecond optical pulses propagating in a $LiNbO_3$ crystal, one can study most simply the collinear propagation of the rectified and optical fields neglecting the radial profiles of both. Assuming that the depletion of the input optical pulse is negligible, the rectified field produced in the case of phase-matching at zero frequency is governed by the equation

$$\left[\frac{\partial^2}{\partial z^2} - \frac{1}{\nu_{3e}^2} \frac{1}{\partial t^2} \right] E_{3e}(z,t) = \frac{4\pi}{c^2} \frac{\partial^2}{\partial t^2} P_3^N (z,t) \qquad (2)$$

where $\nu_{3e} = \frac{c}{n_{3e}}$ is the difference frequency phase velocity, n_{3e} is the far-infrared e-ray index of refraction. No dispersion for n_{3e}

is understood since the frequency of the rectified field is below 20 cm^{-1}, where, as in $LiNbO_3$, the lowest frequency polariton mode[26] for e-ray is at 248 cm^{-1}. The propagation direction is along z-axis, as is the $\hat{c}$-axis of the $LiNbO_3$ crystal.

Furthermore, we can write

$$P_3^N(z,t) = \chi_{33}^{(2)} E_e E_e^* \tag{3}$$

where E_e denotes the laser field in the e-ray. The causal Green's function for Eq. (2) is

$$G(z-z',t-t') = -\frac{\nu_{3e}}{2} H\left(t-t' - \frac{1}{\nu_{3e}}|z-z'|\right) \tag{4}$$

where $H(\xi)$ is the heavyside function such that

$$H(\xi) = 0 \quad \text{for } \xi < 0$$

$$= 1 \quad \text{for } \xi > 0$$

The solution for the rectified field can be written as

$$E_{3e}(z,t) = \frac{\nu_{3e}}{2}\frac{4\pi}{c^2}\int_0^{\ell} dz' \int_{-\infty}^{\infty} dt' \frac{\partial^2}{\partial t'^2} P_3^N(z',t') H\left(t-t' - \frac{1}{\nu_{3e}}|z-z'|\right) \tag{5}$$

In the formula (5), the crystal slab is assumed to lie between $z=0$ and $z=\ell$, and the refraction and reflection from the crystal boundaries is neglected. For $z \geqslant \ell$, Eq. (5) becomes

$$E_{3e}(z,t) = \frac{2\pi}{n_{3e}c}\int_0^{\ell} dz' \frac{\partial}{\partial t} P_3^N\left(z', t - \frac{1}{\nu_{3e}}(z-z')\right) \tag{6}$$

A formula for the frequency spectrum of the far-infrared electric field is easily obtained by the Fourier transformation of Eq. (6).

$$\mathcal{E}_{3e}(z,\omega) = \frac{1}{\sqrt{2\pi}} \int_{-\infty}^{\infty} dt\, e^{i\omega t}\, E_{3e}(z,t) \tag{7}$$

Equations (3), (6), and (7) indicate that if the exact expression for $\chi_{33}^{(2)}(\omega)$ and the laser optical field E_e are known, one can calculate the power spectrum of the rectified field. We assume no dispersion for $\chi_{33}^{(2)}(\omega)$ and n_{3e} for $\omega < 20\ cm^{-1}$ (this is true since the lowest frequency polariton mode affects most of the dispersion of $\chi_{33}^{(2)}(\omega)$ is at 248 cm^{-1}) and that the laser optical pulse takes the Gaussian form

$$E_e = \mathcal{E}_e \exp[-(\frac{n_e z}{c} - t)^2/2\sigma^2]\exp[i(\frac{n_o\omega_o}{c} z - \omega_o t)] \tag{8}$$

where $\mathcal{E}_e$ denotes the complex amplitude, n_e is the index of refraction for the e-ray laser field, σ is a parameter related to the optical pulse-width and ω_o is the laser pulse central frequency. Substituting Eq. (8) into Eq. (3), then using Eqs. (6) and (7), we obtain the power spectrum of the rectified field by a single picosecond optical pulse as

$$S_{3e}(\omega) = \frac{cn_{3e}}{4\pi}\ \mathcal{E}_{3e}(z,\omega)\mathcal{E}_{3e}^*(z,\omega)$$

$$= \frac{\pi\omega^2\sigma^2}{4n_{3e}c}\ |\mathcal{E}_e|^4 |\chi_{33}|^2\, e^{\frac{-\sigma^2\omega^2}{2}}\ \ell^2\ \frac{\sin^2(\frac{k\ell}{2})}{(\frac{k}{2}\ \ell)^2} \tag{9}$$

In deriving Eq. (9), we assume that the condition $\alpha\ell \ll 1$ is valid where ℓ is the thickness of crystal and α is the far-infrared e-ray absorption constant. Also, in Eq. (9), k equals $\frac{\omega(n_{3e}-n_e)}{c}$, where

ω is the far-infrared frequency. It can be seen from Eq. (9) that the far-infrared power spectrum depends on the square of both the input laser power and the nonlinear coefficient, on the dipole radiation efficiency ω^2, on the coherent far-infrared phase-matching factor $[(\sin^2 k\ell/2)/(k\ell/2)^2]$ which is centered at zero frequency and on the optical pulse envelope $e^{-\omega^2\sigma^2/2}$.

Although the experimental observation was of the sum of a picosecond pulse train instead of a single pulse, the general shape of this power spectrum was verified.

In the case of phase matching at finite frequencies, the $\hat{c}$ axis of the crystal slab is tilted away from the z-axis with an angle θ. If one neglects the so-called "walk-off" effect of the laser e-ray, Eqs. (2), (4), (5), (6), (7) are valid with the subscript e changed to o to indicate that it is the far-infrared o-ray which is generated. Equation (3) should then be replaced by

$$P_3^N(z,t) = \chi_{eff} E_o E_e^* \tag{10}$$

where E_e is expressed as in Eq. (8) and E_o, the laser o-ray, can be written as

$$E_o = \mathcal{E}_o \exp[-(\frac{n_o z}{c} - t)^2/2\sigma^2] \exp[i(\frac{n_o \omega_o}{c} z - \omega_o t)] \tag{11}$$

where $\mathcal{E}_o$ is the amplitude and n_o is the laser o-ray index of refraction. Carrying out the calculation as in the first case (for simplicity, we substitute Eq. (6) into Eq. (7) and integrate with respect to dt first), we obtain for $z \geqslant \ell$

$$E_{3o}(z,\omega) = \frac{-i\pi\omega\sigma}{n_{3o}c}\chi_{eff}E_oE_e^* e^{\frac{-\omega^2\sigma^2}{4}} e^{i\frac{\omega}{v_{3o}}z} * \int_0^{\ell} e^{i\Delta k_+ z'} \cdot e^{\frac{-z'^2(n_o-n_e)^2}{4\sigma^2c^2}} dz' \tag{12}$$

and

$$\Delta k_+ = (n_o-n_e)\frac{\omega_o}{c} - (n_{3o}-\bar{n})\frac{\omega}{c}\ ; \quad \bar{n} = \frac{n_o+n_e}{2} \tag{13}$$

If the difference in the optical path of the laser o-ray and e-ray after passing through the crystal slab is much less than the optical pulse length, i.e. $\frac{\ell(n_o-n_e)}{2\sigma c} << 1$ (as is true for a few mm $LiNbO_3$ crystal slab), then Eq. (12) can be simplified as

$$E_{3o}(z,\omega) = -\frac{i\pi\omega\sigma}{n_{3o}c}\chi_{eff}\cdot E_oE_e^* e^{\frac{-\omega^2\sigma^2}{2}} e^{i(\omega/v_{3o})z} \frac{e^{i\Delta k_+\ell}-1}{i\Delta k_+} \tag{14}$$

The power spectrum for $z \geqslant \ell$ can be expressed as

$$S_{3o}(\omega) = \frac{\pi\omega^2\sigma^2}{4n_{3o}c}|\chi_{eff}|^2 \times |E_o|^2|E_e|^2 e^{\frac{-\omega^2\sigma^2}{2}} \frac{\sin^2(\frac{\Delta k_+}{2}\ell)}{(\frac{\Delta k_+}{2}\ell)^2} \cdot \ell^2 \tag{15}$$

Comparing Eq. (15) with (9), we can conclude that in the case of the laser o-ray beating with e-ray, the phase-matching factor centers at finite frequency instead at zero frequency. However, so far in both cases, we have only solved the forward propagating far-infrared radiation ($z \geqslant \ell$). The Green's function in Eq. (4) implies that there also exist the solutions for the backward propagating far-infrared radiation ($z \leqslant 0$). We can easily follow the mathematical formulas and solve for the condition $z \leqslant 0$. In the case of phase-matching at zero

frequency, the calculated power spectrum has exactly the same formula as the Eq. (9). But in the case of phase-matching at finite frequency, Δk_+ in Eq. (15) changes to Δk_-, where

$$\Delta k_- = (n_o - n_e) \frac{\omega_o}{c} + (n_{3o} - \bar{n}) \, \omega/c \tag{16}$$

Thus, the backward and forward phase-matching frequencies do not coincide. Since in $LiNbO_3$ $n_{3o} = 6.6$ yields far-infrared reflectivity of 54% at the crystal boundaries, this backward phase-matching wave is reflected from the back surface of the crystal and detected by the far-infrared detector. In $LiNbO_3$ crystal, the forward phase-matching frequency is about twice the backward phase-matching frequency in magnitude. Experimentally, both are observed and agree well with the theoretical calculation.

B. Experiments and Results

The experimental scheme is shown in Fig. 1. A Nd:glass laser simultaneously Q-switched and mode-locked by a Kodak 9470 dye solution was used as an exciting source. A Brewster-angle-cut laser rod 0.95 cm in diameter and 10 cm long was placed in a 85 cm long laser cavity. Two externally triggered linear lamps housed in a double ellipse reflector were used to achieve the population inversion for the laser action. The window of the dye cell made an angle of about 60° with respect to the optical axis of the cavity. An adjustable circular aperture was inserted into the cavity to maintain good laser transverse modes. The output was obtained through a 70% reflecting mirror and was monitored by a biplanar vacuum photo-diode combined with a Tektronix 519 oscilloscope which triggered a type 556 oscilloscope.

A Nichol-prism polarizer was used to purify the laser polarization. The mode-locked laser output consisted of a train of about 30 pulses between the half-power points of the envolope with 6-nsec separation between pulses. The total energy contained in the pulse train was about 20 mJ. The pulse width measured with two-photon fluorescence techniques[27,28] was about 5 psec. A lense with a 30 cm focal length was used to focus the laser beam into the $LiNbO_3$ crystal which was 26 cm from the lense, and 1 mm of black polyethylene was used at the output to prevent laser light from reaching the far-infrared detector. The far-infrared output was then split into two beams by a Mylar beam splitter. One of the beams was used for spectral analysis in either a Michelson interferometer[15,19] (see Fig. 2) or a metal-mesh Fabry-Perot interferometer[20] (see Fig. 3). The other was used for normalization. The entire far-infrared system was evacuated to avoid water-vapor absorption. The two beams were separately detected by two n-type InSb (Putley) detectors[29] operated at 1.50±0.05°K[30] in a magnetic field of 5.4 kG. These two detector sizes were 5×4×2 mm and 7×4×1.5 mm respectively and were cut from the same boule, which had a carrier density of about $7\times10^{13}/cm^3$ and a mobility of 7×10^5 cm^2/vsec measured at 77°K. The detector system is shown in Fig. 4. Both detectors were biased with a constant voltage of 0.2 V and the current of each detector was measured using an operational amplifier with a feedback resistor R_F = 205 kΩ [see Fig. 5(b)]. The response time of this system was 2 μsec. The sensitivity of the detector was measured using a blackbody at 200°C and a filter passing 0-50 cm^{-1}. This showed

the average noise equivalent power in a 5×10^5 Hz bandwidth to be 1×10^{-6} W. However, since the sensitivity is certainly not uniform in this energy region[29,31] and since there are inevitable local system resonances at these long wavelengths, the absolute values of the far-infrared power may be in error by as much as an order of magnitude.

Measurements with the Michelson Interferometer

The Michelson interferometer used in the experiments is shown in Fig. 2. It had a 5 mil mylar beam splitter. The chopped mercury arc lamp source which we assume to have a blackbody spectrum was used to measure the instrumental function of the system[15,19] (the spectral sensitivity of the spectrometer-detector combination). For this measurement, the detector signal passing through a lock-in amplifier was recorded by a digital data recording system.[19] The interferograms[19] were measured. The instrumental function was obtained from the Fourier transform of the interferogram, corrected for the assumed blackbody spectrum of the mercury lamp source. The same source was also used to align the Michelson interferometer and locate the zero of path difference.[15,19] To measure the spectra of the laser mixing experiments, the arm containing the chopper and the mercury arc lamp was removed from the Michelson interferometer and replaced by a 9-inch collecting brass tube and the polyethylene lens similar to the output arm of the Michelson interferometer. After the laser was fired, the two far-infrared signals detected were displayed on a Tektronix 556 dual beam oscilloscope and photographed. The ratio of the two signals was then computed. To obtain the true spectrum from the Michelson

interferogram, the Fourier transformation of the interferogram was divided point by point by the instrumental function with the same resolution.

Two crystal orientations were studied. In the first, a 0.775-mm thick $LiNbO_3$ crystal was oriented with the normally incident laser beam polarized along the $\hat{c}$-axis and propagating along $\hat{b}$. In this configuration, the nonlinear susceptibility $\chi_{33}^{(2)}$ (= 3.14×10^{-6} esu)[32] contributes to the generation of far-infrared polarized along $\hat{c}$, and phase-matching occurs at zero difference frequency as the simple theory shows. The Michelson interferometer was used to investigate the far-infrared spectrum. The interferogram was sampled at intervals of 0.2 mm out to a maximum of 5 mm, which limited the resolution[15,19] to 2 cm^{-1}. Four laser shots were averaged for each sample. The final spectrum computed with linear apodization[15] and corrected by the instrumental function is shown in Fig. 6(a). Because of the frequency-dependent reflection coefficient of the 5-mil mylar beam splitter[15] in the Michelson interferometer, the reliable range of the spectrum measured was from 3 to 22 cm^{-1}. The resulting spectrum contains peaks at 2.5, 6.5, and 10.5 cm^{-1} with descending amplitude. The general shape of the spectrum and the exact location of the peaks and valleys agreed well with the simple theoretical calculation using Eq. (9). In this calculation, the far-infrared index of refraction measured by Bosomworth[33] and the optical refractive indices of Boyd, etc.,[34] were used. A more detailed theoretical calculation[23] including the effects of finite beam cross section and reflection and refraction from the crystal boundaries and

assuming a 1.8-psec Gaussian laser pulse is shown in Fig. 6(a) for comparison. The agreement is good.

In the second case, a 1.524-mm-thick $LiNbO_3$ crystal was oriented with its $\hat{c}$ axis tilted at $\theta = 16°$ away from the normal to the plane surfaces and the $\hat{a}$ axis at an angle ϕ from the plane containing the normal and the $\hat{c}$ axis. The normally incident laser beam was polarized to have equal components in the ordinary and extraordinary rays. In this configuration, the polarization responsible for the ordinary ray far-infrared generation can be written as

$$P_{Do} = [\chi_{24}^{(2)}\sin\theta + \chi_{22}^{(2)}\sin 3\phi\cos\theta]E_oE_e + \frac{\chi_{22}^{(2)}}{2}\cos^2\theta\cos 3\phi E_e^2 - \frac{\chi_{22}^{(2)}}{2}\cos 3\phi E_o^2 \tag{17}$$

where $\chi_{24}^{(2)} = 3.08\times10^{-6}$esu, $\chi_{22}^{(2)} = 4.4\times10^{-7}$esu,[32] E_o and E_e are laser o-ray and e-ray components respectively. The polarization responsible for the generation of the far-infrared takes the form

$$\begin{aligned} P_{De} = {} & \chi_{22}^{(2)}\cos^2\theta\cos 3\phi E_oE_e \\ & + (\chi_{24}^{(2)}\cos^2\theta\sin\theta - \frac{\chi_{22}^{(2)}}{2}\sin 3\phi\cos^3\theta + \frac{\chi_{31}^{(2)}}{2}\cos^2\theta\sin\theta + \frac{\chi_{33}^{(2)}}{2}\sin^3\theta)E_e^2 \\ & + (\frac{\chi_{22}^{(2)}}{2}\sin 3\phi\cos\theta + \frac{\chi_{31}^{(2)}}{2}\sin\theta)\, E_o^2 \end{aligned} \tag{18}$$

Note that Eqs. (17) and (18) have three-fold symmetry with respect to the angle ϕ as required by the $LiNbO_3$ crystal symmetry. In order to isolate the far-infrared signal produced by the laser o-ray beating with e-ray from the laser rectifying signal, the angle ϕ was chosen to be 30° and a grid polarizer was used to filter out the far-infrared

e-ray generated by P_{De} in Eq. (18). In this case, the last two terms in Eq. (17) vanishes and P_{Do} contains signals of phase-matching at finite frequency only. The experimental result measured with the Michelson interferometer is shown in Fig. 6(b).

The backward phase-matched peak at 6.5 cm^{-1} was observed, but the forward phase-matched peak expected at 13.5 cm^{-1} was not distinguishable from the background noise. Again, the simple theoretical calculation using Eqs. (15) and (16) can predict location and linewidth of both backward and forward phase-matching frequencies and the general shape of the spectrum. Detailed theoretical curves calculated by Morris[23,24] for 1.8 and 2.3-psec Gaussian laser pulses are shown for comparison. It is seen that the relative strength of the 13.5 cm^{-1} peak is very sensitive to the variation of the pulsewidth, which changes with laser operating condition.

Measurements with the Fabry-Perot Interferometer

In a separate experiment, we used a Fabry-Perot interferometer with metal-mesh reflectors to analyze the spectrum. Since the spectrum is expected to contain only two narrow phase-matched peaks, a Fabry-Perot interferometer, which has higher peak transmissivity than the Michelson interferometer, should be more suitable. The construction of the Fabry-Perot interferometer is shown in Fig. 3. For conciseness and simplicity, the two micrometers used to adjust the parallelism of the two metal-mesh reflectors are not shown in the figure. A He:Ne laser was used to align the parallelism of the two metal-mesh reflectors by observing the diffraction spots from the metal meshes. The experimental results are shown in Fig. 7. The first, third and fifth

peaks in the figure arise from the forward phase-matched peak at 13.5 cm^{-1}, while the second and the fourth peaks have contributions from both the forward and the backward phase-matched peaks. Since the resolving power[20] of the Fabry-Perot interferometer was limited to about 4 due to the 40° spreading angle of the far-infrared radiation from the crystal, the theoretical width (~ 2 cm^{-1}) of the phase-matched peaks was not resolved. The solid curve in Fig. 7 is the detailed theoretical calculation of the interferometer fringes assuming Gaussian laser pulses of 1.8-psec pulse width. The details of this calculation are given in Appendix A. It appears to be in satisfactory agreement with the experimental results. As a separate check using the Fabry-Perot interferometer, we rotated the $LiNbO_3$ crystal to phase match at $\theta = 14°$. The result is shown in Fig. 8. The phase-matched peaks appear at 11 and 5.5 cm^{-1} as expected from the simple theory. As was the case for Fig. 7, the detailed theoretical fit assumes 1.8-psec Gaussian laser pulses. The details of the calculation are given in Appendix A.

The total far-infrared energy detected from $\chi_{33}^{(2)}$ in the first case (phase-matching at zero frequency) was of the order of 1 erg, which is about 20 times larger than that detected in the second case (phase-matching at finite frequency). Both agree to within an order of magnitude with a theoretical estimate based on a mode-locked laser train of 30 pulses and a peak power density of 0.2 GW/cm^2. We also measured the relative far-infrared power generated by $\chi_{31}^{(2)}$ and $\chi_{33}^{(2)}$. The measured ratio $\chi_{33}^{(2)}/\chi_{31}^{(2)} \simeq 4$ was in satisfactory agreement with the calculated value of 3.5.[32] The peak power of the picosecond far-infrared pulses in the first case was of the order of 200 W.

C. Conclusions and Discussions

We have observed far-infrared radiation generated in $LiNbO_3$ by picosecond light pulses from a mode-locked Nd:glass laser. The plane wave approximation with the Green's function method was adequate to explain the general shape of the spectra and the exact location of the peaks and valleys in the far-infrared power spectra for all of the experiments. Realistic numerical calculations which included various effects due to a finite beam cross section, crystal boundaries and the different optical and far-infrared phase velocities, were in agreement with the experimental results.

There is some discrepancy between the pulsewidths obtained from the two-photon absorption fluorescence measurements[27,28] and from the far-infrared generation measurements. This is due to the different nature of the two methods. The two photon absorption fluorescence techniques measure the autocorrelation of the actual pulse shape. If the pulse has some rapidly varying ripples on its more slowly varying envelope, and if the photographic technique[27,28] does not have sufficient resolution, then the two-photon absorption fluorescence technique tends to yield an autocorrelation function of only the more slowly varying part. The far-infrared generation measures the actual spectral content of the pulse and, consequently, would yield an apparently shorter pulse. Yajima, et al.[35] observed the far-infrared radiation as high as 20 cm^{-1} in the rectifying case and yet they obtained laser pulsewidth of 10 psec from the two-photon absorption fluorescence measurement. This result also indicated strongly the existence of the more rapidly varying ripples on its more slowly

varying pulse envelope. In the case of phase-matching at finite frequency, the forward phase-matching peak at 13.5 cm^{-1} is very sensitive to the pulse width around the two picosecond region. This method can be generally applied to monitor small pulsewidth changes under different experimental conditions. For shorter pulsewidths, the Gaussian envelope for the far-infrared radiation cuts off at a higher frequency and a crystal with bigger angle θ is needed to monitor this change. Similarly, for longer pulsewidths, the angle θ should be smaller.

The peak power of the picosecond far-infrared pulses produced in the rectifying case was of the order of 200 W, which could be increased to 5 kW by increasing the laser peak power density to 1 GW/cm^2. In the second case, the spectral width and the tunability of the generated radiation can not compete with the two CO_2 laser systems or the two dye laser systems described later in this thesis. But if the laser pulsewidth could be as short as 0.5 psec, this system could be capable of producing tunable far-infrared pulses from 3 to 40 cm^{-1}. Such pulses can be used to investigate transient and nonlinear phenomena in the far-infrared region.

Furthermore, under the same laser operating condition, it is obvious that crystals with larger electro-optical coefficients can generate more far-infrared power. The $LiIO_3$ crystal[36] was tried with less satisfactory results than $LiNbO_3$. Crystals with absorbing impurities which enhance the second-order nonlinearity may generate more powerful far-infrared radiation. This phenomenon has been

observed by Auston et al.[37,38] using the copper doped $LiTaO_3$ ($LiTaO_3$:Cu).

III. PHASE-MATCHED FAR-INFRARED GENERATION BY MIXING TWO DYE LASERS

A. Theory

Consider two plane wave laser beams with frequencies ω_1 and ω_2 propagating normal to a slab of the birefringent crystal with its optical $\hat{c}$-axis tilted an angle θ away from the normal. The nonlinear polarization responsible for the difference frequency generation can be written as

$$P_3^N = \chi_{eff} E_1 E_2^* \tag{20}$$

where χ_{eff} is the effective nonlinear coefficient and E_1, E_2 are laser fields propagating along $\hat{z}$-axis

$$E_j = \mathcal{E}_j \, e^{i(\omega_j t - k_j z) - \alpha_j z/2} \qquad j = 1,2 \tag{21}$$

and $k_j = \frac{\omega_j n_j}{c}$; n_j, α_j and $\mathcal{E}_j$ are the refractive index, the absorption constant, and the field amplitude, respectively.

If we assume no depletion of the input laser beams due to the difference frequency generation, then the Green's function method developed for section IIA can be used to calculate the far-infrared power. When the far-infrared absorption is included in (2), n_{3e} should be changed to $n_3 + i\alpha_3/2$. Using Eqs. (4), (5), (6), (7), (20), and (21), we solve the forward collinear case ($z > \ell$) and obtain

$$\mathcal{E}_3(z,\omega_3) = + \frac{\sqrt{2\pi}}{n_3 c} \, i\omega_3 \, e^{ik_3 z - \frac{\alpha_3}{2} z} \cdot$$

$$\int_0^\ell dz' \chi_{eff} \mathcal{E}_1 \mathcal{E}_2^* \, e^{i(k_1 - k_2 - k_3)z' - \frac{\alpha_1 + \alpha_2 - \alpha_3}{2} z'} \tag{22}$$

In the expression (22), the crystal slab is situated from 0 to ℓ along the z-axis. We assume that the detector is buried in the dielectric medium which has no far-infrared absorption but matches the refractive index of the mixing crystal. We then obtain the far-infrared output power per unit area as

$$P_3 = \frac{1}{n_3 c}\,\frac{1}{2}\,\omega_3^2\,|\chi_{eff}|^2|E_1|^2|E_2|^2\,\frac{e^{-\alpha_3\ell}+e^{-(\alpha_1+\alpha_2)\ell}-2\cos\Delta k\ell\, e^{-\frac{1}{2}(\alpha_1+\alpha_2+\alpha_3)\ell}}{(\Delta k)^2+(\frac{\alpha_3}{2}-\frac{\alpha_1+\alpha_2}{2})^2} \tag{23}$$

where

$$\Delta k = k_1-k_2-k_3 \tag{24}$$

Similarly, if we solve for the backward propagation far-infrared radiation (i.e., $z < 0$), we obtain the same formula (23) for the power except that

$$\Delta k = k_1-k_2+k_3 \tag{25}$$

The factor inside the bracket in formula(23) is the well-known phase-matching factor. Its importance can be seen from the following arguments. In the low absorption limit $\alpha_3 \simeq 0$ ($\alpha_1 = \alpha_2 = 0$), this phase matching factor is equal to

$$\frac{\sin^2(\frac{\Delta k}{2}\ell^2)}{(\frac{\Delta k}{2}\,\ell)^2}\cdot\ell\,,$$

which becomes ℓ^2 as k approaches zero. The far-infrared power is then proportional to the square of the crystal thickness. In the high absorption limit $\alpha_3\,\ell >> 1$ ($\alpha_1 = \alpha_2 = 0$), the phase-matching factor approaches $\frac{4}{\alpha_3^2}$ as Δk goes to zero. The far-infrared power is optimized when $\Delta k = 0$. This is called the phase-matching condition. In an

optically isotropic crystal, this condition cannot be satified for the collinear case. Being far away from the anomalous dispersion region, the far-infrared index of refraction is always larger than the optical index of refraction. Collinear phase-matching is possible by using a birefringent crystal. One of the two laser fields is in the ordinary ray, the other is in the extraordinary ray. The far-infrared radiation generated can be in the o-ray or in the e-ray. The e-ray index of refraction is a function of the crystal orientation. At a certain crystal orientation, k_1-k_2 can be arranged to be equal to k_3. This is the case of forward collinear phase-matching. For the same crystal orientation, the backward phase-matching condition can be satisfied for a different far-infrared frequency. For instance, $LiNbO_3$ is a negative birefringent crystal ($n_o > n_e$). In this experiment, the optical input wavelengths are around 8330 Å. At $\theta = 45°$, the forward collinear phase-matching (FCPM) frequency happens at $\omega_3 = 95\ cm^{-1}$ while the backward collinear phase-matching (BCPM) frequency is at 36 cm^{-1}. The generated far-infrared is in the o-ray.

To be commensurate with the real experimental situations, the plane-wave approximation should be modified.[39] In the following, each experimental condition and the corresponding modification of formula (23) will be discussed.

1. Double Refraction

In the collinear phase-matched scheme, since a birefringent crystal is used, one of the input fields is in the e-ray whose energy flow direction differs from that of the wavevector inside the crystal. The angle between those two directions is called "walk-off" angle.[40] Due

to this effect, the overlap of the two input beams walks off after a certain distance within the crystal. The maximum "walf-off" angle occurs near $\theta = 45°$.[41] In the case of $LiNbO_3$, this angle is 2.14°. In all the experiments, the crystal thickness is less than 2 mm. The "walk-off" distance of the two beams at the end of the crystal is less than 74μ which is negligible as the diameter of input beam cross section is around 3 mm. However, when the crystal thickness is larger than 1 cm, the effect becomes important.

2. Boundary Conditions

The refractive index of the mixing crystal differs from that of the vacuum. Boundary conditions should be imposed in solving for the electric fields inside and outside the crystal. The parallel surfaces of the crystal serve like a Fabry-Perot interferometer for both the input beams and the far-infrared. The $LiNbO_3$ has an optical index of refraction around 2.2 which results in a finesse of only 1.16. In addition, the input beams have around ~ 2 Å bandwidth which tends to wash out the Fabry-Perot fringes further. Therefore the effect of the crystal boundaries on the input beams is adequately described by the transmission coefficients,

$$|E_1|^2 = \frac{4\pi P_1 T_1}{n_1} \qquad \text{and} \qquad |E_2|^2 = \frac{4\pi P_2 T_2}{n_2} \tag{26}$$

where $P_{1,2}$ and $T_{1,2}$ are the power per unit area and the transmission coefficients for the frequencies ω_1 and ω_2 respectively. The boundary conditions affecting the far-infrared radiation are more complicated. The $LiNbO_3$ crystal has far-infrared refractive index of 6.6 for the

o-ray and 5.4 for the e-ray. Both rays have high absorption constants. An o-ray can convert part of its energy into the e-ray when it is reflected from the crystal boundary at $\theta \neq 0$. In order to see the Fabry-Perot pattern in the far-infrared, the transmission of a 0.5-mm thick $LiNbO_3$ crystal was measured by conventional Fourier Transfor Spectroscopy. The results showed that as $\omega_3 > 40\ cm^{-1}$, the Fabry-Perot transmission pattern flatened out for both o-ray and e-ray because of high absorption. Around 20 cm^{-1}, this pattern showed a large modulation. But our generated far-infrared has about a bandwidth of 3 cm^{-1}, which is wide enough to span a peak and valley of that modulation. In this case, the averaged values of the transmission and absorption coefficients are therefore valid. In the dye laser mixing experiment, the crystal thickness is greater than 0.5 mm. We include these effects in an effective transmission. Therefore a transmission coefficient representing the crystal boundary effects on the far-infrared radiation, T_3, is used to modify the expression for the power P_3 in formula (23). In summing up, we obtain

$$P_3 = \frac{8\pi^3}{c^3} \frac{T_1 T_2 T_3\ n_3}{n_1 n_2 \tilde{n}_3} \omega_3^2 |\chi_{eff}|^2 P_1 P_2^* \text{(phase-matching factor)} \tag{27}$$

3. Effects of Finite Beam Cross Section, Divergence, and Diffraction

In reality, the finite laser beam cross section and the associated divergence effect should be taken into consideration in the calculation instead of infinite plane waves. The laser beam in our experiment was focused and had 2 miliradian divergence. The mixing crystal was situated at about 26 Raleigh range (estimated from a TEM_{∞} laser beam) away from the minimum beam width (detailed information is given in Section IIB). Therefore the ray-optics approximation is valid for the input beams. The divergence of the multi-mode input beams will cause the far-infrared radiation to spread through an angle γ as shown in Fig. 9(a), where δ is the divergence angle. Under the forward collinear phase-matching condition, Δk is not zero because of this divergence and of the multi-mode laser beams,

$$\Delta k = \sqrt{k_3^{\,2} + (k_1\delta)^2} - k_3 \simeq \frac{(k_1\delta)^2}{2k_3} \tag{28}$$

and $\gamma = \dfrac{k_1\delta}{k_3}$

To demonstrate the significance of this effect, if ω_3 generated is at 20 cm^{-1}, we have $\Delta k = 13.5\ cm^{-1}$ and $\gamma = 11°$. The far-infrared total reflection angle inside the $LiNbO_3$ at $\omega_3 = 20\ cm^{-1}$ is 8.7°. We can see that part of the far-infrared generated is totally reflected back to the $LiNbO_3$ crystal and never reaches the detector. The experimental far-infrared power should be less at low frequencies than that calculated from the plane wave approximation. In addition, the radius

R of the beam was 1.5 mm at the crystal. The total far-infrared power should be

$$P_{3(total)} = \frac{P_3}{\pi R^2}, \quad \frac{1}{R^2} = \frac{2}{R_1^{\,2}+R_2^{\,2}} \tag{30}$$

where P_3 is expressed as in formula (27), and R_1 and R_2 are the Gaussian beam radius at e^{-2} intensity for ω_1 and ω_2, respectively. The expression for R in formula (30) guarentees that the actual area of the beam overlap is less than the minimum of the two input beams. For the far-infrared field, the wavelength λ_3 is long, and the diffraction angle γ_D satisfies roughly the following equation inside the crystal

$$\sin\gamma_D = \frac{1.22\ \lambda_3}{2\ n_3\ R}$$

At $\omega_3 = 20\ cm^{-1}$, γ_D equals to 1.75° which is much less than γ. The spreading angle outside the crystal due to γ_D is 11.73° which is not important compared to the 45° collecting angle of the detection system. However, the far-infrared diffraction effect will shorten the crystal coherence length from the value derived from the plane-wave approximation. This effect is even more complicated when multi-mode laser beams are included. This point can not be clarified without going to a more detailed theoretical treatment.

4. Finite Far-Infrared Linewidth

The bandwidth of the input laser beams results in a far-infrared bandwidth of 3 cm^{-1} in the mixing experiment. This finite bandwidth causes the phase-mismatch Δk to deviate from zero even when the central far-infrared frequency is phase-matched. For the FCPM case, from Eq. (24), we obtain

$$d(\Delta k) = (n_o - n_3)\ \frac{\Delta w_3}{c} + \frac{\Delta w_3}{c}\ (n_o - n_e(\theta))$$

$$\simeq (n_o - n_3)\ \frac{\Delta w_3}{c} = -82.9\ \mathrm{cm}^{-1} \tag{32}$$

and for the BCPM case, using Eq. (25), we get

$$d(\Delta k) = (n_o + n_3)\ \frac{\Delta w_3}{c} - \frac{\Delta w_2}{c}\ (n_o - n_e(\theta))$$

$$\simeq (n_o + n_3)\ \frac{\Delta w_3}{c} = 165.8\ \mathrm{cm}^{-1} \tag{33}$$

where Δw_3 is the far-infrared bandwidth and the numberical values are calculated for the $LiNbO_3$ crystal. In calculating the far-infrared power from Eqs. (27) and (28), we should integrate over the far-infrared bandwidth. However, aside from the phase-matching factor, the expression is not a sensitive function of w_3 within this bandwidth, as w_3 is reasonably far away from the polariton mode frequency. We carry out the integration which only includes the phase-matching factor. It can be seen from Eqs. (32) and (33) that the integration averaged over Δk is different in the FCPM case from the BCPM case, even though the far-infrared bandwidth is the same.

5. The Dispersions of the Dielectric Constant and the Second Order Nonlinear Susceptibility

There are eight E polariton modes[26] (with the lowest frequency are one at 152 cm^{-1}) which determine the dispersion of the dielectric constant of the far-infrared o-ray in $LiNbO_3$. The refractive index n_3, the absorption constant α_3, and the transmission coefficient T_3

can be calculated from the dielectric constant expressed as

$$\varepsilon(w_3) = \varepsilon_o + \sum_j \frac{S_j\, w_{T_j}}{(w_{T_j}^2 - w_3^2) + i\Gamma_j w_3} \tag{34}$$

where ε_o is the DC dielectric constant and w_{T_j}, S_j, and Γ_j are the jth polariton mode frequency, the oscillator strength, and the related damping constant, respectively. The derivation[42-44] of the dispersion of the second order nonlinear susceptibility is described in Appendix B. It can be summarized in the following by the assumption that the linear susceptibility of the mixing crystal does not have appreciable dispersion in the region of the input laser frequecies w_1 and w_2

$$\frac{1}{2}\chi^{(2)}(w_3) = d(w_3) = d_E + \frac{1}{4\pi}\sum_j \frac{S_j w_{T_j}^2\, d_{\theta j}}{w_{T_j}^2 - w_3^2 + i\Gamma_j w_3} \tag{35}$$

$$d_{\theta j} \pm \left[\frac{8\pi c^4 n_p (S_{ex,j}/Ld\Omega)}{S_j \hbar w_{T_j} w_s^4 n_s (\bar{n}_{T_j} + 1)}\right]^{1/2} \tag{36}$$

$$d(0) = d_E + \frac{1}{4\pi}\sum_j S_j d_{\theta j} = r n_p^4 \quad {}^{*,44} \tag{37}$$

In using the formula we first calculate $d_{\theta j}$ from Eq. (36) and d_E from Eq. (37), then use d_E and $d_{\theta j}$ in Eq. (35) to find out the dispersion of $\chi^{(2)}(w_3)$. The $d_{\theta j}$ in Eq. (36) is directly related to the Raman

*This formula should be modified if tensor notation is used for $\chi^{(2)}$, please see reference 44.

scattering experiment on the w_{T_j}-frequency polariton mode where n_p and n_s are the refractive indices of the Raman pumping beam and the scattered beam, respectively; w_s is the frequency of the scattered beam. The $S_{ex,j}/Ld\Omega$ denotes the Raman scattering extinction length per unit solid angle on the jth polariton mode and $\bar{n}_{T_j}$ represents the average thermal population number of polariton quanta at the sample temperature T. The $\bar{n}_{T_j}$ [44] can be expressed as

$$\bar{n}_{T_j} = \frac{1}{e^{\hbar w_{T_j}/kT}-1} \tag{38}$$

In Eq. (37), r is the measured electro-optical constant when the measuring light frequency is the same as that of the Raman scattering input beam.

In summing up, combining Eqs. (23), (27) and (30), we get the far-infrared power (in watts)

$$P_{3(total)} = \frac{8\pi^2}{c^3} \frac{T_1T_2T_3n_3}{n_1n_2\tilde{n}_3} w_3^2 |\chi_{eff}|^2 P_1P_2 \frac{2}{R_1^2+R_2^2} \bar{I} \tag{39}$$

where

$$I = \frac{e^{-\alpha_3\ell} + e^{-(\alpha_1+\alpha_2)\ell} - 2\cos\Delta k\ell\, e^{-\frac{1}{2}(\alpha_1+\alpha_2+\alpha_3)\ell}}{(\Delta k)^2 + (\frac{\alpha_3}{2} - \frac{\alpha_1+\alpha_2}{2})^2}$$

and $\bar{I}$ is the average of I over the different values of Δk caused by the laser beam divergence, the diffraction and finite bandwidth of the far-infrared radiation.

It is worth mentioning the physical meaning expressed by Eqs. (35), (36), and (37) about the contribution of the polariton modes to the

second order nonlinear susceptibility. We can think the difference frequency generation as an induced parametric process, or as an induced three photon process. A photon of w_1 is converted into two lower frequency photons of w_2 and w_3. The laser beam at frequency w_2 is used to enhance, or induce the conversion. The physical picture of this conversion can be illustrated when the far-infrared frequency w_3 is the same as one of the polariton modes of the mixing crystal. In this case, a photon at frequency w_1 is scattered to become a photon at lower frequency w_2 (like Raman scattering) and excites a polariton mode, which radiates far-infrared. The nonlinear coefficient responsible for the difference frequency generation is proportional to the product of the Raman scattering cross-section and the radiation efficiency of that polariton mode. The term included in the summation in Eq. (35) has this physical meaning. Note that $d_{\theta j}$ in Eq. (36) can be negative or positive. The contribution of the polariton modes to the second order nonlinear susceptibility can be constructive or destructive. Note also that the oscillator strength, S_j, of the polariton mode plays a complicated role in its relation to the far-infrared generation from the mixing experiment. It is contained both in the nonlinear susceptibility and the far-infrared absorption constant.

Noncollinear phase-matching is possible in any crystal which possesses anomalous dispersion between the incident laser radiation and the far-infrared difference frequency radiation. Optically isotropic crystals as well as crystals with birefringence can be used to achieve noncollinear phase-matching. All three waves involved are usually polarized in the same direction. The index of refraction of the far-

infrared radiation is usually quite large so that a corner of the mixing crystal is chopped off in order to facilitate the far-infrared collection (see Fig. 12). The two input beams cross with an angle and the far-infrared radiation comes out in a different direction making the exact detailed theoretical description even more difficult than the collinear phase-matched case. A heuristic theory which contains the major physical effects and is adequate to explain roughly the experimental results can be obtained from a modification of the collinear phase-matched case.

We assume that Eq. (39) is true for the nonlinear phase-matched case except that ℓ is replaced by ℓ_{eff} which represents the effective crystal length through which the three waves involved really interact. A simple analysis will show that Eq. (39) is only valid at the phase-matching angle for the noncollinear case. The other physical conditions--the double refraction, the boundary conditions, the dispersion of the dielectric constant and the second-order nonlinear susceptibility can be argued as in the collinear phase-matched case. But the effects of finite far-infrared linewidth and the divergence of input laser beams on Δk in Eq. (39) take different forms. Under nonlinear phase-matching conditions, the divergence of the input laser beams causes a nonvanishing Δk in Eq. (39). From Fig. 9(b), we obtain

$$\Delta k \cong k_1 \delta \sin\phi \tag{40}$$

where δ is divergence angle and ϕ is the angle between $\hat{k}_1$ and $\hat{k}_3$. Equation (40) indicates the importance of the laser divergence under phase-matching conditions. In the dye laser experiment using $LiNbO_3$,

we obtain $\Delta k = 137\ cm^{-1}$ which is much larger than that due to finite far-infrared linewidth whose contribution to Δk in Eq. (39) can be expressed as

$$\Delta k \cong [n_3 - n_1 \cos(\phi - \psi)] \frac{\Delta\omega_3}{c} \tag{41}$$

For the derivation of Eq. (41), see Fig. 9(b).

B. Experimental Techniques

1. Dual-Frequency One Dye Cell Scheme

Figure 10 shows the detailed experimental arrangement using a dual-frequency dye laser. A Glan Thomson polarizer[45] (GTP) with anti-reflection coatings was used inside the laser cavity to divide the beam into two orthogonally polarized components. Two 312 mm echelle gratings operated in the Littrow configuration in the 7th order were used for feedback and independent frequency tuning of the two polarization components. The gratings were aligned correctly to the output mirror using a He:Ne laser. The use of a single dye cell and an output mirror ensured that the two output laser beams were well overlapped spatially. Fine tuning for spatial overlap was achieved by observing the burn spots of each laser in the focal plane of a lens. Temporal overlap of the beams requires equalizing the net gain in the two arms of the cavity. A ruby laser beam circularly polarized or linearly polarized in a direction at 45° from the GTP axis was used to pump the dye cell (DTTC iodide in DMSO[46] as in Bradleys[47] single frequency dye laser). The dye cell was a 1 cm^2 Bechman spectrophotometer cell. The dye concentration was not critical; however, it was adjusted to give

20% transmission for low level light at 6900 Å. Temporal overlap could be optimized by modifying the relative gain of the two arms with a microscope slide inside the cavity. We estimated the grating reflectivity to be 40% based on the reflectivity in the 8th order autocollimation for a He:Ne laser. The output mirror had 70% reflectivity at dye laser frequencies. With a 30-mW, 30-ηs ruby pumping beam the dye laser output had a peak power of 600 kW and its two wavelengths could be tuned independently from 8100 Å to 8400 Å as verified by an 1-1/2 meter Jarrel-Ash spectrometer. The linear polarization of the output beam was pure to within 10% and the two polarizations of the beams were not mutually orthogonal. A lens with 75 cm focal length was used to examine the focal spot size of the laser beams and yielded a spot radius of about 1.5 mm. This implied that the laser output had a half angle divergence of 2 milliradian. The nearly elongated spatial profile foreach beam indicated that the laser transverse mode was not a single mode but multi-mode. The lens with 75 cm focal length was used to focus the beam on the crystal which was placed 70 cm from the lens.

In order to reduce statistical noise due to laser fluctuations, the far-infrared signal was normalized against the sum-frequency signal generated by reflection from a (110) surface of an InAs crystal, which has a negligible dispersion in our frequency range. Discrimination against the second-harmonic signal[48] was achieved by orienting one laser field parallel to [001] crystal axis which was perpendicular to the plane of incidence. The other laser field was arranged parallel to the plane of incidence and had no component along [001]. Since the

InAs crystal has a cubic symmetry ($\bar{4}3m$), the polarization of the sum frequency signal generated in this configuration by $\chi_{14}^{(2)}$ and $\chi_{25}^{(2)}$ was perpendicular to [001]. The second-harmonic signal generated by $\chi_{36}^{(2)}$ was polarized parallel to [001] and was rejected by a polarizer. Seven cm of a saturated solution of $CuSO_4$ was used to filter out the laser light. The sum frequency signal was detected by an S-5 photomultiplier. The intracavity microscope slide (Fig. 8) used to adjust the relative gain of the two arms of the cavity was used to couple out a fraction of the orthogonally polarized beams for sum-frequency generation.

The dual-frequency one dye-cell scheme was very easy to operate for the forward and backward collinear far-infrared generation. It can be used for the noncollinear phase-matched experiment by placing another Glan Thomson polarizer right after the laser output mirror to separate two beams spatially. After the polarization of the w_1 beam is rotated 90°, the two beams can be combined by a prism (see Fig. 12).

2. Two-dye-cell Scheme

The far-infrared generation can of course be achieved by using two separate dye lasers. In fact, two-dye-cell scheme was used before the idea of the one-dye-cell scheme was well developed. Figures 11 and 12 show experimental schemes which use two dye cells. The former was for the backward and forward collinear phase-matched experiment, the latter for the noncollinear phase-matched experiment. In Fig. 11, the ruby beam experimental set-up which was omitted in both Figs. 10 and 12 was drawn for the purpose of completeness. It consisted of a

Q-switched ruby oscillator laser rod and the amplifier laser rod which were both 4-inches long and their diameters were 5/16 inch and 3/8 inch, respectively. Two sets of two linear lamps housed in a double ellipse reflector were used to excite the oscillator and the amplifier ruby rods respectively. The oscillator lamps discharged about 555 Joules and the amplifier lamp 750 Joules. The discharge of the amplifier lamps should precede that of the oscillator in order to have high gain. In our experiment, the lamps of the oscillator and the amplifier were fired at the same time so that the ruby laser power was only doubled by the amplifier. The total ruby laser power was about 30 MW. Half of the vertically polarized ruby beam was used to pump a dye laser (as C2 in Fig. 11) whose polarization was also vertical. The ruling grooves on the grating reflect more light with its polarization parallel to them rather than perpendicular. Hence the ruling grooves on the grating were always arranged to be parallel to the polarization of the pump beam. The other half of the ruby beam with its polarization rotated 90° by a pair of Fresnel rhombs was used to pump another dye laser. The dye lasers with orthogonal polarizations were then combined by a Glan Thomson polarizer. Again a lense with 75 cm focal length was used to focus the beams on the crystal which was 70 cm from the lense. About 8% of the focused beam was deflected by a microscopic slide to generate sum-frequency signal on the InAs surface for normalization.

Figure 12 shows a two-dye-cell scheme used for the noncollinear phase-matching experiments. The ruby beam was split to pump the two dye cells. The polarizations of the two output dye lasers were

parallel. The microscope slides were used to couple out part of the energy from each beam. Two prisms were used to deflect the coupled-out W_1 beam whose polarization was rotated 90° by a pair of Fresnel rhombs. The coupled-out beams were combined by a Glan Thomson polarizer and focused to generate the sum-frequency signal for normalization. Two lenses with 80 cm focal length were used to independently focus the beam. The mixing crystals were 75 cm from each lens. A third prism was used to deflect the focused W_2 beam which beat with the focused W_1 beam in the crystal to generate far-infrared radiation. Non-collinear phase-matching was achieved by the coupled rotation and transition of the prism. Only one piece of $LiNbO_3$ (a 4 mm cube with a corner cut off) was used for the noncollinear phase-matching experiment.

3. Far-infrared Detection

Far-infrared signals in the 20 to 95 cm^{-1} range were detected with an n-type InSb detector[29] (see Fig. 4) operated at 1.4°K in a 14.5 kG magnetic field which causes a cyclotron resonance peak[49] around 95 cm^{-1}. In the 95 cm^{-1} to 200 cm^{-1} range, a Ge:Ga[50] photoconductive detector [see Fig. 5(a)] at 4.2°K was used. The detector bias and the current-measuring operational amplifier is shown in Fig. 5(b). Black polyethylene sheets with total thickness of 0.75 mm were used to prevent laser beams from reaching the far-infrared detectors. For the forward collinear and noncollinear phase-matching experiments, a 1-cm diameter evacuated brass light pipe with a black polyethylene window which was 0.5 cm away from the mixing crystal was used to guide the far-infrared radiation for detection. The L-shaped brass light pipe had a brass

reflector at the elbow-bend. To observe the backward collinearly phase-matched signal, we added a right angle bend to the light pipe. The dye laser beams passed through a 1/8-in. hole in the right angle bend and hit the crystal mounted near the mouth of the light pipe. The far-infrared radiation was then collected from the back (laser beam entrance side) of the crystal. There was about 5 cm of air in the collection path. The electric signal from the amplifier and the signal from the photomultiplier (representing the sum-frequency signal) were displayed on a dual beam oscilloscope where we took the picture of the two signals simultaneously. The ratio of the two signals was then computed.

The instrumental function (the sensitivity of the filter-detector system) was measured by conventional Fourier transform spectroscopy[15,19] using, as a reference, a Golay cell[51] with a diamond window having a flat response. The far-infrared power detected from the mixing experiment versus frequency was then divided point by point by the instrumental function to obtain the true relative power spectrum. In the measurement of the instrumental function, the mercury arc source, the interferometer, and light pipe system were the same as for the Golay cell and the far-infrared detectors. The only difference was the value of $A\Omega$, (where A is the detector area and Ω is the detecting solid angle) which was 0.026 for the Golay cell and 0.079 for the Fe:Fa detector. We assumed the difference $A\Omega$ value did not affect the frequency response.

The absolute far-infrared power at 125 cm^{-1} from the forward collinear phase-matching experiment was measured to be 4.85 mW using the

Ge:Ga detector. The discussion of the calibration of this detector is as follows. The responsivity[50] curve of the Ge:Ga versus frequency starts at around 80 cm^{-1}, has a peak at 95 cm^{-1}, then decreases steadily to a negligible value at about 200 cm^{-1}. This curve could be simplified by assuming that the detector's true responsivity at 125 cm^{-1} was constant over the frequency range from 85 cm^{-1} to 190 cm^{-1}. The Michelson interferometer (with 1/2 mil mylar beam splitter combined with Yoshinaga filter), which had output radiation from 50 to 200 cm^{-1}, was used as the source for the Ge:Ga detector and the Golay cell. At the zero path of the Michelson interferometer, the Ge:Ga detector had 0.96 mV output, while the Golay cell had 0.2 V output. The Golay cell has a flat response and the responsivity is known from the manual to be 8.3×10^5 V/watt.[51] From this result and the fact that the Ge:Ga detector had three times larger $A\Omega$ value but detected one-third less radiation because of sensitivity cut-off, we calculated that the responsivity of the Ge:Ga detector including the 0.75 cm black polyethylene filter was 2×10^3 V/watt. The electrical noise of the Ge:Ga detector which was biased at 1.35 V (the same as used in the laser mixing experiment) was measured to be 1.2×10^{-7} $V/\sqrt{Hz}$ by a lock-in amplifier at a chopping frequency of 280 Hz. The PAR type D preamplifier used in the lock-in amplifier did not contribute to the dominant noise at this chopping frequency and the Ge:Ga resistance of 240 $k\Omega$. The noise figure of the preamplifier under this condition was less than 0.1 dB.

From these results we concluded that the electrical noise equivalent power of the Ge:Ga detector was 6×10^{-11} W/$\sqrt{\text{Hz}}$. If we assumed that the Ge:Ga detector absorbs 50% of the incident radiation and reflects about 50% with its two surfaces (n=4), then its noise equivalent power including the 500 kHz detection bandwidth would be 8.48×10^{-8} watts. In the mixing experiment, the 2 μs response time of the detection system tended to average out the 30 ns far-infrared pulse. The minimum detectable far-infrared peak power generated should be equal to 8.48×10^{-8} watts×2 μs/30 ns = 5.86 μwatts. This value had to be corrected due to the 0.75 cm black polyethylene filter[52] which attenuated the 125 cm^{-1} radiation a factor of 8.65 and the light pipe attenuated a factor of 3 by observation. The real minimum detectable far-infrared peak power generated at 125 cm^{-1} by the mixing experiments was 0.147 mW. We observed that the far-infrared signal to noise ratio generated in $LiNbO_3$ at 125 cm^{-1} was 33.

The above absolute power calibration at 125 cm^{-1} would be invalid if in the laser mixing experiment, the operational amplifier shown in Fig. 5(b) induced more noise than the Ge:Ga detector. We biased the detector at 1.35 V for the best measured signal to noise ratio. The peak-to-peak noise voltage V_{pp} at the amplifier output was 2 mV. We replaced the detector by an equivalent room temperature resistor and observed V_{pp} = 0.3 mV. Hence, we concluded that the detector-system (Ge:Ga) was detector-noise limited.

However, in using the InSb (Putley) detector we observed V_{pp} = 0.3 mV, the same for both the detector and the equivalent room

temperature resistor. Hence, for the system the noise was limited by the amplifier. As a check, the 95 cm^{-1} signal generated by the non-collinear phase-matching experiment was detected by two detector systems. The InSb detector system yielded a signal to noise ratio three times higher than that of the Ge:Ga detector system whose responsivity at 95 cm^{-1} was about twice higher than at 125 cm^{-1}. This implies that the Ge:Ga detector is very noisy. This excess noise might also come from the electric contacts which were made by using indium solder.

4. Crystal Preparation

Table I describes the $LiNbO_3$ crystals used for the experiment. Table II shows the other crystals used in the experiment. In order to measure the resistivity (Ω/cm) of the semiconductor samples, we used GaIn alloy to wet the crystal edges for making the electrical contacts. The ZnS crystal was a long strip 1 mm wide which would not accept all the input beams. This factor was included in the correction of the far-infrared power measurement shown in Table III. Two CdSe crystals with different resistivities were used for the experiment. No signal greater than noise was observed in either case. Note that the resistivity of the semiconductors is important in the mixing experiments because it is related to the free electron plasma oscillation which limits the lowest far-infrared frequency which can be generated. It is also related to the far-infrared refractive index which affects the phase-matching.

5. Phase-Matching Methods

Since $LiNbO_3$ is a negative birefringent crystal ($n_o > n_e$, where $n_{o,e}$ are the indices of refraction of the ordinary and extraordinary rays respectively), the forward collinear phase-matching achieved by arranging the W_1 beam along the o-ray and the W_2 beam along the e-ray ($W_1 > W_2$, $|k_1| > |k_2|$) generated the far-infrared o-ray. Backward collinear phase-matching obtained by positioning the W_1 beam in the e-ray and the W_2 beam in the o-ray ($W_1 > W_2$ but $|k_1| < |k_2|$) also generated a far-infrared o-ray. The other four mixing crystals shown in Table II are positive birefringent crystals ($n_o < n_e$). The W_1 beam in e-ray and the W_2 beam in o-ray was used for the forward collinear phase-matching which generated the far-infrared o-ray. In all the collinear phase-matching experiments using the five crystals, the effective second order nonlinear susceptibility $\chi^{(2)}_{eff}$ was equal to $\chi^{(2)}_{24}\sin\theta$, where θ is the phase-matching angle. In doing the noncollinear phase-matching experiment in $LiNbO_3$, $\chi^{(2)}_{eff} = \chi^{(2)}_{33}$ was used which generated the far-infrared e-ray. The two dye laser beams were required to cross at an angle ψ as shown in Fig. 12. The e-ray far-infrared came out another direction as shown in Fig. 12.

C. Results of Experiments and Comparison with Theory

For quick reference, a summary of experimental results is presented in Table III which shows the frequency tuning range and the power of the far-infrared radiation generated in five different crystals. Typical far-infrared wavelength measurement by a Fabry-Perot interferometer with metal mesh reflectors is shown in Fig. 13. This

measurement was the earliest taken of the experiments with the experimental scheme shown in Fig. 11. But the two gratings were not the same, one echelle grating with 312/mm rulings operated on the 7th order, and the other with 1200/mm rulings operated on the first order. The far-infrared line width produced in this case was different from that with two 312/mm gratings which were used for the rest of the experiment. Hence, no theoretical calculation for the Fabry-Perot fringes was attempted because we did not know the linewidth. The purpose of this experiment was to calibrate the difference in wavelength of input laser beams measured by a Jarrell-Ash 1.5 m spectrometer. A photographic plate[24] was taken inside the spectrometer to register the two laser wavelengths, one fixed and the other changed with the tuning of the laser grating. Hence, the difference frequency W_3 versus the grating tuning was established. The value of W_3 calibrated in this way had the estimated error of less than $\pm$ 2 cm^{-1}.

The $LiNbO_3$ crystals used in the collinear phase-matched experiments (see Table I) were cut with $\phi = 0°$ (ϕ is the angle between the a-axis and the plane containing the c-axis and k-wavevector). In this configuration, the nonlinear polarizations for far-infrared o-ray and for far-infrared e-ray have the following forms from Eqs. (17) and (18), respectively

$$P_{30} = \chi_{24}\sin\theta E_1 E_2^* \tag{41}$$

$$P_{3e} = \chi_{22}\cos^2\theta E_1 E_2^* + \text{Rectifying term} \tag{42}$$

The rectifying term represents the contributions from $E_1E_1^*$ and $E_2E_2^*$ which are centered at zero frequency. In the experiment, only the

phase-matched o-ray generation was explored. The polarization of far-infrared output was checked by a grid polarizer. Note that because the far-infrared o-ray index of refraction is different from that of e-ray, the phase-matching condition can be satisfied for one of them but not for both simultaneously. The equations indicate that the phase-matched o-ray power is greater than the phase-matched e-ray power ($\chi_{24}^{(2)} \simeq 7\ \chi_{22}^{(2)}$) with the exception of the small θ case. Also the e-ray is difficult to distinguish from the laser rectifying signals.

The theoretical calculations for the phase-matching angle versus the phase-matching frequency is shown in Fig. 14 for $LiNbO_3$[33,34] (both FCPM and BCPM), ZnO,[53,54] ZnS,[55,56] and CdS[53,57] (FCPM only). Experimentally, under the condition that no precise angle determination was attempted for $LiNbO_3$ and the uncertainty in the measurement of W_3, we observed that the results were quite well described by this theoretical calculation from 20 to 127 cm^{-1}. In ZnO, the observed phase-matching frequency of 190 cm^{-1} at $\theta = 90°$ agreed well with the theoretical calculation. However, in CdS the observed phase-matching frequency of 180 cm^{-1} at $\theta = 90°$ was lower than that of the predicted value. This discrepancy might be due to the fact that our CdS crystal has a low resistivity of 1.5 Ω/cm so that the far-infrared index of refraction was changed due to the free electron plasma oscillation in the crystal. Note that the ZnO crystal has high resistivity of $2 \times 10^4\ \Omega$/cm. The observed phase-matching frequency of 91 cm^{-1} at $\theta = 90°$ for ZnS was also lower than the predicted value of 120 cm^{-1}. However, in calculation of ZnS, the dispersion of the far-infrared

refraction index was not included ($\varepsilon_o = 8.6$)[56] due to nonavailability of the experimental results.[58]

Figure 15 shows two phase-matching curves. The inner curve was obtained in a 1.6-mm thick $LiNbO_3$ with $\theta = 16°$. The forward phase-matching frequency was at 21 cm^{-1}. Another piece of 0.5 mm thick $LiNbO_3$ crystal was cut from the same boule at $\theta = 90°$ for the far-infrared transmission measurement by a Michelson interferometer. From the Fabry-Perot transmission pattern of this crystal and the known far-infrared o-ray index of refraction ($n = 6.6$), we deduced that the o-ray far-infrared absorption constant α_3 was 14 cm^{-1} at $\omega_3 = 21$ cm^{-1}. The outer curve in Fig. 15 shows the backward phase-matching curve at 56 cm^{-1} in $LiNbO_3$. Another two forward phase-matching curves in $LiNbO_3$ are shown in Fig. 16. Both Figs. 15 and 16 were obtained by fixing the wavelengths of the input beams and rotating the mixing crystal. The abscissa denoted the angle of rotation inside the crystal. From Eq. (39), we obtained the following formula for the far-infrared power (in watts)

$$P_3(\theta) = \int \frac{A\sin^2\theta}{|\Delta k(\theta)|^2+(\alpha_3/2)^2} \left[1 + e^{-\alpha_3\ell} - 2\cos(\Delta k(\theta)\ell)e^{-\alpha_3/2\cdot\ell}\right] d(\Delta\omega_3) \tag{43}$$

where A is a constant and the integration is over the far-infrared line-width. The $\Delta k(\theta)$ in Eq. (43) can be expressed as

$$\Delta k(\theta) \cong (n_o - n_3)\frac{\Delta w_3}{c} - \frac{w_2}{c}\left.\frac{dn_e(\theta)}{d\theta}\right|_{\theta=\theta_0}\Delta\theta \tag{44}$$

The equations (43) and (44) indicate that in an ideal case either the far-infrared linewidth or the absorption constant α_3 can be deduced from the phase-matching curves if the other value is given. Computer calculations[24] fitting the forward collinear phase-matching curve obtained by a 1.6-mm thick $LiNbO_3$ crystal at $\theta = 16°$ (phase-matched at 21 cm^{-1}) and $\alpha_3 = 14\ cm^{-1}$ (measured) yielded the far-infrared linewidth of 3 cm^{-1}. Both the experimental result and the theoretical calculation is shown in Fig. 15. When $\alpha_3 \ell >> 1$ and $\alpha_3 >> (n_3 \pm n_0)\Delta w_3/c$ (+ for BCPM, - for FCPM), $P_3(\theta)$ in Eq. (43) reduces to

$$P_3(\theta) \cong \frac{A \sin^2\theta}{(\frac{w_2}{c}(n_e(\theta)-n_0)+B)^2 + (\alpha_3/2)^2} (\Delta w_3) \tag{45}$$

where B is a constant related to the center of the phase-matching curve. This situation represents the experimental results shown by the outer curve of Fig. 15 and the curves of Fig. 16. In order to obtain the absorption constant α_3 and its standard deviation from the phase-matching curve, the quantity

$$Q^2_{A,B,\alpha_3} = \sum_j [P_j^{\ 2} - P_3^{\ 2}(\theta_j)_{A,B,\alpha_3}]/(m-3) \tag{46}$$

was minimized[24] with respect to the parameters A, B, and α_3, where P_j was the experimentally observed far-infrared power and $P_3(\theta_j)_{A,B,\alpha_3}$ was the calculated value at $\theta=\theta_j$ respectively and m was the number summed over j. The Q_{A,B,α_3} represented the power standard deviation which was inverted to give the standard deviation[24,59] of the absorption coefficient. Figure 17 summarizes the absorption constants and

their standard devistions from the forward collinear phase-matching experiments in $LiNbO_3$. The solid curve in that figure shows the experimental results obtained by the far-infrared transmission measurement of Bosomworth[33] for $w_3 \leqslant 70\ cm^{-1}$ and the infrared reflection measurement of Barker and Landon[26] for $w_3 > 70\ cm^{-1}$. The deviation of the absorption constant from the different samples with different ways of measurements has been reported by Ushioda et al.[60] in the crystals of GaP, ZnO and $LiNbO_3$ (A1 mode). We belive the deviation as shown in Fig. 17 is real in our sample. The sharp rising around $w_3 = 65\ cm^{-1}$ might be directly associated with two phonon density of states.[60] Note that, from Eq. (43), when $|\Delta k(\theta)|$ evaluated at the phase-matching angle does not vanish and is greater than $\frac{\alpha_3}{2}$ due to the laser beam divergence and/or the finite bandwidth of w_3, the phase-matching curve is no longer a sensitive way to measure the far-infrared absorption constant. We were not able to deduce the absorption constant α_3 for the e-ray from the mixing experiment. The FIR e-ray signal generated with FCPM via $\chi_{22}^{(2)}$ was too weak [see Eq. (42)] and the values of α_3 deduced from the NCPM results were rather inaccurate because of the 4-m rad laser divergence (see Section IIA).

The far-infrared power as a function of w_3 generated in $LiNbO_3$ for the collinear phase-matched (both forward and backward) and the noncollinear phase-matched schemes after the correction of instrumental functions is shown in Fig. 18. The solid curves represent the corresponding theoretical calculations using the Eq. (39) whose validity was discussed in detail in Section IIIA. In using Eq. (39), we

carried out the average only over the phase-matching factor I ($\alpha_1 = \alpha_2 \simeq 0$), since the rest of the equation varies slowly as a function of w_3 within the bandwidth of 3 cm^{-1}. Note that the main contribution to Δk in I is due to the finite far-infrared bandwidth for FCPM and BCPM and due to the divergence of the input laser beams for NCPM (see Section IIIA). For the calculation of the dispersions of $\chi_{24}^{(2)}$ ($\chi_{24}^{(2)}(0) = 3.2 \times 10^{-6}$ e.s.u. for CPM) and $\chi_{33}^{(2)}$ ($\chi_{33}^{(2)}(0) = 3.3 \times 10^{-6}$ e.s.u. for NCPM), we used Eqs. (35), (36) and (37) and the oscillator strengths of Barker and Loudon[26] and the Raman cross section of Kaminow and Johnston, Jr.[61] In calculating the dispersions of n_3(o-ray for CPM and e-ray for NCPM) we used the data of Bosomworth[33] and Barker and Loudon.[26] For the o-ray, we used the observed values of α_3 shown in Fig. 17. Those dispersions were included in the calculation for the far-infrared power.

The theoretical calculation for the FCPM case (see Fig. 18) describes the experimental result quite well except on the low frequency side. Now let us take the divergence of the laser beam into consideration. From Section IIIA (3) or Fig. 9(a), the far-infrared radiation spreads a half angle of 11° at $w_3 = 20$ cm^{-1} inside the crystal due to the laser beam divergence effect. If the detector has a collection half angle of 45°, this means that only the radiation within a cone with a half angle of 6.7° inside the crystal goes to the detector. The generated far-infrared power at $w_3 = 20$ cm^{-1} should be 3 times higher than detected. For the same reason, the generated far-infrared power at $w_3 = 30$ cm^{-1} should be 1.4 times higher

than monitored. For $w_3 \geqslant 40$ cm^{-1}, the far-infrared spreading angle is less than the collection angle so that all the radiation is collected. The collection angle of 45° is reasonable for the InSb detector (see Fig. 4) since no focusing cone was used in front of the detector. From the above arguments, we conclude that for the FCPM case, the experimental results agree quite well with the theoretical calculations. The dip at 65 cm^{-1} is mainly caused by the dispersion of α_3 which has absorption peaks around 65 cm^{-1} superimposed on the slope of the strong infrared mode at 152 cm^{-1}.[26]

In the BCPM case, because of the frequency dependent far-infrared loss through the hole on the collecting brass light pipe (see Section IIIB(3)) and 5 cm of air in the collection path, the data were difficult to calibrate precisely. The experimental results did not agree well with the theoretical calculation. However, we still see the severe drop in power at low frequency side and this might be due to the laser divergence effect as in the FCPM case. The theoretical calculation curve in the BCPM case, which predicts a factor of two times that of the FCPM case, comes close to the FCPM curve on the low frequency side. This is caused by the average over different Δk values in $\bar{I}$ (Δk from 0 to 82.9 cm^{-1} for FCPM and from 0 to 165.8 cm^{-1} for BCPM including the linewidth effect) in the region where α_3 is small.

In the NCPM case, a 4-mm cube of $LiNbO_3$ was used with one corner cut off at 68° to let the generated far-infrared out (see Fig. 12). Noncollinear phase-matching of far-infrared generation was achieved by varying angles ψ (outside the crystal) and ϕ (inside the crystal)

from 0.81° to 4.60° and from 65.11° to 73.08° respectively.[33,34] The far-infrared output in this case should be strongly affected by the divergence of the input beams. The theoretical curve for NCPM in Fig. 18 was therefore the average over Δk from 0 to 137 cm^{-1}, which was appropriate for our 4 m rad beam divergence at the crystal. With ℓ_{eff} = 0.5 mm, it fits the experimental data very well except at the point w_3 = 160 cm^{-1} where the signal-to-noise was the poorest and where we were near the maximum translation range of the prism (see Fig. 12). The steady decrease in the far-infrared signal with w_3 above 55 cm^{-1} (where $\alpha_3\ell_{eff} >> 1$ and ℓ_{eff} is not an important parameter) is due to the increasing e-ray absorption.[26] The decrease on the low frequency side is caused by the laser divergence and the w_3^2 radiation efficiency factor. Note that far-infrared spreading angle (γ' as defined in Fig. 9(b)) caused by the laser beam divergence is only 5.0° at w_3=20 cm^{-1} in this case. The generated far-infrared radiation should be the same as detected.

The NCPM scheme generates more far-infrared power than the FCPM scheme for two basic reasons. First, since $\chi_{33}^{(2)} \cong \chi_{24}^{(2)}$,[32] $\chi_{eff}^{(2)}$ for FCPM is reduced by a factor of $\sin\theta$, which decreases at low frequencies. Second, the FIR e-ray generated with NCPM has a lower absorption coefficient than the FIR o-ray generated with FCPM.

Finally, the dispersion of $\chi_{24}^{(2)}$ as a function of w_3 is shown in Fig. 19. The experimental values were obtained from the FCPM results shown in Fig. 18. The standard error bars were deduced from the observed power deviation and the standard deviation of α_3 shown in

Fig. 17. For the theoretical calculation, we used Eqs. (35), (36), and (37) and the data as listed in Table IV. The agreement between the experiment and the theoretical calculation is reasonable. The dispersion of $\chi_{33}^{(2)}$ was not plotted because we could not deduce the values of α_3 for the e-ray in the mixing experiment.

D. Conclusions and Discussions

1. Conclusions

We have investigated the phase-matched far-infrared generation by optical mixing of two dye laser beams under three different experimental schemes in five different crystals. We used sum frequency generation by reflection from an InAs surface for normalization. Using $LiNbO_3$ as a mixing crystal, we have observed the tunable far-infrared radiation from 20 to 127 cm^{-1} in the FCPM scheme, from 20 to 95 cm^{-1} in the BCPM scheme, and from 40 to 160 cm^{-1} in the NCPM scheme. The observed far-infrared power as a function of w_3 in both the FCPM and NCPM schemes agreed quite well with theoretical calculations derived from the plane-wave approximation with several modifications which were relevant to our experimental conditions. The observed far-infrared power as a function of w_3 in the FCPM scheme did not agree with the theoretical calculation because of the uncertainty and difficulty in our far-infrared collection system. We conclude that the finite laser beam divergence has detrimental effects on the far-infrared generation in the NCPM scheme and in both the FCPM and BCPM schemes at low frequencies. We have also investigated forward collinear phase-matching in ZnO, ZnS, CdS and CdSe at selected frequencies,

among which ZnO is the best crystal.

We have demonstrated a way of measuring the FIR absorption constant as high as 845 cm^{-1} using the phase-matching curves in the FCPM and BCPM experiments. Our measured FIR absorption constants with FCPM deviated from the FIR transmission measurement of Bosomworth and the infrared reflection measurement of Barker and Loudon. We also observed the FIR bandwidth of 3 cm^{-1} from the phase-matching curve with FCPM. We have deduced the dispersion of $\chi_{24}^{(2)}$ of $LiNbO_3$ from the FCPM experiment. It was consistent with the theoretical calculation.

Compared with the FCPM scheme, the NCPM scheme requires only one crystal for operation over a wide frequency range but needs two angular adjustments to orient the crystal for phase-matching. It generates more FIR power than the FCPM scheme in $LiNbO_3$. The single-dye-cell experimental scheme (see Fig. 10) which could be used for both the collinear and noncollinear phase-matching was rather single and very convenient to operate in comparison with two-dye-cell schemes. Compared with the other FIR generation experiments using CO_2 lasers, our dual-frequency one-dye-cell scheme is attractive because of the ease with which temporal and spatial overlap of the two input beams is obtained. It also has the advantage of a large continuous tunability and the use of room temperature mixing crystals.

2. Discussion

Ushioda, et al.[60] has reported the observation of the structure of the FIR absorption constant in GaP, using small angle Raman scattering. He associated this structure with the two phonon density of

states. In this thesis, we lack the identification of the sources which caused the strong FIR o-ray absorption around $w_3 = 65\ cm^{-1}$. It was either due to the local phonon modes of certain impurities or incurred by the multi-phonon processes. We could not identify its relation with two phonon density of states since, to the best of my knowledge, no neutron scattering experiments or other experiments have been done to find out the phonon dispersion curves of $LiNbO_3$. Further research is needed to see if using the difference frequency generation experiment one can extract the information of the two phonon density of states for the mixing crystals.

In this thesis, we have not answered the question of whether the FIR diffraction might shorten the crystal coherence length as derived from the plane-wave approximation. Another experiment, focusing two TEM_{∞} Gaussian laser beams with narrow linewidth, is worth performing. The observation of the FIR output as a function of how hard we focus the beams should help to resolve this mystery.

There are opportunities for further research along the following lines:

a. As a device to do FIR spectroscopy

The FIR bandwidth of $3\ cm^{-1}$ can be narrowed by applying intracavity beam expanding telescopes to effectively use larger areas of the gratings. About a 0.1 Å bandwidth[62] of the dye laser beam can be achieved by using a diffraction grating and a telescope inside the cavity. For further narrowing, in addition, a tilted Fabry-Perot etalon should be placed inside the cavity with a sacrifice of laser

output power. The use of better far-infrared detector is possible and rewarding. A Josephson junction bolometer, which has an NEP (noise-equivalent-power) as low as 5×10^{-15} W/$\sqrt{\text{Hz}}$ reported by Clarke, et al.,[63] appears very promising. A germanium bolometer with an electrical NEP of 2×10^{-14} W/$\sqrt{\text{Hz}}$ [64] will improve the far-infrared detection about three orders of magnitude provided that the amplifier noise can be improved to that degree also.

Since the laser technology is developing rapidly, there always exists the opportunities of using better laser sources for the mixing experiment. We have verified that the dual-frequency dye laser system shown in Fig. 10 can be operated with flashlamp-pumped rhodamine 6 G dye laser, although the dye laser output of our system was still insufficient to generate detectable FIR in the mixing experiment. However, a flashlamp-pumped dye laser system of 100 kW peak power and 1 μs pulsewidth could yield the same FIR signal for each pulse as our laser pumped system with 600-kW peak power and 30 ns pulsewidth. Because a repetition rate greater than 1 pulse/sec is possible with such a dye laser, the dual-frequency single dye cell scheme described here should make a very useful source for FIR spectroscopy.

It is also a matter of time and effort to develop mixing crystals with better properties. An ideal crystal would be transparent to the lasers, have very small absorption for the far-infrared, have large nonlinear susceptibilities (or large electro-optical constants), be easily obtainable in good quality large crystals, and be highly resistent to optical damage. It has been reported that the ammonium oxalate crystal $[(NH_4)_2C_2O_2\cdot H_2O]$[65] has electro-optical coefficients

r_{41} = 680, r_{52} = 980, and r_{63} = 750 ($\times 10^{-8}$ e.s.u.) and the strontium barium niobate crystal ($Sr_{0.7}Ba_{0.25}Nb_2O_6$)[66] has electro-optical coefficient $r_{33} = 4020\times 10^{-8}$ e.s.u. Compared to $LiNbO_3$ with $r_{33} = 92.8\times 10^{-8}$ e.s.u., these two crystals should improve the far-infrared output two to three orders of magnitude if their FIR absorption constants are less than that of $LiNbO_3$. A piece of ammonium oxalate crystal was grown and, though it was not good enough in optical quality for the mixing experiment, it was used for a rough FIR absorption measurement. Its FIR absorption constant was much lower than that of $LiNbO_3$ at low frequencies (e.g., $\alpha_3 = 10\ cm^{-1}$ at $w_3 = 42\ cm^{-1}$). Another advantage of using crystals of large nonlinear susceptibility is that the far-infrared radiation can be generated with reasonable power output without phase-matching in the collinear scheme. Thus, the angular rotation of the mixing crystal for phase-matching can be avoided and only the tuning of the laser grating is needed to achieve the tunable far-infrared radiation. Auston et al.[12] have used the reduced $LiNbO_3$ (by N_2 and H_2 mixture) to generate tunable FIR radiation from 2 to 50 cm^{-1} in the collinear scheme without phase-matching. The second-order nonlinear susceptibility of the reduced $LiNbO_3$ is enhanced by the strong absorption of the laser beams due to the dipole moment of the absorbing centers upon excitation and the pyroelectric polarization which accompanies the subsequent thermalization of the excitation. Looking for better crystals is an area of further research.

b. The investigation of the nonlinear optical properties of materials.

Van Tran Nguyen and T. J. Bridges[8] have observed an enhancement of second-order nonlinearity when the far-infrared difference frequency w_3 was tuned to that of the spin-flip (magnetic dipole) mode caused by the conduction-electron spin in the magnetic field. In the experiment, they mixed two CO_2 lasers in an n-type InSb in a strong magnetic field. Terrence L. Brown and P. A. Wolff have specifically explained this nonlinear spin-resonance effect caused by the spin-flip mechanism. Note that our calculation of the dispersion of $\chi^{(2)}$ using Eqs. (34), (35), and (36) for the polariton modes can be generalized for this case and for the anti-ferromagnetic resonance case. As pointed out by Shen,[67] the effective dielectric constant for the spin-flip case (InSb in magnetic field) can be expressed as

$$(\varepsilon_3)_{eff} = \varepsilon_3(1+4\pi\,\chi_m^{(1)}) \simeq \varepsilon_3 \left[1 - \frac{N(g\mu_B)^2\pi}{\hbar(w_3-w_o+i\Gamma)}\right] \tag{47}$$

where ε_3 is the complex dielectric constant without magnetic field including a polariton mode at $w_{T_o} = 183\ cm^{-1}$, $\chi_m^{(1)}$ is the magnetic susceptibility, N is the number of condution-electron per unit volume, g is the Laudon g-factor, μ_B is the Bohr magneton and w_o is the spin-flip frequency. In evaluating the corresponding oscillator strength for the spin-flip mode, we set $(\varepsilon_3)_{eff}$ in Eq. (47) equal to

$$(\varepsilon_3)_{eff} = \varepsilon_3 - \frac{Sw_o}{(w-w_o)+i\Gamma} \tag{48}$$

The equations (47) and (48) imply that

$$S = \varepsilon_3 N(g\mu_B)^2 \pi/\hbar w_o \tag{49}$$

Note that S includes ε_3 in Eq. (49). Using Eqs. (35), (36) and (49), we obtain the second-order nonlinear susceptibility on the spin-flip resonance in the form

$$\frac{1}{2}\ \chi_S^{(2)}(w_3=w_o) = d_S(w_3=w_o) = \frac{Sd_\theta}{4\pi}\ \frac{w_o}{\Gamma} + d_{N.M.} \tag{50}$$

where $d_{N.M.}$ denotes the nonlinearity when there is no magnetic field present. The spin-flip resonance nonlinearity denoted by the first term on the right hand side of Eq. (50) is equal to 4.3×10^{-6} e.s.u. taking $g = 40$, $\Gamma = 0.1\ cm^{-1}$, $w_o = 90\ cm^{-1}$, $w_s = 1000\ cm^{-1}$, $n_p \cong n_s$, $\bar{n}_{T_j} = 0$ (at 15°K), $N = 2.2\times10^{15}\ cm^{-3}$, and $S_{ex,j}/Ld\Omega = 0.2\times10^{-23}\ cm^{-1}sr^{-1}$.[68,69] This value is in good agreement with Brown's result of 4.1×10^{-6} e.s.u. and Shen's result of 4.5×10^{-6} e.s.u. while $d_{N.M.}$ is equal to 5×10^{-7} e.s.u.[8]

Another interesting case is the enhancement of second-order nonlinearity due to the anti-ferromagnetic resonance of 37 cm^{-1} in CoF_2. The absorption constant α_3[70] of 150 cm^{-1} on resonance was measured by far-infrared laser spectroscopy. From Eq. (48), we can relate α_3 to the oscillator strength by

$$\alpha_3 = \frac{1}{\sqrt{\varepsilon_3}}\ \frac{w_o}{c}\ \mathrm{Im}(\varepsilon_3)_{eff} = \frac{1}{\sqrt{\varepsilon_3}}\ \frac{w_o}{c}\ S\ \frac{w_o}{\Gamma} \tag{51}$$

where $\mathrm{Im}(\varepsilon_3)_{eff}$ represents the imaginary part of $(\varepsilon_3)_{eff}$. We evaluate $S = 0.085$ by taking $w_o = 37\ cm^{-1}$, $\Gamma = 1.35\ cm^{-1}$,[71] and $\varepsilon_3 = 6.1$.[72]

In order to evaluate $d_{\theta j}$ in Eq. (36), we take the values $n_p = n_s$, $\bar{n}_{T_j} \simeq 0$ (T = 4°K), $w_s = 1.58\times10^4$ cm^{-1} (He:Ne laser), and $S_{ex',j}/Ld\Omega = 0.27\times10^{-9}$ cm^{-1}sr^{-1}.[73] The second-order nonlinearity on resonance $\frac{Sd_\theta}{4\pi}\frac{w_o}{\Gamma}$ is equal to 5.13×10^{-8} e.s.u. Since CoF_2 is a centro-symmetric crystal, there is no electric-dipole-type polariton mode. The spin-opitcal phonon mode (E_g)[73,74] which is simultaneously infrared active and Raman active is at the frequency of 256 cm^{-1}. The contribution of that mode to the second-order nonlinearity is estimated to be less than 1×10^{-8} e.s.u. at low frequencies (<< 256 cm^{-1}). The electronic state contribution (e.g. d_E in Eq. (36)) to the second-order nonlinearity vanishes because of centro-symmetric crystal in CoF_2. Hence, the far-infrared output generated in CoF_2 around $w_3 = 37$ cm^{-1} (near AFMR) will be at least three orders of magnitude less than that produced in $LiNbO_3$ with FCPM.

In this thesis, we have demonstrated both in theory and in experiment that we can investigate the second order nonlinearity of the crystals using two-laser mixing. Such investigation can be carried further and it provides an important guidance to choose better crystals to generate tunable far-infrared radiation for the purpose of doing spectroscopy.

Table I

$LiNbO_3$

Source	θ	$\phi^{\dagger}$	Thickness	Experiments
Crystal technology (0.5×0.5×3 cm)	15°,25°,35°,45°, 55°,65°	0°	0.65 mm	FCPM & BCPM
Crystal technology (4 mm cube)	with one corner cut off			NCPM
Hansen Microwave Lab.	16°	0°	1.6 mm	FIR linewidth measurement

*Diamond abrasive of 1 μ size was used for the final optical polishing.

†ϕ is the angle between the a-axis and the plane containing the c-axis and k-wavevector.

Table II

Other Crystals

Crystal	P(Ω/cm)	θ	Thickness	Experiments
ZnO*	2×10^4	90°	1 mm	FCPM
CdS*	1.5	90°	1 mm	FCPM
ZnS*		90°	1 mm	FCPM
CdSe†	$0.1, 10^2$	90°	1 mm	FCPM

*Already well polished

†Cleaved from bulk samples and finally polished by Al_2O_3 1μ abrasive.

Table III

Summary of the mixing experiments on five different crystals

Crystals	Tunable range	Power (Frequency observed)
$LiNbO_3$	20 to 127 cm^{-1} (FCPM)	see Fig. 18
	20 to 95 cm^{-1} (BCPM)	≈ twice that of FCPM
	40 to 160 cm^{-1} (NCPM)	see Fig. 18
ZnO*	⩽ 190 cm^{-1} (FCPM)	14 mW (190 cm^{-1})
CdS*	⩽ 180 cm^{-1} (FCPM)	3 mW (180 cm^{-1})
ZnS*	⩽ 91 cm^{-1} (FCPM)	0.74 mW (91 cm^{-1})
CdSe*	⩽ 150 cm^{-1} (FCPM)	< 0.15 mW† (150 cm^{-1})

*Crystal thickness 1 mm

†Less than the detector noise level

Table IV

The data of infrared and Raman scattering measurements used to calculate the dispersion of $\chi_{24}^{(2)}$ in $LiNbO_3$. The polariton modes are E modes and $\chi_{24}^{(2)}(w_3=0)=3.74\times10^{-6}$ e.s.u. is the value associated with the argon laser at 4885 Å (not dye laser) which was the input beam for the measurement of Raman scattering cross-sections.

w_{T_j} (cm^{-1})	S_j	γ_j (cm^{-1})	$S/Dd\Omega\cdot10^6$ ($cm^{-1}sr^{-1}$)	$d_{\theta j}\cdot S_j\times10^6$ e.s.u.
152	22.0	14	3.8	11.0
236	0.8	12	2.9	1.85
265	5.5	12	0.54	1.83
322	2.2	11	0.96	1.48
363	2.3	33	0.94	1.46
431	0.18	12	0.39	0.25
586	3.3	35	2.2	2.2
670	0.2	47	0.04	0.07

CHAPTER II

I. INTRODUCTION

The techniques of using piezoelectric transducers to generate coherent monochromatic phonons at microwave frequencies become very inefficient as the frequency approaches 50 GHz. Because of the cancellation of the sound energy produced from different parts of the crystal, the effective interaction volume between the electric field and the sound wave becomes very small at high frequencies. The small effective interaction volume results in a low conversion efficiency. The highest frequency of coherent phonon generated by driving a piezoelectric crystal in a microwave cavity was at 114 GHz, an experiment done by J. Ilukor and E. H. Jacobson.[75] The conversion efficiency, however, was lower than 10^{-8}. Phonon experiments at frequencies in excess of 50 GHz have generally used incoherent heat pulse techniques[76,77] or, more recently, phonon fluorescence[78] in superconductors which provides a relatively intense noncoherent phonon source at the energy-gap frequency.

In this chapter, we examine the feasibility of generating high frequency coherent phonons in periodic superlattices by optical means. Because of the periodicity of a superlattice, coherent phase-matched generation of phonons by umklapp processes can occur at frequencies which would be prohibited in a homogeneous material. Direct conversion of photons into phonon is possible through the first-order interaction if the superlatttice is piezoelectric, as suggested by Bloembergen and Sievers.[79] This is the case in multi-layer epitaxially grown

crystals,[80,81] in partially oriented sputtered films,[82,83] or in polytypic crystals[84] as SiC in which a superlattice of periodicity as large as 1500 Å has been observed.

The second-order interaction between sound and light involves the electrostrictive constants of the medium. In a single crystal or uniform medium, the Brillouin and stimulated Brillouin scatterings using electrostrictive constants can generate phonons whose highest achievable frequency is restricted by the maximum momentum transfer of twice the photon momentum. Unless intense laser sources with wavelengths shorter than that of ultraviolet light are available, this frequency is usually less than 50 GHz. In addition, the phonon spectrum generated by Brillouin scattering has a broad bandwidth and a very low intensity. By constructing a superlattice, the electrostrictive interaction would permit coherent phonon generation by stimulated Brillouin scattering or by two laser mixing. Stimulated Brillouin scattering is not favorable for high-frequency phonon generation in a superlattice. High-order umklapp precesses have larger phonon attenuation constants and so larger thresholds for stimulated Brillouin scattering than the zero-order process. Unless specially designed cavities are used to discriminate against the zero-order umklapp process, stimulated Brillouin scattering in a superlattice would thus produce only the same low-frequency phonons as in a uniform medium. The only attractive way to generate high frequency coherent phonons by the second-order process in a superlattice appears to be the electrostrictive beating of the two laser beams at their difference frequency. Single crystals

are not required for this process, so that superlattices constructed by sputtering[82] or vacuum deposition[83,85] can be used.

In this chapter, we present the detailed calculations of phonon power generated by both first and second order processes. In Section II, we discuss the direct conversion of millimeter or submillimeter wave photons into phonons at the same frequency in a piezoelectric superlattice. Conversion efficiency as high as 10^{-4} in a 100-layer GaAs:GaP superlattice is achievable. The effect of the random errors in the periodicity of the superlattice on the generated phonon power was estimated with the assumption that wave functions with Bloch's form for both sound and light were still valid. In Section III, we calculated the generation of high frequency coherent phonons by the second order electrostrictive process of mixing two laser beams. The calculated efficiency suggests that the 1 mW phonon power can be obtained by the mixing of two 10^7 W/cm^2 ruby laser beams in a one-hundred layer superlattice 8.7 μ-thick. The effect of random errors in the periodicity of the superlattice is also discussed. In Section IV, the summary of the calculations, the experiments done in this field, the discussion of the material problems related to the construction of a superlattice as well as the future experiments will be presented.

II. FIRST ORDER INTERACTION VIA PIEZOELECTRIC EFFECTS

If the superlattice is composed of partially oriented alternating thin films, direct conversion of photons into phonons is possible via piezoelectric effects. Consider a superlattice with alternating crystal layers of thickness d_1 and d_2, respectively. High-frequency transverse phonon waves propagating along the x axis perpendicular to the layers can be generated at discrete frequencies by a far-infrared field E which is governed by the equation

$$P_i \frac{\partial^2 u}{\partial t^2} - \frac{\gamma_i}{2} \frac{\partial u}{\partial t} - T_i \frac{\partial^2 u}{\partial x^2} = \frac{\partial}{\partial x} (e_i E) \tag{52}$$

where i = 1 or 2 indicates the two different crystal layers, and P_i, γ_i, T_i and e_i are the density, the acoustic damping, the elastic stiffness, and the piezoelectric stress constants, respectively. The coupled far-infrared field satisfies the following equation

$$\frac{\partial^2 E}{\partial x^2} - \frac{\varepsilon_i}{c^2} \frac{\partial^2 E}{\partial t^2} = \frac{4\pi}{c^2} \frac{\partial^2}{\partial t^2} (e_i \frac{\partial u}{\partial x}) \tag{53}$$

where ε_i (i = 1 and 2) are the dielectric constant of the two different crystal layers. Since we are interested in the sound frequency above 100 GHz that corresponds to a superlattice with unit-cell thickness of 500 Å for the first order umklapp process, the number of atoms in such a unit cell is so large that the exact calculation of polariton modes[86] is extremely difficult. However, we can estimate the polariton effect due to the superlattice by solving Eqs. (1) and (2) in the long-wave limit of the electric field. The dispersion of the dielectric constant can be easily obtained as

$$\varepsilon(\omega) = \bar{\varepsilon} + \sum_n \frac{4\pi\bar{e}^2 G^2/\bar{\rho}\omega_{Tn}^2}{1 - \frac{\omega^2}{\omega_{Tn}^2} + i\frac{\bar{\gamma}}{2\bar{\rho}}\frac{\omega}{\omega_{Tn}^2}} \tag{54}$$

where $G = \frac{2\pi}{d_1+d_2}$, the reciprocal unit vector of the superlattice, ω_{Tn} is the nth polariton mode which is roughly equal to $n\bar{v}G$, and $\bar{v}$ is the averaged sound velocity of two crystal layers in a unit cell. The physical constant with a bar over it in Eq. (54) denotes the averaged value of corresponding constants in a unit cell (e.g. $\bar{\varepsilon} = (\varepsilon_1+\varepsilon_2)/2$ and so forth). From Eq. (54), we can obtain the oscillator strength $4\pi\bar{e}^2G^2/\bar{\rho}\omega_{Tn}^2$ for nth polariton mode due to the superlattice in the order of $10^{-3}/n^2$.[87] However, the corresponding phonon damping term $\frac{\bar{\gamma}}{2\bar{\rho}}\frac{\omega}{\omega_{Tn}^2}$ is in the order of $10^{-3}n$ for a superlattice below 10°K which is the temperature we will assume for the rest of the calculations. Hence the ratio of the oscillator strength to the corresponding phonon attenuation term is small compared to the optical dielectric constant so that the polariton effects due to the superlattice can be neglected.

We shall assume that the over-all thickness of the superlattice is small enough that the far-infrared power is not depleted appreciably in the conversion. The undepleted far-infrared field in a periodic medium should have the Bloch form $E = \mathcal{E}(x)\exp(ikx-iwt)$ with $\mathcal{E}(x) = (x+nd)$, where $d = d_1+d_2$ and n is an integer. This function $\mathcal{E}(x)$ and the reduced wave vector k can be obtained from the homogeneous wave equation with the boundary conditions for the given layer structure.[88]

If the wavelength of the far-infrared field is much larger than d, then $\varepsilon(x) \simeq$ constant. Similarly, without the driving field the acoustic wave should also have the Bloch form $U = u(x)\exp(iqx-iw_q t)$ where $u(x)=u(x+nd)$. With the driving field in Eq. (51), the acoustic wave can be written as $U = A(x)u(x)\exp(iqx-iw_q t)$, where the amplitude function $A(x)$ is a monotonically increasing function of x. If $A(x)$ is slowly varying that

$$q\left|\frac{\partial A}{\partial x}\right| >> \left|\frac{\partial^2 A}{\partial x^2}\right| \tag{55}$$

then Eq. (1) can be written as

$$\frac{\partial A}{\partial x} = -\frac{\partial(eE)}{\partial x}\exp(-iqx)\left[2T\left(iqu(x) + \frac{\partial u}{\partial x}\right)\right]^{-1} \equiv f(x) \tag{56}$$

The solution of the above equation is

$$A(Nd) = M(F_1+F_2)$$

$$M = \{1-\exp[i(k-q)Nd]\}/\{1-\exp[i(k-q)d]\}$$

$$\left.\begin{aligned} F_1 &= \int_{\varepsilon}^{d_1-\varepsilon} f(x)\,dx + \int_{d_1+\varepsilon}^{d_1+d_2-\varepsilon} f(x)\,dx \\ F_2 &= \int_{d_1-\varepsilon}^{d_o+\varepsilon} f(x)\,dx + \int_{d_1+d_2-\varepsilon}^{d_1+d_2+\varepsilon} f(x)\,dx \end{aligned}\right\} \text{Lim } \varepsilon \to 0 \tag{57}$$

where F_1 is the contribution from the fulk and F_2 is the contribution from the discontinuous boundaries between layers and N denotes total number of unit cells in a superlattice.

From Eq. (57), it is seen that if $k = q$, then $M = n$ is a maximum. This phase-matching condition can be satisfied at many different phonon frequencies in a superlattice, whenever in the reduced zone scheme the photon dispersion curve crosses the phonon dispersion curve. Physically, the phase-matched generation of phonons at various frequencies with the same wave vector corresponds to different orders of Umklapp processes. With a small phase mismatch $\Delta k = k-q$, we have $|M| = \sin(\Delta kNd)/\sin(\Delta kd)$.

As an example, we consider a superlattice of 100 epitaxial GaAs:GaP layers normal to the [111] axis. The incoming em field propagating along [111] is polarized along $[0\bar{1}1]$. We choose $d_1 = 280$ Å and $d_2 = 354$ Å so that $d_1/v_1 = d_2/v_2$, where v_1 and v_2 are the sound velocities in GaAs and GaP respectively. In this configuration, we obtain the piezoelectric stress constant $e = E/\sqrt{3}\, c_{44}d_{14}$, and d_{14} is the piezoelectric strain constant. We also obtain for Eq. (1) $T = \frac{1}{3}(c_{11}+c_{44}-c_{12})$ where c_{ij} are the elastic stiffness constants. The Bloch form solutions of the homogeneous far-infrared field equation take the forms

$$\begin{aligned} \varepsilon(x) &= a_1 e^{i(\alpha-k)x} + b_1 e^{-(\alpha+k)x} \qquad 0 \leqslant x \leqslant d_1 \\ &= a_2 e^{i(\beta-k)x} + b_2 e^{-(\beta+k)x} \qquad d_1 \leqslant x \leqslant d \end{aligned} \tag{58}$$

where $\alpha = \frac{\omega}{c}\sqrt{\varepsilon_1}$, $\beta = \frac{\omega}{c}\sqrt{\varepsilon_2}$ and a_1, b_1, a_2 and b_2 are constants which are related to each other through four homogeneous equations[88] by imposing the conditions of continuity and periodicity on $\varepsilon(x)$ at $x = d_1$

and d. Equating the determinant of these four equations to zero yields the dispersion equation determining k

$$\cos kd = \cos\alpha d_1 \cos\beta d_2 - \frac{\varepsilon_1+\varepsilon_2}{2\sqrt{\varepsilon_1\varepsilon_2}} \sin\alpha d_1 \sin\beta d_2 \tag{59}$$

This equation determines the ω versus k dispersion relation and the forbidden gaps for light propagating in the superlattice. As the result of four homogeneous equations and the dispersion relation, only a_1 in Eq. (58) is an independent variable whose value can be calculated by matching the boundary conditions at the input boundary of the superlattice.

The Bloch form solutions for the homogeneous sound wave u(x) have the same forms as in $\varepsilon(x)$

$$\begin{aligned} u(x) &= L_1 e^{i(k_1-q)x} + R_1 e^{-i(k_1+q)x} \qquad 0 \leqslant x \leqslant d_1 \\ &= L_2 e^{i(k_2-q)x} + R_2 e^{-i(k_2+q)x} \qquad d_1 \leqslant x \leqslant d \end{aligned} \tag{60}$$

where

$$k_1^2 = \frac{\omega^2}{v_1^2} + \frac{\gamma_1}{2T_1} i\omega, \quad k_2^2 = \frac{\omega^2}{v_2^2} + \frac{\gamma_2}{2T_2} i\omega \quad \text{and } L_1, R_1,$$

L_2 and R_2 are constants as in the far-infrared field case. The sound dispersion relation is determined by the equation

$$\cos qd = \cos k_1 d_1 \cos k_2 d_2 - \frac{z_1^2+z_2^2}{2z_1 z_2} \sin k_1 d_1 \sin k_2 d_2 \tag{61}$$

where $z_1 = \rho_1 v_1$ and $z_2 = \rho_2 v_2$ are sound impedances for GaAs and GaP respectively.

Substituting Eqs. (58) and (60) into (57), we can obtain A(Nd). The sound power generated can be expressed as

$$P_S \cong \frac{1}{2} T_2 v_2 |A(Nd)|^2 q^2 |u(d)|^2 \tag{62}$$

We have calculated the conversion efficiency (generated sound power divided by the input far-infrared power) as a function of discrete phonon frequencies corresponding different order of umklapp processes. The physical constants and the computer program used for the calculation is shown in Appendix C. The result of this calculation is shown in Fig. 20. Here, unless $d > 50\ \mu$, F_1 in Eq. (57) can be neglected in comparison with F_2. From Fig. 21, it is seen that the odd-order umklapp processes have large conversion efficiencies ($\sim 10^{-4}$). This is because the phonon waves generated at the successive boundaries between layers are in phase. For the even-order umklapp processes, they are out of phase. We have assumed in the calculation that the piezoelectric constant is independent of frequency and the discontinuities between layers are infinitely sharp. Therefore, the conversion efficiencies for the odd-order and the even-order Umklapp processes separately have no appreciable dependence on frequency. If the discontinuities between layers spread over a distance comparable to the phonon wavelength, then phase cancellation occurring within the boundaries will decrease the conversion efficiency.

In reality it is very difficult to manufacture a perfect superlattice with an exact periodicity for 100 layers. It is important to

know the effect of the random errors in the periodicity on the phonon power produced. For simplicity, we assume an equal probability of making the thickness of each layer accurate to within certain percentages. The imperfection of the periodicity will modify the homogeneous sound wave function as described in Eq. (60) and the homogeneous far-infrared wave function as expressed in Eq. (58). It will also change the integration limit for each layer in the processes of obtaining A(Nd) from Eq. (56). As a first-order approximation, we assume the imperfection of the periodicity does not effect the Bloch form wave function for sound as well as for light so that the constants $a_{1,2}$, $b_{1,2}$ in Eq. (58) and $L_{1,2}$, $R_{1,2}$ in Eq. (60) are fixed values. Integrating f(x) in Eq. (56) through layers of certain randomness in thickness, we easily obtain the following formula

$$\bar{A}\ (Nd) = \frac{1}{\Delta d_1} \int_{d_1-\Delta d_1}^{d_1+\Delta d_1} \left[\frac{1}{\Delta d} \int_{d-\Delta d}^{d+\Delta d} M(F_1+F_2)\,dy \right] dz \qquad (63)$$

where y and z are dummy variables and represent the replacements for d_1 and d contained in $M(F_1+F_2)$ respectively. Furthermore, assuming $\frac{\Delta d_1}{d_1} = \frac{\Delta d}{d}$, the percentage random error in thickness is the same for each layer. When the phase-matching condition (i.e., q=k) is satisfied, M in Eq. (63) is equal to N (the number of unit cells in the superlattice) which can be taken out of integration. The computer calculation of $\frac{\Delta d}{d}$ = 2% for the numerical example of GaAs:GaP superlattice is listed in Appendix C. The results are shown in Fig. 20. The random variation tends to decrease the phonon power at points of

high conversion efficiency, and increases the phonon power at points where the efficiency is low due to cancellation. The high-order umklapp processes which involve shorter phonon wavelengths are more sensitive to such imperfection as one would expect.

III. SECOND-ORDER INTERACTION VIA ELECTROSTRICTIVE COUPLINGS

When a superlattice possesses inversion symmetry as in the alternating thin films of vacuum deposition, all the piezoelectric constants are zero. The only attractive way to generate high-frequency coherent phonons in such a superlattice is through the electrostrictive mixing of two laser beams. Consider two laser beams at frequencies w_1 and w_2 mixing in a superlattice of alternating thin films to generate high-frequency longitudinal phonons. We assume that the two beams propagating along x have the same polarization. Then the phonon generation is again described by Eq. (52) but with the driving term replaced by $(\frac{\partial}{\partial x})(\varepsilon_o{}^2 P E_1 E_2{}^*/4\pi)$, where ε_o is the optical dielectric constant, and P the stress-optical constant. A similar solution to Eq. (57) can also be obtained by assuming negligible depletion of laser power.

As a numerical example, we consider a superlattice composed of 100 vacuum-deposited KCl:CdS layers with d_1 = 420 Å and d_2 = 450 Å so that again $d_1/v_1 = d_2/v_2$. The homogeneous wave functions for the two laser beams and the dispersion relation can be obtained from Eqs. (58) and (59) respectively. The homogeneous wave function and the dispersion relation for sound are described by Eqs. (60) and (61) respectively. The detailed computer calculation is included in Appendix D. The calculated phonon power is shown in Fig. 21 as a function of the discrete phonon frequencies corresponding to various umklapp processes. For odd-order umklapp processes, F_2 in Eq. (57) is the dominant effect as in the piezoelectric case. We note that even for high-order umklapp processes, the phonon power generated

by two 10 mW/cm^2 laser beam can be as high as 5 mW provided that the discontinuities between layers spread over a distance much smaller than the sound wavelength. For even-order umklapp processes, the dominant contribution to the sound power is from F_1 in Eq. (57), since the two terms in F_2 are out of phase. The effect of a ±2% random variation in the period of the superlattice is also shown in Fig. 21. The computer calculation is listed in Appendix D. Again, the high-order umklapp processes are more sensitive to such imperfection.

IV. DISCUSSIONS AND CONCLUSIONS

From our calculations, we see that the phonon pulse generated at the discontinuous boundary between layers is the dominant process for both the first and second order interactions. This is not surprising because the generation of phonon using the discontinuity between vacuum and a quartz crystal was observed first by Ilukor and Jacoksen. They employed a $TM_{3,4,8}$ mode rectangular cavity which was completely filled with a big piece of crystal quartz to generate the coherent hypersonic wave of the highest frequency at 114 GHz.

We did not treat the optical umklapp processes (resulting from the periodic index of refraction for light) and the acoustic umklapp processes (coming from the periodical acoustic properties of a superlattice) separately in our calculations. Note that our general formulas are valid for a superlattice which is either periodic in sound or periodic in light as well as periodic in both sound and light. However, in direct conversion of photons into phonons, the optical umklapp processes are negligible because the wavelength of the far-infrared field is much longer than the period of the superlattice. The acoustic umklapp processes are dominant in this case so that it is important to have a superlattice which is periodic in sound. In the second-order interaction case, the optical umklapp processes are as important as the acoustic umklapp processes since the wavelengths of the input laser beams are comparable to the period of the superlattice. A medium which has a spatial modulation of the refraction index can be used to generate high frequency phonons by the mixing of two laser

beams. For example, a gelatin film[89] (on a glass substrate) was exposed to the interference pattern produced by two coherent laser beams. After exposure the gelatin was developed using techniques which are well-known in holography[90] and which result in a spatial modulation of the index refraction. This gelatin is a superlattice for the input laser beams and can be used to generate coherent phonons by optical umklapp processes only.

To make a piezoelectric superlattice of about 100 layers by molecular beam epitaxial vapor deposition[81,82] is still a formidable job. Recently, Chang and Esaki et al.[91] reported the manufacture of a superlattice of 100 unit cells with each cell consisting of a GaAs layer about 60 Å thick and a $Ga_{0.5}Al_{0.5}As$ layer about 20 Å thick. Time and effort will be required to make a superlattice of more than 100 unit cells with periodicity within 1 or 2% accuracy. An easier way to make a piezoelectric superlattice is by alternating sputtering[83] of thin films with materials like CdS, ZnS, ZnO, PZT (lead-zirconate-titanate) and the niobates and tantalates of the alkali metals. Since most of those materials have hexagonal symmetry, a proper choice of the c-axis with respect to the superlattice axis can facilitate the generation of both the longitudinal and transverse phonons[83] using one superlattice. Nature even provides us polytypic crystals[84] like SiC, CdI_2 which are superlattices in crystal forms. Polytypic silicon carbide crystal is well-known being a superlattice with unit cell as large as 1500 Å (type 594R).[92] The phonon modes (corresponding to different orders of umklapp processes) of 4H,[93] 6H,[94] 15R,[95] 21R and 33R[96] SiC have been studied by Patrick and Choyke et al. Those are good for very high frequency phonon generation (> 270 cm^{-1}) by

direct absorption of far-infrared photons. By choosing polytypic SiC with large unit cell as in the types 192R,[84] 400H[97] and 594R,[92] we might be able to generate coherent hypersonic waves with frequencies greater than 150 GHz.

Another type of superlattice used by Martin, et al.[98] are the crystalline long-chain paraffinic solids which are composed of the n-paraffin by replacing a specific CH_2 group in the chain by a dipolar C=O group. They reported the generation of phonons at frequencies 28, 37, 58, 73, and 115 cm^{-1} [99] by direct absorption of far-infrared radiation in the long-chain molecular superlattice. They constructed a superlattice of this type with total thickness of 100 μ and periodicity of 40 Å. They estimated the photon-to-phonon power conversion efficiency which is an order of magnitude greater than the GaAs-GaP piezoelectric system (in our calculation) per superlattice layer.

Note that a superlattice which is composed of isotropic alternating thin films by vacuum deposition can only be used to generate longitudinal phonons by the mixing of two laser beams. No phonon can be generated by the first-order interaction because of inversion symmetry and no transverse phonons can be produced by two-laser mixing.

From our calculation and discussion, it appears that a superlattice that can be constructed by many different ways can be used as a practical device to generate coherent hypersonic waves at very high frequencies. In both cases we have calculated, the acoustic power generated under phase-matching conditions is proportional to the square

of the total number of unit cells in the superlattice. The generation of hypersonic waves at frequencies higher than 50 GHz with a power larger than 1 mW should be possible in a superlattice about 10 μ thick.

ACKNOWLEDGMENTS

I am grateful to my thesis advisor, Professor P. L. Richards, for his indefatigable guidance and enthusiastic support throughout the course of this work. I am also grateful for Professor Y. R. Shen for fruitful discussions and invaluable guidance during many phases of this work.

I would like to thank J. R. Morris for his detailed theoretical calculations for the picosecond-pulse experiment and for his cooperation on the experiment of mixing two dye lasers. My understanding of non-linear optics has benefited greatly from many discussions with him. Thanks are also due to many members in Professor Richards' group, from whom I learned much through daily discussions. Among them, I especially thank Dr. Richard Joyce, from whom I learned many techniques needed during my first year of research.

I would like to thank my wife, Nancy, for her understanding and sharing of the frustrations throughout this work. I thank Kathy Williams Hoffer for her typing of many manuscripts for the papers.

This work was performed under the auspices of the U. S. Atomic Energy Commission.

APPENDIX

A. Calculation of Fabry-Perot Interference Fringes

In this calculation, we mainly used the formulas obtained by Ulrich et al.[20] Consider a 2-dimensional square grid with separation g between wires of rectangular cross section with breadth 2a. If a Fabry-Perot interferometer (FPI) is composed of two identical paralle plane grids (or metal meshes) of this type with separation d, the power transmission $\tau(\lambda)$ for a normally incident plane wave of wavelength λ is

$$\tau(\lambda) = \left(1 + \frac{A}{T}\right)^{-2} \left(1 + \frac{4R}{(1 - R)^2} \sin^2\frac{2\delta}{2}\right)^{-1} \tag{A1}$$

where

$$\delta = 4\pi nd/\lambda - 2(\phi - \pi) \tag{A2}$$

and where $R^{1/2}e^{i\phi}$, A, and T are the amplitude reflection coefficient, the power absorption, and the power transmission of a single 2d grid respectively. There three parameters are related to one another through the following two equations

$$T = 1 - R = 4w^2g^2/\lambda^2 \tag{A3}$$

$$\tau_o = \left(1 + \frac{A}{T}\right)^{-2} \simeq 1 - \frac{\lambda^{3/2}}{6agw^2}\left(\frac{\sigma}{c}\right)^{1/2} \tag{A4}$$

where τ_o is the peak power transmission of a FPI and w is defined as

$$w = \ln\csc(\pi a/g) \tag{A5}$$

The finesse F is defined as

$$F \simeq \frac{\pi R^{1/2}}{1 - R} = \frac{\lambda^2\pi}{4w^2g^2}\ (1 - 4w^2g^2/\lambda^2)^{1/2} \simeq \lambda^2\ \frac{\pi}{4w^2g^2} \tag{A6}$$

In the above formula, the approximations are valid for $R \geqslant 0.6$ and $\lambda >> g$.

In the experiment, however, Ulrich et al. observed both τ_o and F were only 80% of values calculated from Eq. (A4) and Eq. (A6) due to deviations Δd in spacing caused by the uneveness and poor parallelism of the two grids.

In the picosecond laser experiments, we used the electroformed nickel metal-mashed FPI of 100 lines per inch with a = 0.00105 in. to measure a spectrum containing two narrow peaks--forward and backward phase-matched peaks respectively. The power tranmission took the form

$$\tau d = \iint \frac{I_f(v)\ dvd\theta}{1 + B_f \sin^2(\frac{2\pi v}{c}\ d\cdot\cos\theta)} + \iint \frac{I_b(v)\ dvd\theta}{1 + B_b \sin^2(\frac{2\pi v}{c}\ d\cos\theta)} \tag{A7}$$

where θ was angle between the incident far-infrared and the normal of FPI grids. The $I_f(v)$ and $I_b(v)$, which denoted the theoretically calculated forward and backward phase-matched spectra (shown in Fig. 6(b)) multiplied by the corresponding peak transmissivity of the FPI as expressed in Eq. (A4), had true Δv_f (Fullwidth half maximum) of 1.2 cm^{-1} and Δv_b of 0.6 cm^{-1} respectively. The linewidths were calculated using Eqs. (15) and (16). In our case, we assumed that τ_o and F had 80% values calculated from Eqs. (A4) and (A6). We obtained F = 2.9, B_f = 3.76 for v_f = 13.5 cm^{-1} and F = 16.8, B_b = 114.7 for v_b = 6.75 cm^{-1}. The numerators in Eq. (A7) are not sensitive function for v within their corresponding linewidths. Using the two-peak spectrum of Fig. 6(b), integrated with respect to v first and obtained the form

$$\tau_d = c_1 \int_0^{40°} \frac{d\theta}{1 + 3.76 \sin^2\left(\frac{2\pi v_f}{c} d\cos\theta\right)} + c_2 \int_0^{40°} \frac{d\theta}{1 + 114.7 \sin^2\left(\frac{2\pi v_b}{c} d\cos\theta\right)} \tag{A8}$$

where $c_1/c_2 = 1$.

In Eq. (A8), we assumed the far-infrared spreading angle of 40° and both B_f and B_b were independent of θ within this range. The result of this calculation is shown as the solid curve of Fig. 7. The theoretical calculation in Fig. 8 was obtained by using the same formula (Eq. (A8)) and $c_1/c_2 = 1.7$, $B_f = 7.16$, $B_b = 234$, $v_f = 11\ cm^{-1}$ and $v_b = 5.5\ cm^{-1}$.

B. The Dispersion of $\chi^{(2)}$

In the following, we will derive Eqs. (35) and (36) in a simple way. Our derivations will differ only a factor from the detailed rigid derivations which come from Henry et al.[42] Sussman,[43] and Shen.[67] The derivation of Eq. (37) can be found in Appendix 3 of Quantum Electronics by Yariv.[44] For simplicity, only single polariton mode will be treated while multi-polariton modes can be easily included by a summation. Tensor notations which complicate the derivations will be neglected.

a. Spontaneous Raman Scattering and Raman Susceptibility. Suppose a material has a vibration mode, or a polariton mode, or a magnon mode, then the linear susceptibility of that material can be expanded as a function of a normal mode

$$\chi = \chi_o^{(1)} + \left(\frac{\partial\chi(1)}{\partial Q}\right)_o Q \tag{A9}$$

where Q represents the specific mode mentioned. The energy density in the medium (or interacting Hamiltonian) has the following form when there is optical E field present inside the medium

$$U = -P\cdot E = -\chi E\cdot E = -\left[\chi_o^{(1)} + \left(\frac{\partial\chi^{(1)}}{\partial Q}\right)_o Q\right] EE \tag{A10}$$

$$= U^{(o)} + U^{(N)} = -\chi_o^{(1)}\ E\cdot E - \left(\frac{\partial\chi^{(1)}}{\partial Q}\right)_o QEE$$

The second term on the right hand side of Eq. (A10) is responsible for the Raman scatterings. The first term represents the linear interaction between the field and the medium. When a strong laser beam $E_p(w_p)$ shines on the medium, the normal mode $Q(w_v)$ can be excited due to the non-linear interaction which also produces a scattering light $E_s(w_s)$. The following equations describe this situation

$$\left(\nabla + \frac{w_p^2}{c^2}\varepsilon_p\right) E_p(w_p) = -\frac{4\pi}{c^2} w_p^2 \left(\frac{\partial\chi^{(1)}}{\partial Q}\right) E_s(w_s)\ Q(w_v) \tag{A11}$$

$$\left(\nabla^2 + \frac{w_s^2}{c^2}\varepsilon_s\right) E_s(w_s) = -\frac{4\pi}{c^2} w_s^2 \left(\frac{\partial\chi^{(1)}}{\partial Q}\right) E_p(w_p)\ Q^*(w_v) \tag{A12}$$

$$\left(w_T^2 - w_v^2 + i\Gamma w_v\right) Q = \left(\frac{\partial\chi^{(1)}}{\partial Q}\right) E_p(w_p)\ E_s^*(w_s) \tag{A13}$$

The right hand sides of Eq. (A11) and Eq. (A12) come from a general equation similar to Eq. (2) and using Eq. (A10)

$$P_i^{(N)} = -\frac{\partial U^{(N)}}{\partial E_i^*} = +\frac{\partial}{\partial E_i^*}\left[\left(\frac{\partial\chi}{\partial Q}\right) Q^* E_p E_s^* + c.c.\right] \tag{A14}$$

$$i = P \text{ or } S$$

The Eq. (A13) describes the normal mode motion with driving force coming from $-\partial U^{(N)}/\partial Q^*$. Substitute Eq. (A13) into Eq. (A12), we obtain

$$\left(\nabla^2 + \frac{w_s^2}{c^2}\varepsilon_s\right) E_s(w_s) = -\frac{4\pi}{c^2} w_s^2 \left|\frac{\partial\chi^{(1)}}{\partial Q}\right|^2 |E_p|^2 \frac{1}{D(w_v)^*} E_s \tag{A15}$$

where $D(w_v) = w_T^2 - w_v^2 + i\Gamma w_v$. The Raman susceptibility is defined as

$$\chi_R = \left|\frac{\partial\chi^{(1)}}{\partial Q}\right|^2 \frac{1}{D(w_v)^*} \tag{A16}$$

Furthermore, from Eq. (A14), the electric dipole $P_s^{(N)}$ radiates the scattered light $E_s(W_s)$ with power dP into a solid angle $d\Omega$. From Jackson's Electrodynamics, p. 273, we obtain

$$\frac{dp}{d\Omega} = \frac{c}{8\pi} n_s K_s^4 |p|^2 \sin^2\theta = \frac{c}{8\pi} n_s K_s^2 \left|\frac{\partial\chi^{(1)}}{\partial Q}\right|^2 |E_p|^2 \langle Q\rangle^2 \sin^2\theta \tag{A17}$$

at 90° scattering angle $\sin\theta = 1$. The Raman scattering differential corss-section is in the form

$$\left(\frac{d\sigma}{d\Omega}\right)_R = \frac{dp/d\Omega}{P_p} = \frac{n_s K_s^4}{n_p} \left|\frac{\partial\chi^{(1)}}{\partial Q}\right|^2 \langle Q\rangle^2 \tag{A18}$$

where $P_p = cn_p|E_p|^2/8\pi$ is used. From corresponding principle, the average enery of a normal mode takes the form

$$\langle Q\rangle^2 w_T^2 \simeq \frac{1}{2}\hbar w_T \tag{A19}$$

substitute Eqs. (A19) and (A18) into Eq. (A16), we obtain

$$\chi_R = \frac{2w_T}{\hbar D(w_v)^*} \frac{n_p}{n_s K_s^*} \left(\frac{d\sigma}{d\Omega}\right)_R \tag{A20}$$

b. Polarization Mode and Raman Susceptibility. Polariton mode is just a kind of normal mode which represents a combination of phonon-vibration and electric field inside the medium. The normal coordinate Q now is a linear combination of $V(w_v)$ and $E_3(w_v)$ where $V(w_v)$ is the lattice vibration and $E_3(w_v)$ is the associated far-infrared field. Hence, $\left(\frac{\partial\chi}{\partial Q}\right)$ in Section a has to be replaced by two constants. We get the the following formula

$$U^{(N)} = -d_E E_p E_s^* E_3^* - d_\theta e E_p E_s^* V^* - eVE_3^* + c.c. \tag{A21}$$

where $|e|$ is the charge of electron and the last term in Eq. (A21) denotes the polariton coupling. Deriving the equations for E_s, E_3 and V due to the non-linear driving forces caused by Eq. (A21), we get

$$\left(\nabla^2 + \frac{w_v^2}{c^2}\varepsilon_\infty\right) E_3 = -\frac{4\pi w_v^2}{c^2}\left[d_E E_p E_s^* + eV\right] \tag{A22}$$

$$\left(\nabla^2 + \frac{w_s^2}{c^2}\varepsilon_s\right) E_s = -\frac{4\pi w_s^2}{c^2}\left[d_E E_p E_3^* + e d_\theta E_p V^*\right] \tag{A23}$$

and

$$uD(w_v)\ V = eE_3 + e d_\theta E_p E_s^* \tag{A24}$$

where u is reduced mass of the lattice vibration.

In Eq. (A24), we can solve V and substitute it into Eq. (A22) and Eq. (A23) and we use the formula

$$\varepsilon_v = \varepsilon_\infty + \frac{Sw_T^2}{D(w_v)} = \varepsilon_\infty + \frac{4\pi e^2}{uD(w_v)} \tag{25}$$

where S is the oscillator strength of the polariton mode and is equal to $\frac{4\pi e^2}{uw_T^2}$ where w_T is the polariton mode frequency, we easily get

$$\left[\nabla^2 + \frac{w_v^2}{c^2}\varepsilon_v\right] E_3 = -\frac{4\pi w_v^2}{c^2}\left[d_E + \frac{1}{4}\frac{Sd_\theta w_T^2}{D(w_v)}\right] E_p E_s^* \tag{A26}$$

and

$$\left[\nabla^2 + \frac{w_s^2}{c^2}\varepsilon_s\right] E_s = -\frac{4\pi w_s^2}{c^2}\left[dE + \frac{1}{4\pi}\frac{Sd_\theta w_T^2}{D^*(w_v)}\right] E_p E_3^* - \frac{4\pi w_s^2}{c^2} \tag{A27}$$

$$\left[\frac{1}{4\pi}\frac{Sw_T^2|d_\theta|^2}{D(w_v)^*}\right] |E_p|^2 E_s$$

In the mixing experiment, we usually have the far-infrared equation as in Eq. (A26) with right hand side replaced by

$$-\frac{4\pi}{c^2} w_3^2 \frac{\chi^{(2)}}{2} E_1 E_2^* \quad .$$

Therefore, we obtain the Eq. (35) without the summation

$$\frac{1}{2}\chi^{(2)}(w_3) = d_E + \frac{1}{4\pi}\frac{Sw_T d_\theta}{w_T^2 - w_3^2 + i\Gamma w_3} \tag{A28}$$

If the depletion of the input beam is neglegible, Eqs. (A26) and (A27) are coupled together. Compared Eq. (A27) with Eq. (A15), the Raman susceptibility in this case is

$$\chi_R = \frac{1}{4\pi}\frac{Sw_T^2|d_\theta|^2}{D(w_v)^*} \tag{29}$$

Setting Eq. (A29) equal to Eq. (A20), we finally have the form

$$d_\theta = \pm \left[\frac{8\pi n_p c^4}{\hbar w_T S n_s w_s^4} \left(\frac{d\sigma}{d\Omega}\right)_R \right]^{1/2} \tag{A30}$$

Identifying Eq. (A30) with Eq. (36) term by term, we realize that a factor $\bar{n}_T + 1$, which can be obtained from a more detailed quantum mechanical description, is missing in the denominator of Eq. (A30). This factor $\bar{n}_T + 1$, differs negligibly from one in the usual cases.

C. Phonon Generation via Piezoelectric constants in a Superlattice

In this appendix, the first computer program PIEZO calculated the photon-to-phonon conversion efficiency in a GaAs: GaP superlattice of 100 unit cells. The input physical constants were

	$v(10^5$ cm/sec)	ρ(g/cm^3)	$e\left(10^{-8}\ \frac{esu}{dyne}\right)$	$T\left(10^{12}\ \frac{dyne}{cm^2}\right)$	ε	d(Å)
GaAs	2.80	5.31	-4.8	0.416	12.96	280
GaP	3.54	4.13	-3.0	0.518	10.24	354

The frequencies from first to tenth unklapp processes are shown on the abscissa of Fig. 20.

The second program POPIE calculated the effect on the conversion efficiency due to ±2% random errors in the periodicity of the superlattice. The input physical constants were the same as in the first program.

D. Phonon Generation via Electrostrictive Coupling in a Superlattice

The first computer program ELETO calculated the photon power generated with 1 watt/cm^2 input power for each laser beam in a KCl:CdS superlattice of 100 unit cells. The corresponding physical constants for this computation were

	$v(10^5 cm/sec)$	$\rho(g/cm^3)$	P	$T\left(10^{12} \frac{dyne}{cm^2}\right)$	n	d(Å)
KCl	4.20	1.98	0.124	0.398	1.50	420
CdS	4.50	4.825	0.066	0.850	2.43	450

The frequencies from first to tenth unklapp processes are shown on the abscissa of Fig. 21.

The second program POELE calculated the effect on the generated phonon power due to ±2% random errors in the periodicity of the superlattice. The input physical constants were the same as in the first program.

```
      PROGRAM PIEZO (INPUT, OUTPUT)
      DIMENSION W(10)
      COMMON E1,E2,T1,T2,A,B,D1,DI,D,Z1,Z2,BR,TBB,CC,TCC,DD,TDD,EPC,TKC,
     1GAMA, TGMA,DELTA,TDEL
C
C      THE FUNCTIONS IN THE FOLLOWING ARE THOSE CONTAINED IN (56) FOR F(X)
      DOWRF(X)=COSF(Z1*X)-EPC*COSF(Z1*D1+Z1*X)
      DOWIF(X)=SINF(Z1*X)+EPC*SINF(Z1*D1+Z1*X)
      UPRF(X)=COSF(A*X)-BR*COSF(A*D1+A*X)
      UPIF(X)=SINF(A*X)+BR*SINF(A*D1+A*X)
      DEN1F(X)=DOWRF(X)*DOWRF(X)+DOWIF(X)*DOWIF(X)
      TIONRF(X)=(UPRF(X)*DOWRF(X)+UPIF(X)*DOWIF(X))/DEN1F(X)
      TIONIF(X)=(UPIF(X)*DOWRF(X)-UPRF(X)*DOWIF(X))/DEN1F(X)
      DSRF(X)=(Z-U+(Y-V)*COSF(Z1*D1))*COSF(Z2*X)+(Y+V)*SINF(Z1*D1)
     1*SINF(Z2*X)
      DSIF(X)=(Z+U+(Y+V)*COSF(Z1*D1))*SINF(Z2*X)-(Y-V)*SINF(Z1*D1)
     1*COSF(Z2*X)
      USRF(X)=(CR1-DR1)*COSF(B*X)+CR2*COSF(B*X-A*D1)-DR2*COSF(B*X+A*D1)
      USIF(X)=(CR1+DR1)*SINF(B*X)+CR2*SINF(B*X-A*D1)+DR2*SINF(B*X+A*D1)
      DEN2F(X)=DSRF(X)*DSRF(X)+DSIF(X)*DSIF(X)
      SIONRF(X)=(DSRF(X)*USRF(X)+DSIF(X)*USIF(X))/DEN2F(X)
      SIONIF(X)=(DSRF(X)*USIF(X)-DSIF(X)*USRF(X))/DEN2F(X)
      UOPRF(X)=COSF(A*X)+BR*COSF(A*D1+A*X)
      UOPIF(X)=SINF(A*X)-BR*SINF(A*D1+A*X)
      UDRF(X)=(CR1+DR1)*COSF(B*X)+CR2*COSF(B*X-A*D1)+DR2*COSF(B*X+A*D1)
      UDIF(X)=(CR1-DR1)*SINF(B*X)+CR2*SINF(B*X-A*D1)+DR2*COSF(B*X+A*D1)
      DIS1RF(X)=(UOPRF(X)*DOWRF(X)+UOPIF(X)*DOWIF(X))/DEN1F(X)
      DIS1IF(X)=(UOPIF(X)*DOWRF(X)-UOPRF(X)*DOWIF(X))/DEN1F(X)
      DIS2RF(X)=(UDRF(X)*DSRF(X)+UDIF(X)*DSIF(X))/DEN2F(X)
      DIS2IF(X)=(UDIF(X)*DSRF(X)-UDRF(X)*DSIF(X))/DEN2F(X)
C
C      THE PHYSICAL CONSTANTS OF GAAS AND GAP
```

```
      READ 30, V1, V2, P1, P2, E1, E2, T1, T2, DE1, DE2
   30 FORMAT (10F8.4)
C
C      THE FREQUENCIES FROM FIRST TO TENTH UMKLAPP PROCESSES
      READ 31, W(1),W(2),W(3),W(4),W(5),W(6),W(7),W(8),W(9),W(10)
   31 FORMAT (10F8.4)
C
C      THE CONSTANTS RELATED TO SOUND WAVE IN (60)
      PE2=P2*V2
      PE1=P1*V1
      D1=0.280
      D2=0.354
      D=D1+D2
      RATIO=(E2*DE2*V2*T1)/(T2*E1*DE1*V1)
      L=1
  100 Z1=W(L)/V1
      Z2=W(L)/V2
      IF (L-2) 101, 102, 103
  101 GO TO 115
  102 GO TO 116
  103 IF (L-4) 104, 105, 106
  104 GO TO 115
  105 GO TO 116
  106 IF (L-6) 107, 108, 109
  107 GO TO 115
  108 GO TO 116
  109 IF (L-8) 110, 111, 112
  110 GO TO 115
  111 GO TO 116
  112 IF (L-10) 113, 114, 114
  113 GO TO 115
  114 GO TO 116
```

```
  115 SS=-1.0
      GO TO 117
  116 SS=1.0
  117 EPC=SS*(PE2+PE1)/(PE2-PE1)
      Z=(PE2+PE1)/(2.0*PE2)
      Y=Z*SS
      U=(PE2-PE1)/(2.0*PE2)
      V=((PE2+PE1)**2*SS)/((PE2-PE1)*2.0*PE2)
      TKC=-Z1*D1
      PRINT 118, EPC, TKC, Z, Y, U, V
  118 FO-MAT (7H SOUND /(6E15.4))
C
C       THE CONSTANTS RELATED TO LIGHT WAVE IN (58)
      A=DE1*W(L)/3.0E+05
      B=DE2*W(L)/3.0E+05
      GOST=COSF(A*D1)*COSF(B*D2)-(DE1*DE1+DE2*DE2)*SINF(A*D1)*SINF(B*D2)
     1/(2.0*DE1*DE2)
      ROT=SQRTF(1.0-GOST*GOST)
      XX=ATANF(ROT/GOST)
      S=SINF(0.5*(A*D1+B*D2-XX))/SINF(0.5*(A*D1-B*D2+XX))
      BR=S*(DE1+DE2)/(DE2-DE1)
      BB=BR*BR
      CR1=(DE2+DE1)/(2.0*DE2)
      CR2=CR1*S
      DR1=(DE2-DE1)/(2.0*DE2)
      DR2=(DE2+DE1)**2*S/(2.0*DE2*(DE2-DE1))
      TBB=-A*D1
      BOUND=4.0/((1.0+DE1)**2+(1.0-DE1)**2*BB)
      PRINT 120, BR, TBB, CR1, CR2, DR1, DR2
  120 FORMAT (7H LIGHT /(6E15.4))
C
C       THE FOLLOWING IS THE CALCULATION FOR F1 IN (57)
```

```
130 SUM4=0.0
    SUM2=0.0
    TUM4=0.0
    TUM2=0.0
    PUM4=0.0
    PUM2=0.0
    RUM4=0.0
    RUM2=0.0
    N=1000
    FN=N
    DX=D1/FN
    EX=D2/FN
    I=1
132 FI=I
    X=-D1+FI*DX
    R=FI*EX+0.0
    SUM4=SUM4+TIONRF(X)
    SUM2=SUM2+TIONRF(X+DX)
    TUM4=TUM4+TIONIF(X)
    TUM2=TUM2+TIONIF(X+DX)
    PUM4=PUM4+SIONRF(R)
    PUM2=PUM2+SIONRF(R+EX)
    RUM4=RUM4+SIONIF(R)
    RUM2=RUM2+SIONIF(R+EX)
    IF (I-N+3) 134, 136, 136
134 I=I+2
    GO TO 132
136 CELL1R=DX*(4.0*SUM4+2.0*SUM2+TIONRF(0.0)+TIONRF(-D1)+4.0*TIONRF(
   1-DX))/(3.0E+05)
    CELL1I=DX*(4.0*TUM4+2.0*TUM2+TIONIF(0.0)+TIONIF(-D1)+4.0*TIONIF(
   1-DX))/(3.0E+05)
    CELL2R=EX*(4.0*PUM4+2.0*PUM2+SIONRF(0.0)+SIONRF(D2)+4.0*SIONRF(D2-
```

```
     1EX))/(3.0E+05)
      CELL2I=EX*(4.0*RUM4+2.0*RUM2+SIONIF(0.0)+SIONIF(D2)+4.0*SIONIF(D2-
     1EX))/(3.0E+05)
      CLLR=(CELL1R+RATIO*CELL2R)*E1*V1*DE1/(2.0*T1*3.0E+05)
      CLLI=(CELL1I+RATIO*CELL2I)*E1*V1*DE1/(2.0*T1)/3.0E+05
      SCLL=CLLR**2+CLLI**2
      PRINT 150, CELL1R, CELL1I, CELL2R, CELL2I, CLLR, CLLI, SCLL
  150 FORMAT (14H INTERGATION /(7E14.4))
C
C      CALCULATE F2 IN (57)
      CAN1=DIS1IF(0.0)/PE1+DIS2IF(0.0)/PE2
      CAN2=DIS1IF(-D1)/PE1+DIS2IF(D2)/PE2
      DAN1=DIS1RF(0.0)/PE1+DIS2RF(0.0)/PE2
      DAN2=DIS1RF(-D1)/PE1+DIS2RF(D2)/PE2
      PRINT 151, CAN1, CAN2, DAN1, DAN2
  151 FORMAT (6H PARE /(4E20.5))
      HSIN=(E2-E1)/(4.0E+03*W(L))
      CONR=HSIN*(CAN1-CAN2)
      CONI=HSIN*(DAN2-DAN1)
      CONS=CONR*CONR+CONI*CONI
      PRINT 152, CONR, CONI, CONS
  152 FORMAT (8H DISCON /(3E20.4))
C
C      CALCULATE THE SOUND POWER
      GOAL=(CLLR+CONR)**2+(CLLI+CONI)**2
      BOR=(Z+U)*COSF(Z2*D2)+Y+V
      SBR=BOR*BOR
      TOR=Z2*Z2*SBR*T2*V2*1.0E+05*12.5664*BOUND/6.0
      AUMP=SCLL*TOR
      DISP=CONS*TOR
      POWER=GOAL*TOR
      PR+NT 155, AUMP, DISP, POWER
```

```
155 FORMAT (7H POWER /(3E25.4))
    IF (L-10) 160, 162, 162
160 L=L+1
    GO TO 100
162 CALL EXIT
    END
```

```
      PROGRAM POPIE (INPUT, OUTPUT)
      DIMENSION W(10)
      COMMON E1,E2,T1,T2,A,B,D1,D2,D,Z1,Z2,BR,TBB,CC,TCC,DD,
     1GAMA, TGMA,DELTA,TDEL
C
C      THE FUNCTIONS IN THE FOLLOWING ARE THOSE CONTAINED IN (56) FOR F(X)
      DOWRF(X)=COSF(Z1*X)-EPC*COSF(Z1*D1+Z1*X)
      DOWIF(X)=SINF(Z1*X)+EPC*SINF(Z1*D1+Z1*X)
      UPRF(X)=COSF(A*X)-BR*COSF(A*D1+A*X)
      UPIF(X)=SINF(A*X)+BR*SINF(A*D1+A*X)
      DEN1F(X)=DOWRF(X)*DOWRF(X)+DOWIF(X)*DOWIF(X)
      TIONRF(X)=(UPRF(X)*DOWRF(X)+UPIF(X)*DOWIF(X))/DEN1F(X)
      TIONIF(X)=(UPIF(X)*DOWRF(X)-UPRF(X)*DOWIF(X))/DEN1F(X)
      DSRF(X)=(Z-U+(Y-V)*COSF(Z1*D1))*COSF(Z2*X)+(Y+V)*SINF(Z1*D1)
     1*SINF(Z2*X)
      DSIF(X)=(Z+U+(Y+V)*COSF(Z1*D1))*SINF(Z2*X)-(Y-V)*SINF(Z1*D1)
     1*COSF(Z2*X)
      USRF(X)=(CR1-DR1)*COSF(B*X)+CR2*COSF(B*X-A*D1)-DR2*COSF(B*X+A*D1)
      USIF(X)=(CR1+DR1)*SINF(B*X)+CR2*SINF(B*X-A*D1)+DR2*SINF(B*X+A*D1)
      DEN2F(X)=DSRF(X)*DSRF(X)+DSIF(X)*DSIF(X)
      SIONRF(X)=(DSRF(X)*USRF(X)+DSIF(X)*USIF(X))/DEN2F(X)
      SIONIF(X)=(DSRF(X)*USIF(X)-DSIF(X)*USRF(X))/DEN2F(X)
      UOPRF(X)=COSF(A*X)+BR*COSF(A*D1+A*X)
      UOPIF(X)=SINF(A*X)-BR*SINF(A*D1+A*X)
      UDRF(X)=(CR1+DR1)*COSF(B*X)+CR2*COSF(B*X-A*D1)+DR2*COSF(B*X+A*D1)
      UDIF(X)=(CR1-DR1)*SINF(B*X)+CR2*SINF(B*X-A*D1)+DR2*COSF(B*X+A*D1)
      DIS1RF(X)=(UOPRF(X)*DOWRF(X)+UOPIF(X)*DOWIF(X))/DEN1F(X)
      DIS1IF(X)=(UOPIF(X)*DOWRF(X)-UOPRF(X)*DOWIF(X))/DEN1F(X)
      DIS2RF(X)=(UDRF(X)*DSRF(X)+UDIF(X)*DSIF(X))/DEN2F(X)
      DIS2IF(X)=(UDIF(X)*DSRF(X)-UDRF(X)*DSIF(X))/DEN2F(X)
      BR1RF(X)=DIS1IF(X)/PE1
      BR2RF(X)=DIS2IF(X)/PE2
```

```
      BR1IF(X)=DIS1RF(X)/PE1
      BR2IF(X)=DIS2RF(X)/PE2
      DAMRF(X)=BR1RF(X)+BR2RF(X)
      DAMIF(X)=BR1IF(X)+BR2IF(X)
C
C      PHYSICAL CONSTANTS OF GAAS AND GAP
      READ 30, V1, V2, P1, P2, E1, E2, T1, T2, DE1, DE2
   30 FORMAT (10F8.4)
C
C      THE FREQUENCIES FROM FIRST TO TENTH UMKLAPP PROCESSES
      READ 31, W(1),W(2),W(3),W(4),W(5),W(6),W(7),W(8),W(9),W(10)
   31 FORMAT (10F8.4)
C
C      THE CONSTANTS RELATED TO SOUND WAVE IN (60)
      PE2=P2*V2
      PE1=P1*V1
      D1=0.280
      D2=0.354
      D=D1+D2
      RATIO=(E2*DE2*V2*T1)/(T2*E1*DE1*V1)
      L=1
  100 Z1=W(L)/V1
      Z2=W(L)/V2
      IF (L-2) 101, 102, 103
  101 GO TO 115
  102 GO TO 116
  103 IF (L-4) 104, 105, 106
  104 GO TO 115
  105 GO TO 116
  106 IF (L-6) 107, 108, 109
  107 GO TO 115
  108 GO TO 116
```

```
109 IF (L-8) 110, 111, 112
110 GO TO 115
111 GO TO 116
112 IF (L-10) 113, 114, 114
113 GO TO 115
114 GO TO 116
115 SS=-1.0
    GO TO 117
116 SS=1.0
117 EPC=SS*(PE2+PE1)/(PE2-PE1)
    Z=(PE2+PE1)/(2.0*PE2)
    Y=Z*SS
    U=(PE2-PE1)/(2.0*PE2)
    V=((PE2+PE1)**2*SS)/((PE2-PE1)*2.0*PE2)
    TKC=-Z1*D1
    PRINT 118, EPC, TKC, Z, Y, U, V
118 FORMAT (7H SOUND /(6E15.4))
C
C     THE CONSTANTS RELATED TO LIGHT WAVE IN (58)
    A=DE1*W(L)/3.0E+05
    B=DE2*W(L)/3.0E+05
    GOST=COSF(A*D1)*COSF(B*D2)-(DE1*DE1+DE2*DE2)*SINF(A*D1)*SINF(B*D2)
   1/(2.0*DE1*DE2)
    ROT=SQRTF(1.0-GOST*GOST)
    XX=ATANF(ROT/GOST)
    S=SINF(0.5*(A*D1+B*D2-XX))/SINF(0.5*(A*D1-B*D2+XX))
    BR=S*(DE1+DE2)/(DE2-DE1)
    BB=BR*BR
    CR1=(DE2+DE1)/(2.0*DE2)
    CR2=CR1*S
    DR1=(DE2-DE1)/(2.0*DE2)
    DR2=(DE2+DE1)**2*S/(2.0*DE2*(DE2-DE1))
```

```
      TBB=-A*D1
      BOUND=4.0/((1.0+DE1)**2+(1.0-DE1)**2*BB)
      PRINT 120, BR, TBB, CR1, CR2, DR1, DR2
  120 FORMAT (7H LIGHT /(6E15.4))
C
C      THE FOLLOWING IS THE CALCULATION FOR F1 IN (57)
      KI=20
      HI=KI
  130 SUM4=0.0
      SUM2=0.0
      TUM4=0.0
      TUM2=0.0
      PUM4=0.0
      PUM2=0.0
      RUM4=0.0
      RUM2=0.0
      N=1000
      FN=N
      DX=D1/FN
      EX=D2/FN
      I=1
  132 FI=I
      X=-D1+FI*DX
      R=0.0+FI*EX
      SUM4=SUM4+TIONRF(X)
      SUM2=SUM2+TIONRF(X+DX)
      TUM4=TUM4+TIONIF(X)
      TUM2=TUM2+TIONIF(X+DX)
      PUM4=PUM4+SIONRF(R)
      PUM2=PUM2+SIONRF(R+EX)
      RUM4=RUM4+SIONIF(R)
      RUM2=RUM2+SIONIF(R+EX)
```

```
      IF (I-N+KI+3) 134, 136, 136
  134 I=I+2
      GO TO 132
  136 CELL1R=DX*(4.0*SUM4+2.0*SUM2+TIONRF(-D1)+TIONRF(-HI*DX)+
     14.0*TIONRF(-(HI-1.0)*DX))/3.0E+05
      CELL1I=DX*(4.0*TUM4+2.0*TUM2+TIONIF(-D1)+TIONIF(-HI*DX)+
     14.0*TIONIF(-(HI-1.0)*DX))/3.0E+05
      CELL2R=EX*(4.0*PUM4+2.0*PUM2+SIONRF(0.0)+SIONRF(D2-HI*EX)+
     14.0*SIONRF(D2-(HI-1.0)*EX))/3.0E+05
      CELL2I=EX*(4.0*RUM4+2.0*RUM2+SIONIF(0.0)+SIONIF(D2-HI*EX)+
     14.0*SIONIF(D2-(HI-1.0)*EX))/3.0E+05
C
C      THE VARIATION OF F1 DUE TO 2 PER CENT ERRORS IN PERIODICITY
      TY1=-D1*HI/FN
      TY2=D2*(FN-HI)/FN
      PX=DX/2.0
      RX=EX/2.0
      PINR=0.0
      PING=0.0
      RINR=0.0
      RING=0.0
      VARI=2.0*HI+1.0
      NI=1
  140 PI=NI
      ARG=TY1+PI*PX*2.0
      BRG=TY2+PI*RX*2.0
      PINR=(PINR+PX*(TIONRF(ARG-2.0*PX)+4.0*TIONRF(ARG-PX)+TIONRF(ARG))
     1/3.0)*(VARI-PI)/VARI
      PING=(PING+PX*(TIONIF(ARG-2.0*PX)+4.0*TIONIF(ARG-PX)+TIONIF(ARG))
     1/3.0)*(VARI-PI)/VARI
      RINR=(RINR+RX*(SIONRF(BRG-2.0*RX)+4.0*SIONRF(BRG-RX)+SIONRF(BRG))
     1/3.0)*(VARI-PI)/VARI
```

```
     1/3.0)*(VARI-PI)/VARI
      RING=(RING+RX*(SIONIF(BRG-2.0*RX)+4.0*SIONIF(BRG-RX)+SIONIF(BRG))
     1/3.0)*(VARI-PI)/VARI
      IF (NI-2*KI) 142, 144, 144
  142 NI=NI+1
      GO TO 140
  144 PC1R=CELL1R+PINR
      PC1I=CELL1I+PING
      PC2R=CELL2R+RINR
      PC2I=CELL2I+RING
      PCR=PC1R+PC2R
      PCI=PC1I+PC2I
      PSC=PCR*PCR+PCI*PCI
      PRINT 146, PC1R, PC1I, PC2R, PC2I, PCR, PCI, PSC
  146 FORMAT (9H PINTEG /(7E14.4))
C
C      THE VARIATION OF F2 IN (57) DUE TO 2 PER CENT ERRORS IN PERIODICITY
      AUM4=0.0
      AUM2=0.0
      BUM4=0.0
      BUM2=0.0
      CUM4=0.0
      CUM2=0.0
      DUM4=0.0
      DUM2=0.0
      EUM4=0.0
      EUM2=0.0
      GUM4=0.0
      GUM2=0.0
      TTX=D1/1000.0
      DDT=D2/1000.0
      MI=1
```

```
147 GI=MI
    RON=(-HI+GI)*TTX
    RIC=(-1000.0-HI)*TTX+GI*TTX
    ROG=(1000.0-HI+GI)*DDT
    AUM4=AUM4+DAMRF(RON)
    AUM2=AUM2+DAMRF(RON+TTX)
    BUM4=BUM4+DAMIF(RON)
    BUM2=BUM2+DAMIF(RON+TTX)
    CUM4=CUM4+BR1RF(RIC)
    CUM2=CUM2+BR1RF(RIC+TTX)
    DUM4=DUM4+BR1IF(RIC)
    DUM2=DUM2+BR1IF(RIC+TTX)
    EUM4=EUM4+BR2RF(ROG)
    EUM2=EUM2+BR2RF(ROG+DDT)
    GUM4=GUM4+BR2IF(ROG)
    GUM2=GUM2+BR2IF(ROG+DDT)
    IF (MI-2*KI+3) 148, 149, 149
148 MI=MI+2
    GO TO 147
149 TAUR=(4.0*AUM4+2.0*AUM2+DAMRF(-HI*TTX)+DAMRF(HI*TTX)
   1+4.0*DAMRF((HI-1.0)*TTX))/6.0/HI
    TAUI=(4.0*BUM4+2.0*BUM2+DAMIF(-HI*TTX)+DAMIF(HI*TTX)
   1+4.0*DAMIF((HI-1.0)*TTX))/6.0/HI
    SHER=(4.0*CUM4+2.0*CUM2+BR1RF(-D1-HI*TTX)+BR1RF(-D1+HI*TTX)
   1+4.0*BR1RF(-D1+(HI-1.0)*TTX))/6.0/HI
    SHEI=(4.0*DUM4+2.0*DUM2+BR1IF(-D1-HI*TTX)+BR1IF(-D1+HI*TTX)
   1+4.0*BR1IF(-D1+(HI-1.0)*TTX))/6.0/HI
    CHER=(4.0*EUM4+2.0*EUM2+BR2RF(D2-HI*DDT)+BR2RF(D2+HI*DDT)
   1+4.0*BR2RF(D2+(HI-1.0)*DDT))/6.0/HI
    CHEI=(4.0*GUM4+2.0*GUM2+BR2IF(D2-HI*DDT)+BR2IF(D2+HI*DDT)
   1+4.0*BR2IF(D2+(HI-1.0)*DDT))/6.0/HI
    HSIN=(DE1**4*C1-DE2**4*C2)/(4.0*W(L)*1.0E+04)
```

```
      CONR=HSIN*(TAUR-SHER-CHER)
      CONI=-HSIN*(TAUI-SHEI-CHEI)
      CONS=CONR*CONR+CONI*CONI
      PRINT 152, CONR, CONI, CONS
  152 FORMAT (8H DISCON /(3E20.4))
C
C      CALCULATE THE SOUND POWER
      GOAL=(PCR+CONR)**2+(PCI+CONI)**2
      BOR=(Z+U)*COSF(Z2*D2)+Y+V
      SBR=BOR*BOR
      TOR=Z2*Z2*SBR*T2*V2*1.0E+05*12.5664*BOUND/6.0
      AUMP=PSC*TOR
      DISP=CONS*TOR
      POWER=GOAL*TOR
      PRINT 155, AUMP, DISP, POWER
  155 FORMAT (7H POWER /(3E25.4))
      IF (L-10) 160, 162, 162
  160 L=L+1
      GO TO 100
  162 CALL EXIT
      END
```

```
      PROGRAM ELETO (INPUT, OUTPUT)
      DIMENSION W(10)
C
C      THE FUNCTIONS IN THE FOLLOWING ARE THOSE CONTAINED IN (56) FOR F(X)
      DOWIF(X)=SINF(Z1*X)+EPC*SINF(Z1*D1+Z1*X)
      DOWRF(X)=COSF(Z1*X)-EPC*COSF(Z1*D1+Z1*X)
      DEN1F(X)=1.0+EPC*EPC-2.0*EPC*COSF(Z1*D1+2.0*Z1*X)
      DSRF(X)=(Z-U+(Y-V)*COSF(Z1*D1))*COSF(Z2*X)+(Y+V)*SINF(Z1*D1)
     1*SINF(Z2*X)
      DSIF(X)=(Z+U+(Y+V)*COSF(Z1*D1))*SINF(Z2*X)-(Y-V)*SINF(Z1*D1)
     1*COSF(Z2*X)
      DEN2F(X)=DSRF(X)*DSRF(X)+DSIF(X)*DSIF(X)
      TIONRF(X)=(AT1*DOWRF(X)+AT2*(REAB*SINF(2.0*A*X)+RIAB*COSF(2.0*A*X)
     1)*DOWIF(X))/DEN1F(X)
      TIONIF(X)=(-AT1*DOWIF(X)+AT2*(REAB*SINF(2.0*A*X)+RIAB*COSF(2.0*A*X
     1))*DOWRF(X))/DEN1F(X)
      SIONRF(X)=(CT1*DSRF(X)+CT2*(RECD*SINF(2.0*B*X)+RICD*COSF(2.0*B*X))
     1*DSIF(X))/DEN2F(X)
      SIONIF(X)=(-CT1*DSIF(X)+CT2*(RECD*SINF(2.0*B*X)+RICD*COSF(2.0*B*X)
     1)*DSRF(X))/DEN2F(X)
      R11F(X)=1.0+BB+2.0*(REAB*COSF(2.0*A*X)-RIAB*SINF(2.0*A*X))
      R22F(X)=CC+DD+2.0*(RECD*COSF(2.0*B*X)-RICD*SINF(2.0*B*X))
      BR1RF(X)=R11F(X)*DOWIF(X)/(PE1*DEN1F(X))
      BR2RF(X)=R22F(X)*DSIF(X)/(PE2*DEN2F(X))
      BR1IF(X)=R11F(X)*DOWRF(X)/(PE1*DEN1F(X))
      BR2IF(X)=R22F(X)*DSRF(X)/(PE2*DEN2F(X))
C
C      PHYSICAL CONSTANTS FOR KCL AND CDS
      READ 11, DE1, DE2, P1, P2, V1, V2, C1, C2, T1, T2
   11 FORMAT (10F7.4)
C
C      THE FREQUENCIES FROM FIRST TO TENTH UMKLAPP PROCESSES
```

```
      READ 12, W(1),W(2),W(3),W(4),W(5),W(6),W(7),W(8),W(9),W(10)
   12 FORMAT (10F8.4)
C
C      FINDING THE CONSTANTS FOR LIGHT WAVES
      A=0.144*DE1*6.2832
      B=0.144*DE2*6.2832
      D1=0.420
      D2=0.450
      D=D1+D2
      Q1=C1/T1
      Q2=C2/T2
     1/(2.0*DE1*DE2)
      GOST=COSF(A*D1)*COSF(B*D2)-(DE1*DE1+DE2*DE2)*SINF(A*D1)*SINF(B*D2)
      ROT=SQRTF(1.0-GOST*GOST)
      XX=3.1416+ATANF(ROT/GOST)
      S=SINF(0.5*(A*D1+B*D2-XX))/SINF(0.5*(A*D1-B*D2+XX))
      BR=(DE1+DE2)*S/(DE2-DE1)
      BB=(DE1+DE2)**2*S*S/(DE2-DE1)/(DE2-DE1)
      REAB=(DE2+DE1)*S*COSF(A*D1)/(DE2-DE1)
      RIAB=(DE2+DE1)*S*SINF(A*D1)/(DE2-DE1)
      CC=(DE2+DE1)**2*(1.0+S*S+2.0*S*COSF(A*D1))/(4.0*DE2*DE2)
      DD=((DE2-DE1)**2+(DE2+DE1)**4*S*S/(DE2-DE1)**2+2.0*(DE2+DE1)**2*
     1COSF(A*D1)*S)/(4.0*DE2*DE2)
      TD=(DE2+DE1)/(4.0*DE2*DE2)
      SD=(DE2+DE1)**2/(DE2-DE1)
      RECD=TD*(DE2-DE1+SD*S*S+(SD+DE2-DE1)*S*COSF(A*D1))
      RICD=-TD*(DE2-DE1-SD)*S*SINF(A*D1)
      BOUND=4.0/((1.0+DE1)**2+(1.0-DE1)**2*BB)
      PRINT 13, BB, CC, DD, REAB, RIAB, RECD, RICD
   13 FORMAT (7H LIGHT /(7E16.5))
C
C      THE CONSTANTS RELATED TO SOUND WAVE IN (60)
```

```
      PE2=P2*V2
      PE1=P1*V1
      L=1
  100 Z1=W(L)/V1
      Z2=W(L)/V2
      SS=-1.0
  105 EPC=SS*(PE2+PE1)/(PE2-PE1)
      Z=(PE2+PE1)/(2.0*PE2)
      Y=Z*SS
      U=(PE2-PE1)/(2.0*PE2)
      V=((PE2+PE1)**2*SS)/((PE2-PE1)*2.0*PE2)
        TKC=-Z1*D1
      PRINT 110, EPC, TKC, Z, Y, U, V
  110 FORMAT (7H SOUND /(6E15.4))
      GO TO 129
  112 Z1=W(L)/V1
      Z2=W(L)/V2
      SS=1.0
      EPC=SS*(PE2+PE1)/(PE2-PE1)
      Z=(PE2+PE1)/(2.0*PE2)
      Y=Z*SS
      U=(PE2-PE1)/(2.0*PE2)
      V=((PE2+PE1)**2*SS)/((PE2-PE1)*2.0*PE2)
      TKC=-Z1*D1
      PRINT 114, EPC, TKC, Z, Y, U, V
  114 FORMAT (7H SOUND /(6E15.4))
C
C      THE FOLLOWING IS THE CALCULATION FOR F1 IN (57)
  129 AT1=DE1**5*Q1*W(L)*(1.0-BB)/(6.0E+05*Z1)
      AT2=2.0*DE1**4*Q1*A/Z1
      CT1=DE2**5*Q2*W(L)*(CC-DD)/(6.0E+05*Z2)
      CT2=2.0*DE2**4*Q2*B/Z2
```

```
130 SUM4=0.0
    SUM2=0.0
    TUM4=0.0
    TUM2=0.0
    PUM4=0.0
    PUM2=0.0
    RUM4=0.0
    RUM2=0.0
    N=1000
    FN=N
    DX=D1/FN
    EX=D2/FN
    I=1
132 FI=I
    X=-D1+FI*DX
    R=0.0+FI*EX
    SUM4=SUM4+TIONRF(X)
    SUM2=SUM2+TIONRF(X+DX)
    TUM4=TUM4+TIONIF(X)
    TUM2=TUM2+TIONIF(X+DX)
    PUM4=PUM4+SIONRF(R)
    PUM2=PUM2+SIONRF(R+EX)
    RUM4=RUM4+SIONIF(R)
    RUM2=RUM2+SIONIF(R+EX)
    IF (I-N+3) 134, 136, 136
134 I=I+2
    GO TO 132
136 CELL1R=DX*(4.0*SUM4+2.0*SUM2+TIONRF(0.0)+TIONRF(-D1)+4.0*TIONRF(
   1-DX))/(3.0E+05)
    CELL1I=DX*(4.0*TUM4+2.0*TUM2+TIONIF(0.0)+TIONIF(-D1)+4.0*TIONIF(
   1-DX))/(3.0E+05)
    CELL2R=EX*(4.0*PUM4+2.0*PUM2+SIONRF(0.0)+SIONRF(D2)+4.0*SIONRF(D2-
```

```
     1EX))/(3.0E+05)
      CELL2I=EX*(4.0*RUM4+2.0*RUM2+SIONIF(0.0)+SIONIF(D2)+4.0*SIONIF(D2-
     1EX))/(3.0E+05)
      CLLR=(CELL1R+CELL2R)
      CLLI=(CELL1I+CELL2I)
      SCLL=CLLR**2+CLLI**2
      PRINT 150, CELL1R, CELL1I, CELL2R, CELL2I, CLLR, CLLI, SCLL
  150 FORMAT (14H INTERGATION /(7E14.4))
C
C      CALCULATE F2 IN (57)
      CAN1=BR1RF(0.0)+BR2RF(0.0)
      CAN2=BR1RF(-D1)+BR2RF(D2)
      DAN1=BR1IF(0.0)+BR2IF(0.0)
      DAN2=BR1IF(-D1)+BR2IF(D2)
      PRINT 151, CAN1, CAN2, DAN1, DAN2
  151 FORMAT (6H PARE /(4E20.4))
      HSIN=(DE1**4*C1-DE2**4*C2)/(4.0*W(L)*1.0E+04)
      CONR=HSIN*(BR1RF(0.0)+BR2RF(0.0)-BR1RF(-D1)-BR2RF(D2))
      CONI=HSIN*(BR1IF(0.0)+BR2IF(0.0)-BR1IF(-D1)-BR2IF(D2))
      SCON=CONR*CONR+CONI*CONI
      PRINT 152, CONR, CONI, SCON
  152 FORMAT (8H DISCON /(3E20.4))
C
C      CALCULATE THE SOUND POWER
      SAMP=(CONR+CLLR)**2+(CONI+CLLI)**2
      PRINT 153, SAMP
  153 FORMAT (6H SAMP ,1E20.5)
      BOR=V2*T2*Z2*Z2*BOUND*BOUND/(72.0*1.0E+05)
      TOR=BOR*3.2415
      AUM=TOR*SCLL
      DIS=TOR*SCON
      POWER=TOR*SAMP
```

```
      PRINT 154, AUM, DIS, POWER
  154 FORMAT (7H POWER /(3E30.4))
      IF (L-10) 160, 180, 180
  160 L=L+1
      GO TO 163
  163 IF (L-2) 164, 164, 165
  164 GO TO 112
  165 IF (L-4) 166, 167, 168
  166 GO TO 100
  167 GO TO 112
  168 IF (L-6) 169, 170, 171
  169 GO TO 100
  170 GO TO 112
  171 IF (L-8) 172, 173, 174
  172 GO TO 100
  173 GO TO 112
  174 IF (L-10) 175, 176, 180
  175 GO TO 100
  176 GO TO 112
  180 CALL EXIT
      END
```

```
      PROGRAM POELE (INPUT, OUTPUT)
      DIMENSION W(10)
C
C      THE FUNCTIONS IN THE FOLLOWING ARE THOSE CONTAINED IN (56) FOR F(X)
      DOWIF(X)=SINF(Z1*X)+EPC*SINF(Z1*D1+Z1*X)
      DOWRF(X)=COSF(Z1*X)-EPC*COSF(Z1*D1+Z1*X)
      DEN1F(X)=1.0+EPC*EPC-2.0*EPC*COSF(Z1*D1+2.0*Z1*X)
      DSRF(X)=(Z-U+(Y-V)*COSF(Z1*D1))*COSF(Z2*X)+(Y+V)*SINF(Z1*D1)
     1*SINF(Z2*X)
      DSIF(X)=(Z+U+(Y+V)*COSF(Z1*D1))*SINF(Z2*X)-(Y-V)*SINF(Z1*D1)
     1*COSF(Z2*X)
      DEN2F(X)=DSRF(X)*DSRF(X)+DSIF(X)*DSIF(X)
      TIONRF(X)=(AT1*DOWRF(X)+AT2*(REAB*SINF(2.0*A*X)+RIAB*COSF(2.0*A*X)
     1)*DOWIF(X))/DEN1F(X)
      TIONIF(X)=(-AT1*DOWIF(X)+AT2*(REAB*SINF(2.0*A*X)+RIAB*COSF(2.0*A*X
     1))*DOWRF(X))/DEN1F(X)
      SIONRF(X)=(CT1*DSRF(X)+CT2*(RECD*SINF(2.0*B*X)+RICD*COSF(2.0*B*X))
     1*DSIF(X))/DEN2F(X)
      SIONIF(X)=(-CT1*DSIF(X)+CT2*(RECD*SINF(2.0*B*X)+RICD*COSF(2.0*B*X)
     1)*DSRF(X))/DEN2F(X)
      R11F(X)=1.0+BB+2.0*(REAB*COSF(2.0*A*X)-RIAB*SINF(2.0*A*X))
      R22F(X)=CC+DD+2.0*(RECD*COSF(2.0*B*X)-RICD*SINF(2.0*B*X))
      BR1RF(X)=R11F(X)*DOWIF(X)/(PE1*DEN1F(X))
      BR2RF(X)=R22F(X)*DSIF(X)/(PE2*DEN2F(X))
      BR1IF(X)=R11F(X)*DOWRF(X)/(PE1*DEN1F(X))
      BR2IF(X)=R22F(X)*DSRF(X)/(PE2*DEN2F(X))
      DAMRF(X)=BR1RF(X)+BR2RF(X)
      DAMIF(X)=BR1IF(X)+BR2IF(X)
C
C      PHYSICAL CONSTANTS FOR KCL AND CDS
      READ 11, DE1, DE2, P1, P2, V1, V2, C1, C2, T1, T2
   11 FORMAT (10F7.4)
```

```
C
C       THE FREQUENCIES FROM FIRST TO TENTH UMKLAPP PROCESSES
      READ 12, W(1),W(2),W(3),W(4),W(5),W(6),W(7),W(8),W(9),W(10)
   12 FORMAT (10F8.4)
C
C       FINDING THE CONSTANTS FOR LIGHT WAVES
      A=0.144*DE1*6.2832
      B=0.144*DE2*6.2832
      D1=0.420
      D2=0.450
      D=D1+D2
      Q1=C1/T1
      Q2=C2/T2
      GOST=COSF(A*D1)*COSF(B*D2)-(DE1*DE1+DE2*DE2)*SINF(A*D1)*SINF(B*D2)
     1/(2.0*DE1*DE2)
      ROT=SQRTF(1.0-GOST*GOST)
      XX=3.1416+ATANF(ROT/GOST)
      S=SINF(0.5*(A*D1+B*D2-XX))/SINF(0.5*(A*D1-B*D2+XX))
      BR=(DE1+DE2)*S/(DE2-DE1)
      BB=(DE1+DE2)**2*S*S/(DE2-DE1)/(DE2-DE1)
      REAB=(DE2+DE1)*S*COSF(A*D1)/(DE2-DE1)
      RIAB=(DE2+DE1)*S*SINF(A*D1)/(DE2-DE1)
      CC=(DE2+DE1)**2*(1.0+S*S+2.0*S*COSF(A*D1))/(4.0*DE2*DE2)
      DD=((DE2-DE1)**2+(DE2+DE1)**4*S*S/(DE2-DE1)**2+2.0*(DE2+DE1)**2*
     1COSF(A*D1)*S)/(4.0*DE2*DE2)
      TD=(DE2+DE1)/(4.0*DE2*DE2)
      SD=(DE2+DE1)**2/(DE2-DE1)
      RECD=TD*(DE2-DE1+SD*S*S+(SD+DE2-DE1)*S*COSF(A*D1))
      RICD=-TD*(DE2-DE1-SD)*S*SINF(A*D1)
      BOUND=4.0/((1.0+DE1)**2+(1.0-DE1)**2*BB)
      PRINT 13, BB, CC, DD, REAB, RIAB, RECD, RICD
   13 FORMAT (7H LIGHT /(7E16.5))
```

```
C
C       THE CONSTANTS RELATED TO SOUND WAVE IN (60)
      PE2=P2*V2
      PE1=P1*V1
      L=1
  100 Z1=W(L)/V1
      Z2=W(L)/V2
      SS=-1.0
  105 EPC=SS*(PE2+PE1)/(PE2-PE1)
      Z=(PE2+PE1)/(2.0*PE2)
      Y=Z*SS
      U=(PE2-PE1)/(2.0*PE2)
      V=((PE2+PE1)**2*SS)/((PE2-PE1)*2.0*PE2)
      TKC=-Z1*D1
      PRINT 110, EPC, TKC, Z, Y, U, V
  110 FORMAT (7H SOUND /(6E15.4))
      GO TO 129
  112 Z1=W(L)/V1
      Z2=W(L)/V2
      SS=1.0
      EPC=SS*(PE2+PE1)/(PE2-PE1)
      TKC=-Z1*D1
      Z=(PE2+PE1)/(2.0*PE2)
      Y=Z*SS
      U=(PE2-PE1)/(2.0*PE2)
      V=((PE2+PE1)**2*SS)/((PE2-PE1)*2.0*PE2)
      PRINT 114, EPC, TKC, Z, Y, U, V
  114 FORMAT (7H SOUND /(6E15.4))
C
C       THE FOLLOWING IS THE CALCULATION FOR F1 IN (57)
C
C       THE VARIATION OF F1 DUE TO 2 PER CENT ERRORS IN PERIODICITY
```

```
129 AT1=DE1**5*Q1*W(L)*(1.0-BB)/(6.0E+05*Z1)
    AT2=2.0*DE1**4*Q1*A/Z1
    CT1=DE2**5*Q2*W(L)*(CC-DD)/(6.0E+05*Z2)
    CT2=2.0*DE2**4*Q2*B/Z2
    KI=20
    HI=KI
130 SUM4=0.0
    SUM2=0.0
    TUM4=0.0
    TUM2=0.0
    PUM4=0.0
    PUM2=0.0
    RUM4=0.0
    RUM2=0.0
    N=1000
    FN=N
    DX=D1/FN
    EX=D2/FN
    I=1
132 FI=I
    X=-D1+FI*DX
    R=0.0+FI*EX
    SUM4=SUM4+TIONRF(X)
    SUM2=SUM2+TIONRF(X+DX)
    TUM4=TUM4+TIONIF(X)
    TUM2=TUM2+TIONIF(X+DX)
    PUM4=PUM4+SIONRF(R)
    PUM2=PUM2+SIONRF(R+EX)
    RUM4=RUM4+SIONIF(R)
    RUM2=RUM2+SIONIF(R+EX)
    IF (I-N+KI+3) 134, 136, 136
134 I=I+2
```

```
      GO TO 132
  136 CELL1R=DX*(4.0*SUM4+2.0*SUM2+TIONRF(-D1)+TIONRF(-HI*DX)+
     14.0*TIONRF(-(HI-1.0)*DX))/3.0E+05
      CELL1I=DX*(4.0*TUM4+2.0*TUM2+TIONIF(-D1)+TIONIF(-HI*DX)+
     14.0*TIONIF(-(HI-1.0)*DX))/3.0E+05
      CELL2R=EX*(4.0*PUM4+2.0*PUM2+SIONRF(0.0)+SIONRF(D2-HI*EX)+
     14.0*SIONRF(D2-(HI-1.0)*EX))/3.0E+05
      CELL2I=EX*(4.0*RUM4+2.0*RUM2+SIONIF(0.0)+SIONIF(D2-HI*EX)+
     14.0*SIONIF(D2-(HI-1.0)*EX))/3.0E+05
      CLLR=(CELL1R+CELL2R)
      CLLI=(CELL1I+CELL2I)
      SCLL=CLLR**2+CLLI**2
      PRINT 137, CELL1R, CELL1I, CELL2R, CELL2I, CLLR, CLLI, SCLL
  137 FORMAT (14H INTERGATION /(7E14.4))
      TY1=-D1*HI/FN
      TY2=D2*(FN-HI)/FN
      PX=DX/2.0
      RX=EX/2.0
      PINR=0.0
      PING=0.0
      RINR=0.0
      RING=0.0
      VARI=2.0*HI+1.0
      NI=1
  140 PI=NI
      ARG=TY1+PI*PX*2.0
      BRG=TY2+PI*RX*2.0
      PINR=(PINR+PX*(TIONRF(ARG-2.0*PX)+4.0*TIONRF(ARG-PX)+TIONRF(ARG))
     1/3.0)*(VARI-PI)/VARI
      PING=(PING+PX*(TIONIF(ARG-2.0*PX)+4.0*TIONIF(ARG-PX)+TIONIF(ARG))
     1/3.0)*(VARI-PI)/VARI
      RINR=(RINR+RX*(SIONRF(BRG-2.0*RX)+4.0*SIONRF(BRG-RX)+SIONRF(BRG))
```

```
      RING=(RING+RX*(SIONIF(BRG-2.0*RX)+4.0*SIONIF(BRG-RX)+SIONIF(BRG))
     1/3.0)*(VARI-PI)/VARI
      IF (NI-2*KI) 142, 144, 144
  142 NI=NI+1
      GO TO 140
  144 PC1R=CELL1R+PINR
      PC1I=CELL1I+PING
      PC2R=CELL2R+RINR
      PC2I=CELL2I+RING
      WRON=E1*V1*DE1/(6.0E+05*T1)
      PCR=WRON*(PC1R+RATIO*PC2R)
      PCI=WRON*(PC1I+RATIO*PC2I)
      PSC=PCR*PCR+PCI*PCI
      PRINT 146, PC1R, PC1I, PC2R, PC2I, PCR, PCI, PSC
  146 FORMAT (9H PINTEG /(7E14.4))
C
C      THE VARIATION OF F2 IN (57) DUE TO 2 PER CENT ERRORS IN PERIODICITY
      AUM4=0.0
      AUM2=0.0
      BUM4=0.0
      BUM2=0.0
      CUM4=0.0
      CUM2=0.0
      DUM4=0.0
      DUM2=0.0
      EUM4=0.0
      EUM2=0.0
      GUM4=0.0
      GUM2=0.0
      TTX=D1/1000.0
      DDT=D2/1000.0
      MI=1
```

```
147 GI=MI
    RON=(-HI+GI)*TTX
    RIC=(-1000.0-HI)*TTX+GI*TTX
    ROG=(1000.0-HI+GI)*DDT
    AUM4=AUM4+DAMRF(RON)
    AUM2=AUM2+DAMRF(RON+TTX)
    BUM4=BUM4+DAMIF(RON)
    BUM2=BUM2+DAMIF(RON+TTX)
    CUM4=CUM4+BR1RF(RIC)
    CUM2=CUM2+BR1RF(RIC+TTX)
    DUM4=DUM4+BR1IF(RIC)
    DUM2=DUM2+BR1IF(RIC+TTX)
    EUM4=EUM4+BR2RF(ROG)
    EUM2=EUM2+BR2RF(ROG+DDT)
    GUM4=GUM4+BR2IF(ROG)
    GUM2=GUM2+BR2IF(ROG+DDT)
    IF (MI-2*KI+3) 148, 149, 149
148 MI=MI+2
    GO TO 147
149 TAUR=(4.0*AUM4+2.0*AUM2+DAMRF(-HI*TTX)+DAMRF(HI*TTX)
   1+4.0*DAMRF((HI-1.0)*TTX))/6.0/HI
    TAUI=(4.0*BUM4+2.0*BUM2+DAMIF(-HI*TTX)+DAMIF(HI*TTX)
   1+4.0*DAMIF((HI-1.0)*TTX))/6.0/HI
    SHER=(4.0*CUM4+2.0*CUM2+BR1RF(-D1-HI*TTX)+BR1RF(-D1+HI*TTX)
   1+4.0*BR1RF(-D1+(HI-1.0)*TTX))/6.0/HI
    SHEI=(4.0*DUM4+2.0*DUM2+BR1IF(-D1-HI*TTX)+BR1IF(-D1+HI*TTX)
   1+4.0*BR1IF(-D1+(HI-1.0)*TTX))/6.0/HI
    CHER=(4.0*EUM4+2.0*EUM2+BR2RF(D2-HI*DDT)+BR2RF(D2+HI*DDT)
   1+4.0*BR2RF(D2+(HI-1.0)*DDT))/6.0/HI
    CHEI=(4.0*GUM4+2.0*GUM2+BR2IF(D2-HI*DDT)+BR2IF(D2+HI*DDT)
   1+4.0*BR2IF(D2+(HI-1.0)*DDT))/6.0/HI
    HSIN=(E2-E1)/(4.0E+03*W(L))
```

```
      CONR=HSIN*(TAUR-SHER-CHER)
      CONI=HSIN*(TAUI-SHEI-CHEI)
      SCON=CONR*CONR+CONI*CONI
      PRINT 152, CONR, CONI, SCON
  152 FORMAT (8H DISCON /(3E20.4))
      SAMP=(CONR+CLLR)**2+(CONI+CLLI)**2
      PRINT 153, SAMP
  153 FORMAT (6H SAMP ,1E20.5)
C
C      CALCULATE THE SOUND POWER
      BOR=V2*T2*Z2*Z2*BOUND*BOUND/(72.0*1.0E+05)
      TOR=BOR*3.2415
      AUM=TOR*SCLL
      DIS=TOR*SCON
      POWER=TOR*SAMP
      PRINT 154, AUM, DIS, POWER
  154 FORMAT (7H POWER /(3E30.4))
      IF (L-10) 160, 180, 180
  160 L=L+1
      GO TO 163
  163 IF (L-2) 164, 164, 165
  164 GO TO 112
  165 IF (L-4) 166, 167, 168
  166 GO TO 100
  167 GO TO 112
  168 IF (L-6) 169, 170, 171
  169 GO TO 100
  170 GO TO 112
  171 IF (L-8) 172, 173, 174
  172 GO TO 100
  173 GO TO 112
  174 IF (L-10) 175, 176, 180

  175 GO TO 100
  176 GO TO 112
  180 CALL EXIT
      END
```

REFERENCES

1. F. Zernike, Jr. and Paul R. Berman, Phys. Rev. Letters 15, 999 (1965).
2. F. Zernike, Phys. Rev. Letters 18, 931 (1969).
3. V. T. Nguyen and C. K. N. Patel, Phys. Rev. Letters 22, 463 (1969).
4. C. K. N. Patel and V. T. Nguyen, Appl. Phys. Letters 15, 189 (1969).
5. F. Zernike, Phys. Rev. Letters 22, 93 (1969).
6. T. J. Bridges and A. R. Strand, Appl. Phys. Letters 20, 382 (1972).
7. G. D. Boyd, T. J. Bridges, C. K. N. Patel, and E. Buehler, Appl. Phys. Letters 21, 553 (1972).
8. Van Tran Nguyen and T. J. Bridges, Phys. Rev. Letters 29, 359 (1972).
9. R. L. Aggarwal, B. Lax, and G. Favrot, Appl. Phys. Letters 22, 329 (1972). Also, B. Lax, R. L. Aggarwal, G. Favrot, Appl. Phys. Letters 23, 679 (1973).
10. D. W. Faries, K. A. Gehring, P. L. Richards, and Y. R. Shen, Phys. Rev. 180, 363 (1969); D. W. Faries, P. L. Richards, Y. R. Shen, and K. H. Yang, ibid. A3, 2148 (1971).
11. K. H. Yang, J. R. Morris, P. L. Richards, and Y. R. Shen, Bull. Am. Phys. Soc. series 2, 18, 350 (1973).
12. D. H. Auston, A. M. Glass, and P. LeFur, Appl. Phys. Letters 23, 47 (1973).
13. D. H. Martin, Spectroscopic Techniques for Far-Infrared, Submillimeter and Millimeter Waves, Ed. D. H. Martin, (North-Holland Publishing Co., Amsterdam, 1967).
14. T. Yeon, Generation des ondes millimetriques et submillimetriques. In: Proc. 5th Intern. Congr. on Microwave Tubes, Paris 1964 (Academic

Press, New York and London, 1965).

15. P. L. Richards, in Spectroscopic Techniques, edited by D. H. Martin (North-Holland, Amsterdam, 1967) Chapter 2.

16. D. H. Martin and E. Puplett, Infrared Physics Vol. 10, P. 105 (Pergamon Press printed in Britain).

17. D. G. Vickers, E. I. Robson, and J. E. Beckman Applied Optics 10, 682 (1971).

18. K. H. Yang, P. L. Richards, and Y. R. Shen, Appl. Phys. Letters 19, 320 (1971).

19. Richard R. Joyce, Ph.D Thesis 1970, Dept. of Physics, University of California, Berkeley (unpublished).

20. R. Ulrich, K. F. Renk, and L. Genzel, IEEE Trans. Microwave Theory Tech. MTT-11, 363 (1963).

21. K. H. Yang, J. R. Morris, P. L. Richards, and Y. R. Shen. Appl. Phys. Letters 23, 669 (1973).

22. T. K. Gustafson, J. P. E. Taran, P. L. Kelley, and R. Y. Chias, Optics Commun. 2, 17 (1970).

23. J. R. Morris and Y. R. Shen, Optics Commun. 3, 81 (1971).

24. J. R. Morris, Ph.D. Thesis 1974, Dept. of Physics, University of California, Berkeley (unpublished).

25. See, e.g. N. Bloembergen, Nonlinear Optics (W. A. Benjamin, Inc., New York, 1965) P. 75.

26. A. S. Barker, Jr. and R. London, Phys. Rev. 158, 433 (1967).

27. H. P. Weber, Phys. Lett. 27A, 321 (1968).

28. P. P. Bey and H. Rabin, Phys. Rev. 162, 794 (1967).

29. E. H. Putley and D. H. Martin, in Spectroscopic Techniques, edited by D. H. Martin (North-Holland, Amsterdam, 1967), P. 113.

30. The liquid helium bath temperature was regulated by a thermal bridge, see, G. I. Rochlin, Rev. Sci. Instr. 11, 73 (1970).

31. P. L. Richards, Pure and Appl. Chem. 11, 535 (1965).

32. A. Yariv, Quantum Electronics (Wiley, New York, 1967) P. 302.

33. D. R. Bosomworth, Appl. Phys. Letters 9, 330 (1966).

34. G. D. Boyd, Robert C. Miller, K. Nassau, W. L. Bond, and A. Savage, Appl. Phys. Letters 5, 234 (1964).

35. T. Yajima and N. Takeuchi, Japanese J. of Appl. Phys. 9, 1361 (1970).

36. N. Takeuchi, N. Matsumoto, T. Yajima, and S. Kishida, Jap. J. of Appl. Phys. 11, 268 (1972).

37. D. H. Auston, A. M. Glass, and A. A. Ballman, Appl. Phys. Letters 28, 897 (1972).

38. D. H. Auston and A. M. Glass, Appl. Phys. Letters 20, 398 (1972).

39. D. W. Faries, Ph.D. Thesis 1969, Dept. of Physics, University of California (unpublished).

40. See, e.g. Born and Wolf, Principles of Optics (Pergamon Press, Fourth Edition 1970), P. 684.

41. For light propagating normal to a birefringent crystal slab as an e-ray, the walk-off angle ρ can be calculated from the formula $\tan\rho = \frac{1}{2} n_o^2 \left\{ \frac{1}{n_e^2} - \frac{1}{n_o^2} \right\} \sin 2\theta$, where n_o, n_e are refractive indices of o-ray and e-ray respectively, and θ is angle between the normal and the c-axis of the crystal.

42. C. H. Henry and C. G. B. Garrett, Phys. Rev. 171, 1058 (1968).

43. S. S. Sussman, Ph.D. Thesis 1969, Dept. of Phys. Stanford University (unpublished).

44. Y. Yariv, Quantum Electronics (John Wiley, N. Y., 1967). Append. 3.

45. Herschel S. Pilloff, Appl. Phys. Letters 21, 15 (1972). We independently developed this laser scheme.

46. P. P. Sorokin, J. R. Lankard, E. C. Hammond, V. L. Mouzzi, IBM Journal 11, 130 (1967).

47. D. J. Bradley, G. M. Gale, M. Moore, and P. D. Smith, Physics Letters, 26A, 378 (1968).

48. See J. A. Armstrong, App. Phys. Letters 9, 72 (1966), for a similar scheme for sum frequency generation in transmission.

49. M.A.C.S. Brown and M. F. Kimmett, Brit. Commun. Electron 10, 608 (1963); Infrared Physics 5, 93 (1965).

50. W. J. Moore and H. Shenker, Infrared Physics 5, 99 (1965).

51. SP. 50 Golay pneumatic cell from Pye Unican Ltd., England.

52. Handbook, American Institute of Physics, Third Edition, (McGraw-Hill, 1972), P. 6-280. We measured this result by a conventional Faurier transform spectroscopy also.

53. We used the optical refractive index of W. L. Bond, J. of Appl. Physics 36, 1674 (1965).

54. We used the far-infrared data of R. J. Collins, D. A. Kleiman, J. Physics. Chem. Solids 11, 190 (1959).

55. We used the optical refractive index of T. M. Bienieuski, S. J. Czyzak, J. Opt. Soc. Am. 53, 496 (1963).

56. We used the dc dielectric constant of R. H. Bube, Proc. IRE 43, 1836 (1955).

57. We used infrared reflection data of H. W. Verdeur and A. S. Barker, Jr. Phys. Rev. 155, 750 (1967).

58. The far-infrared measurement by W. M. Senton, W. C. Davis, J. Opt. Soc. Am 44, 503 (1954), was not very good.

59. Lindgren, Statistical Theory, (Macmilton, N. Y., 1962) P. 386.

60. S. Ushioda and J. D. McMullen, Solid States Commun. 11, 299 (1972).

61. I. P. Kaminow and W. D. Johnston, Jr., Phys. Rev. 160, 519 (1967).

62. T. W. Hansch, Appl. Opt. 11, 895 (1972).

63. John Clarke, G. I. Hoffer, and P. L. Richards (to be published).

64. John C. Mather (private communication).

65. I. S. Rez, Soviet Physics USPEKHI, 10, 759 (1968).

66. P. V. Lenzo, E. G. Spencer, and A. A. Ballman, IEEE J. Quant. Electronics QE 3, No. 6, 259 (1967).

67. Y. R. Shen, Appl. Phys. Letters 23, 516 (1973).

68. V. T. Nguyen and C. K. N. Patel, Phys. Rev. Lett. 26, 1170 (1969).

69. C. K. N. Patel, Symposium on Modern Optics, (Polytechnic Institute of Brooklyn, 1967), P. 19.

70. H. Brunner and K. F. Renk, J. of Appl. Physics 41, 2250 (1970).

71. P. L. Richards, J. of Appl. Phys. 35, 850 (1964).

72. P. A. Young, Thin Solid Films 4, 25 (1969).

73. R. M. MacFarlane, Phys. Rev. Lett. 25, 1454 (1970).

74. S. J. Allen and H. J. Guggenheim, Phys. Rev. Lett. 27, 1807 (1968).

75. J. Ilukor and E. H. Jacobsen, in Physical Acoustic, edited by W. P. Mason (Academic, N. Y., 1968), Vol. 5.

76. R. J. VonGutfeld, A. H. Nethercot, Jr., and J. A. Armstrong, Phys. Rev. 142, 436 (1966).

77. R. J. VonGutfeld, in Physical Acoustic, edited by W. P. Mason (Academic, N. Y., 1968), Vol. 5.

78. V. Narayanamurti and R. C. Dynes, Phys. Rev. Lett. 27, 410 (1971).

79. N. Bloembergen and A. J. Sievers, Appl. Phys. Letters 17, 483 (1970).

80. A. E. Blakeslee and C. F. Aliotta, IBM J. Res. Dev. 14, 686 (1970).

81. A. Y. Cho, Appl. Phys. Letters 19, 467 (1971).

82. N. F. Foster, J. Vac. Sci. Technol. 6, 111 (1969).

83. L. I. Maissel and R. Glang, Handbook of Thin Film Technology (McGraw-Hill, N. Y., 1970), P. 15-1.

84. A. R. Verma, Polymorphism and Polytypison in Crystals, (John Wiley, N. Y., 1966), P. 61.

85. L. Holland, Vacuum Deposition of Thin Films, (Wiley, N. Y., 1958).

86. R. Tsu and Sudhanshu S. Jha, Appl. Phys. Letters 20, 16 (1972). In this paper, the phonon attenuation was neglected in the calculation of the polariton modes,

87. R. J. King and H. M. Rosenberg, Proc. Roy. Soc., Ser. A315, 369(1970).

88. L. M. Brekhovskikh, Waves in Layered Media, translated by D. Lieberman (Academic, N. Y., 1966), P. 85.

89. H. Kogelnik and C. V. Shank, Appl. Phys. Letters 18, 152 (1971).

90. L. H. Lin, Appl. Opt. 8, 963 (1969).

91. L. L. Chang, L. Esaki, W. E. Howard, and R. Ludeke, J. Vac. Sci. Technol. 10, 11 (1973).

92. Goro Honjo, Shizuo Miyake, and Takanori Tomita. Silicon carbide of 594 layers, Acta Cryst. 3, 396 (1950).

93. Lyle Patrick, W. J. Choyke, and D. R. Hamilton, Phys. Rev. 137, A1515 (1965).

94. W. T. Choyke and Lyle Patrick, Phys. Rev. 127, 1868 (1962).

95. Lyle Patrick, D. R. Hamilton, and W. J. Choyke, Phys. Rev. 132, 2023 (1963).

96. D. R. Hamilton, Lyle Patrick, and W. J. Choyke, Phys. Rev. 138, A1472 (1965).

97. L. S. Ramsdell and R. S. Mitchell, Am. Mineralogist 38, 56 (1953).

98. D. H. Martin and G. R. Dean (to be published).

99. S. B. Field and D. H. Martin, Proc. Phys. Soc., 78, 625 (1961).

FIGURE CAPTIONS

Fig. 1. Experimental scheme for measuring the spectra of mixing picosecond optical pulses in $LiNbO_3$. In the case of phase-matched at finite frequency, some spectra were measured using the same scheme except that the Michelson interferometer was replaced by a Fabry-Perot interferometer.

Fig. 2. The detailed construction of the Michelson interferometer used to measure the far-infrared spectra in the picosecond pulse experiments.

Fig. 3. The drawing of the Fabry-Perot interferometer utilized in the picosecond pulse experiments to measure the narrow spectral peaks produced from the case of phase-matching at finite frequency. The micrometers used to adjust the parallelism of the two metal-mashed reflectors are not shown in the figure.

Fig. 4. The far-infrared dual detector system used in the picosecond pulse experiments. The whole system was immersed in a liquid helium dewar.

Fig. 5. (a) The Ge:Ga photoconductive detector used to detect the far-infrared radiation from 95 to 190 cm^{-1} produced by mixing two dye laser beams. (b) The diagram shows the bias and the operational amplifier used in the picosecond pulse experiments as well as in the experiment of mixing two dye lasers.

Fig. 6. (a) Far-infrared spectrum generated by mode-locked pulses in $LiNbO_3$ phase-matched at zero frequency. The experimental points are obtained from the Michelson interferogram and the solid curve from a theoretical calculation by J. R. Morris assuming Gaussian laser

pulses of 1.8-psec pulsewidth. (b) Far-infrared spectrum generated by mode-locked pulses in $LiNbO_3$ oriented to have forward and backward phase-matching at 13.5 and 6.7 cm^{-1}, respectively. The experimental points are obtained from the Michelson interferogram. The solid and dashed curves are calculated assuming Gaussian laser pulses with a pulsewidth of 2.3 and 1.8 psec. respectively. In this experiment, our laser condition is somewhat different than in the other experiments, and it is very likely that the output pulses are longer.

Fig. 7. Fabry-Perot fringes of far-infrared radiation generated by mode-locked pulses in $LiNbO_3$ simultaneously phase-matched at 13.5 and 6.7 cm^{-1}. The curve is calculated from the dashed theoretical spectrum in Fig. 6(b) corresponding to Gaussian laser pulses of a 1.8 psec pulsewidth.

Fig. 8. Fabry-Perot fringes of far-infrared radiation generated by mode-locked pulses in $LiNbO_3$ simultaneously phase-matched at 11 and 5.5 cm^{-1}. The curve is the theoretical calculation from the result of theoretical spectrum similar to the dashed spectrum in Fig. 6(b). The Gaussian laser pulse corresponds to a pulsewidth of 1.8 psec.

Fig. 9. (a) The diagram shows the effect of the divergent input laser beams on the phase-matching factor in the experiment of collinearly mixing two dye lasers, where δ denoted the divergence angle of the input laser beams. (b) In the non-collinear phase-matching scheme, two input laser beams cross at an angle ψ. Under the phase-matched condition, there exists a phase mismatch, Δk, caused by the input laser divergence.

Fig. 10. One-dye-cell scheme for the far-infrared generation set-up. The wavelength of the two beams can be independently varied from 8100 to 8400 Å. The diagram for the ruby pump system is not shown in this figure, but depicted in Fig. 11.

Fig. 11. Two-dye-cell scheme used for the collinear (both forward and backward) phase-matching experiments. The ruby oscillator was Q-switched by a rotating prism.

Fig. 12. Another two-dye-cell scheme used for the non-collinear phase-matching experiment. The diagram of the ruby pump system shown in Fig. 11 is omitted.

Fig. 13. Typical Fabry-Perot interference fringe resulted from mixing of two dye lasers in $LiNbO_3$. The curve is for the illustration and is not a theoretical calculation.

Fig. 14. Theoretical calculations of the phase-matching frequency vs. the phase-matching angle for $LiNbO_3$, ZnO, ZnS, and CdS crystals in the collinear phase-matching case.

Fig. 15. Phase-matching curves. The outer one is forward collinear phase-matching curve for 21 cm^{-1} in a 1.6-mm $LiNbO_3$ crystal; the inner one is backward collinear phase-matching curve for 56 cm^{-1} in a 0.5-mm $LiNbO_3$ crystal. The solid curves are the theoretical calculations. From the outer curve and the measured α_3 of 14 cm^{-1}, we deduced the far-infrared linewidth of 3 cm^{-1}. From inner curve we obtained $\alpha_3 = 236$ cm^{-1}.

Fig. 16. Another two collinear forward phase-matching curves in two 0.5-mm thick $LiNbO_3$ crystals. The solid curves are the theoretical calculations from which we deduced the far-infrared absorption

constants and their standard deviations.

Fig. 17. The far-infrared o-ray absorption constant vs. w_3. The dots and associated error bars are deduced from the phase-matching curves. The solid curve is the experimental results obtained by the far-infrared transmission measurement of Bosomworth for $w_3 \leq 70$ cm^{-1} and the far-infrared reflection measurement of Barker and Loudon for $w_3 > 70$ cm^{-1}.

Fig. 18. Far-infrared power generated vs. frequency for three phase-matching conditions. The far-infrared power is normalized by a sum frequency signal. The solid curves are based on data of the far-infrared absorption and the Raman cross-section in $LiNbO_3$.

Fig. 19. The dispersion of $\chi_{24}^{(2)}$ vs. frequency in $LiNbO_3$. The dots are experimental results deduced from the forward collinear phase-matched experiments. The solid curve is the theoretical calculation using the oscillator strengths of A. S. Barker, Jr., and R. Loudon, and Raman cross section of I. P. Kaminow and W. D. Johnston, Jr.

Fig. 20. The circular points are the calculated conversion efficiencies for various orders of umklapp process using a piezoelectric super-lattice consisting of 100 epitaxial layers of GaAs:GaP with a total thickness of 6.34 u. The triangular points give the conversion efficiency if the periodicity of the superlattice has a $\pm$ 2% random variation. Note the break in the vertical scale.

Fig. 21. The circular points are the calculated coherent phonon power (divided by the product of the powers of two mixing ruby laser beams) for various orders of umklapp process in a super-lattice of 100 alternating vacuum evaporated layers of KCl:CdS with a total thickness

of 8.7 u. The triangular points give the phonon power if the periodicity of the superlattice has a 2% random variation. Note the break in the vertical scale.

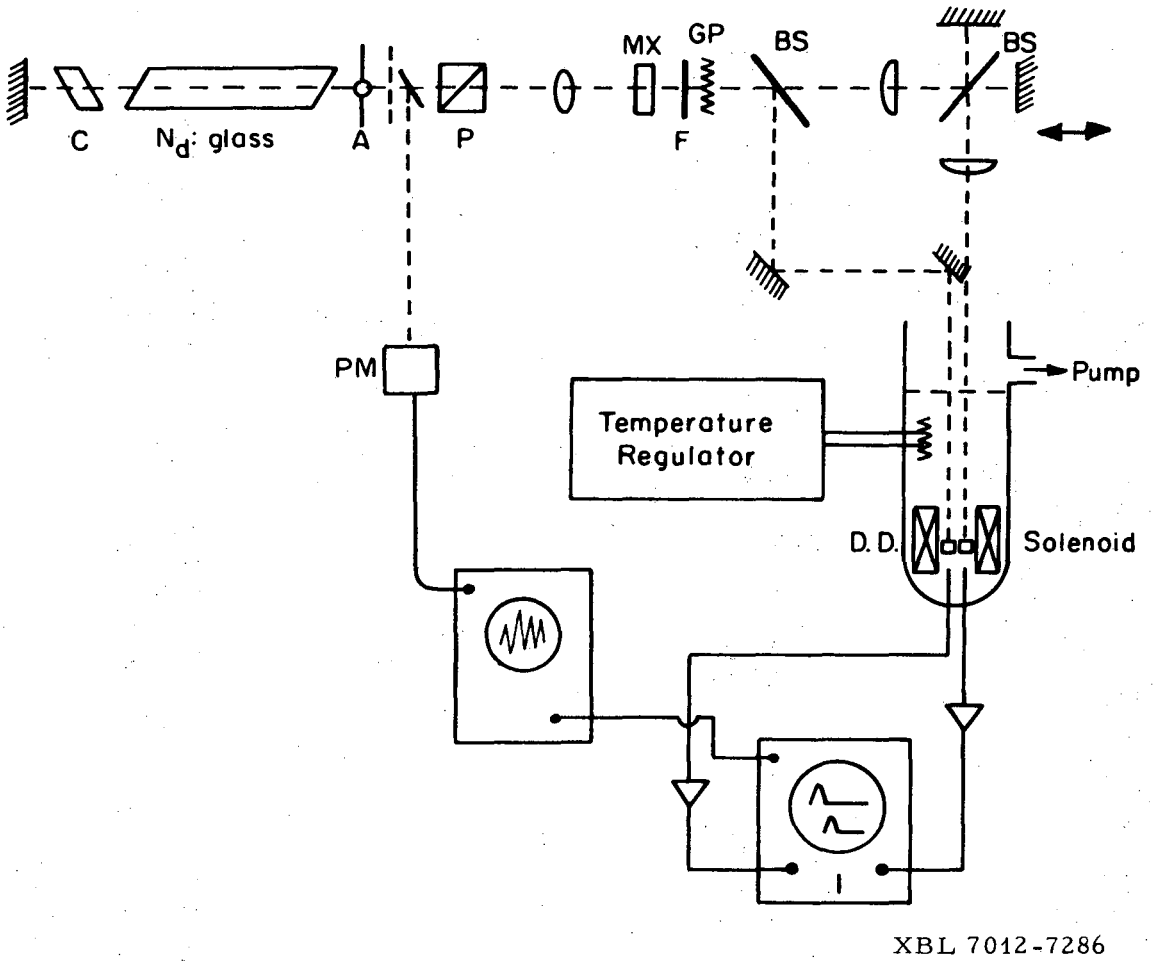
C
N_d: glass
A
P
MX
GP
F
BS
BS
PM
Temperature Regulator
Pump
D. D.
Solenoid
I
XBL 7012-7286

Fig. 1

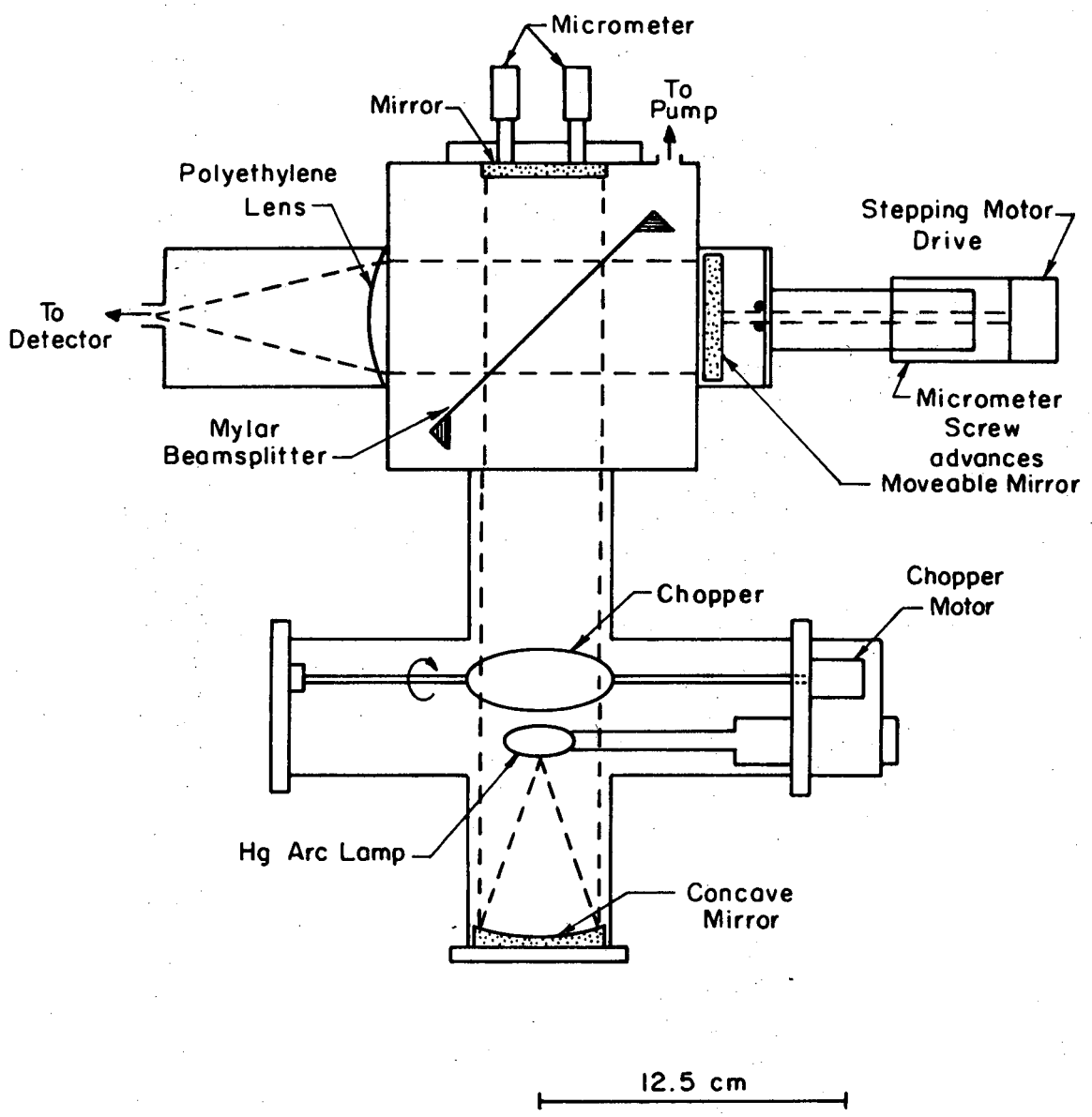

XBL 7011-6927

Fig. 2

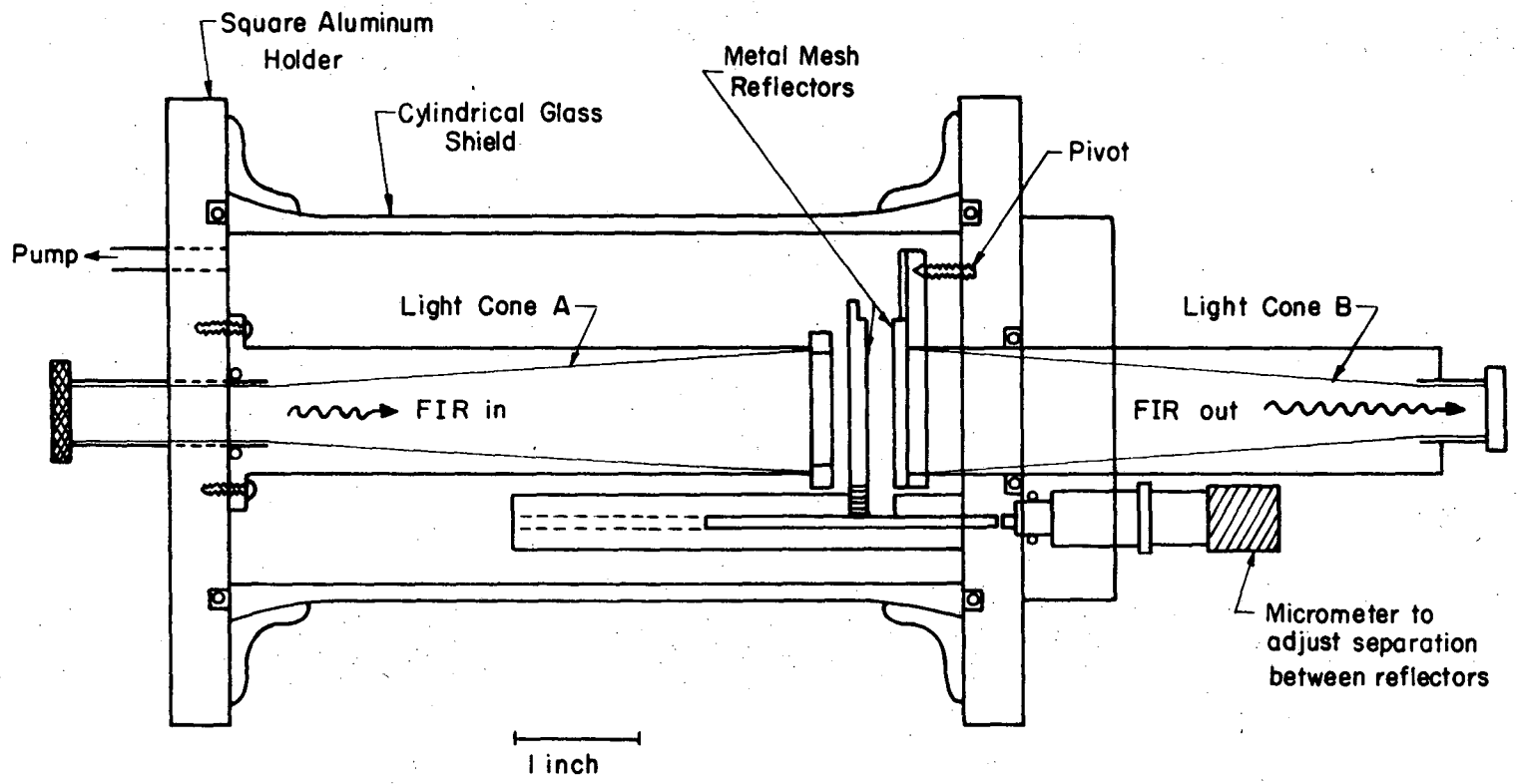

XBL 739-1915

Fig. 3

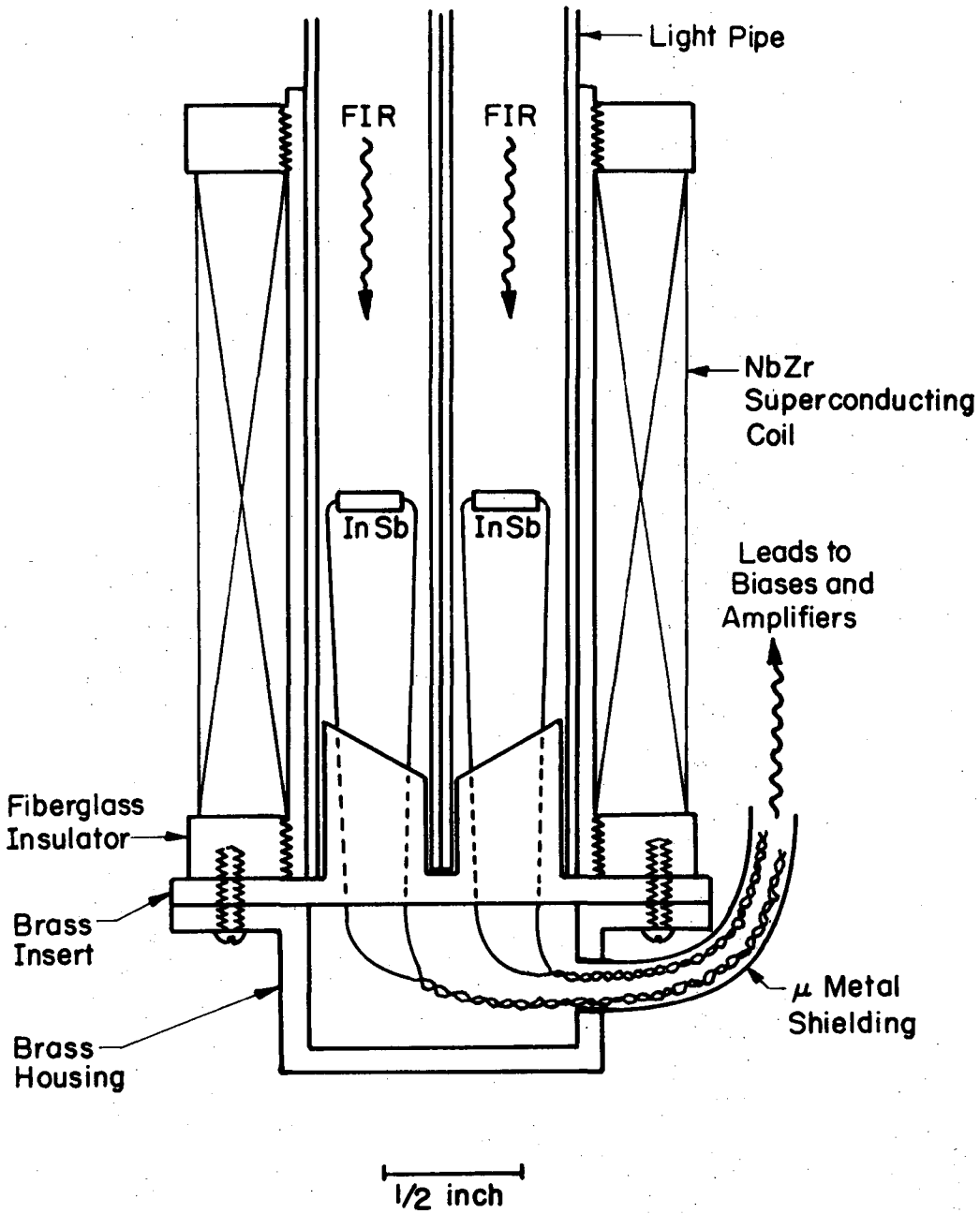

XBL 739-1916

Fig. 4

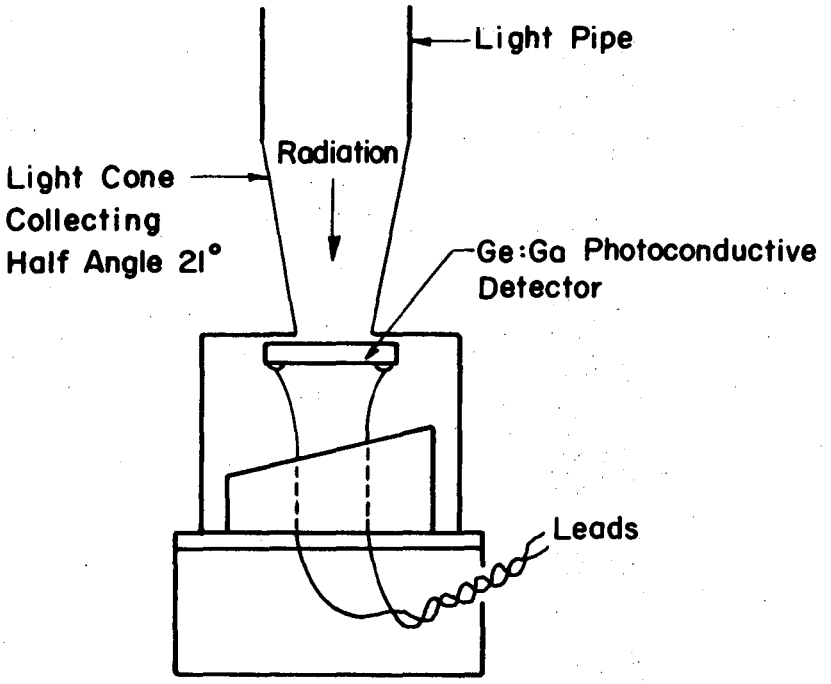

(a) Ge:Ga Detector

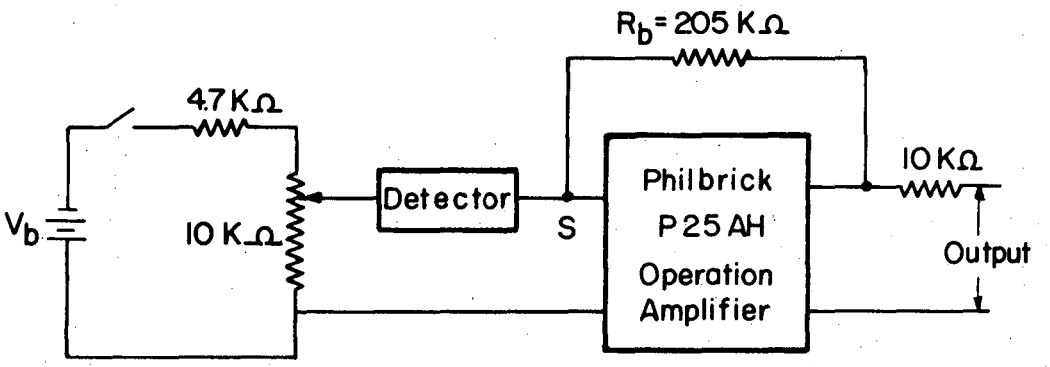

V_b = 1.5 V for InSb Detector
= 9.0 V for Ge:Ga Detector

(b) Operation Amplifier

XBL 739-1917

Fig. 5

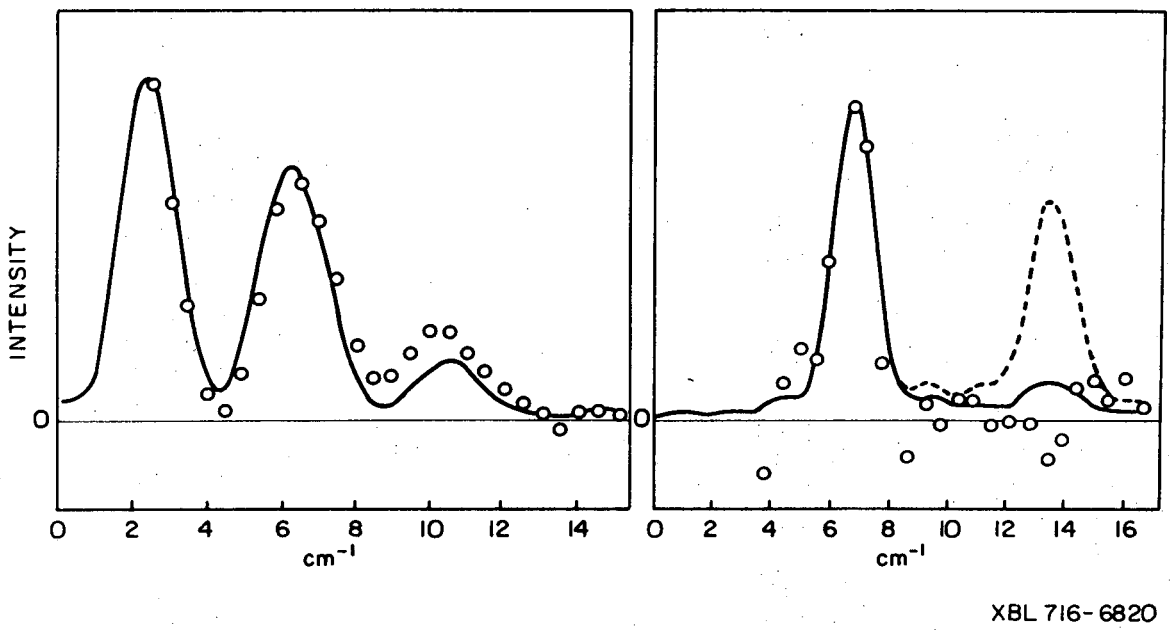
INTENSITY
0
0
2
4
6
8
10
12
14
cm⁻¹
0
2
4
6
8
10
12
14
16
cm⁻¹
XBL 716-6820

Fig. 6

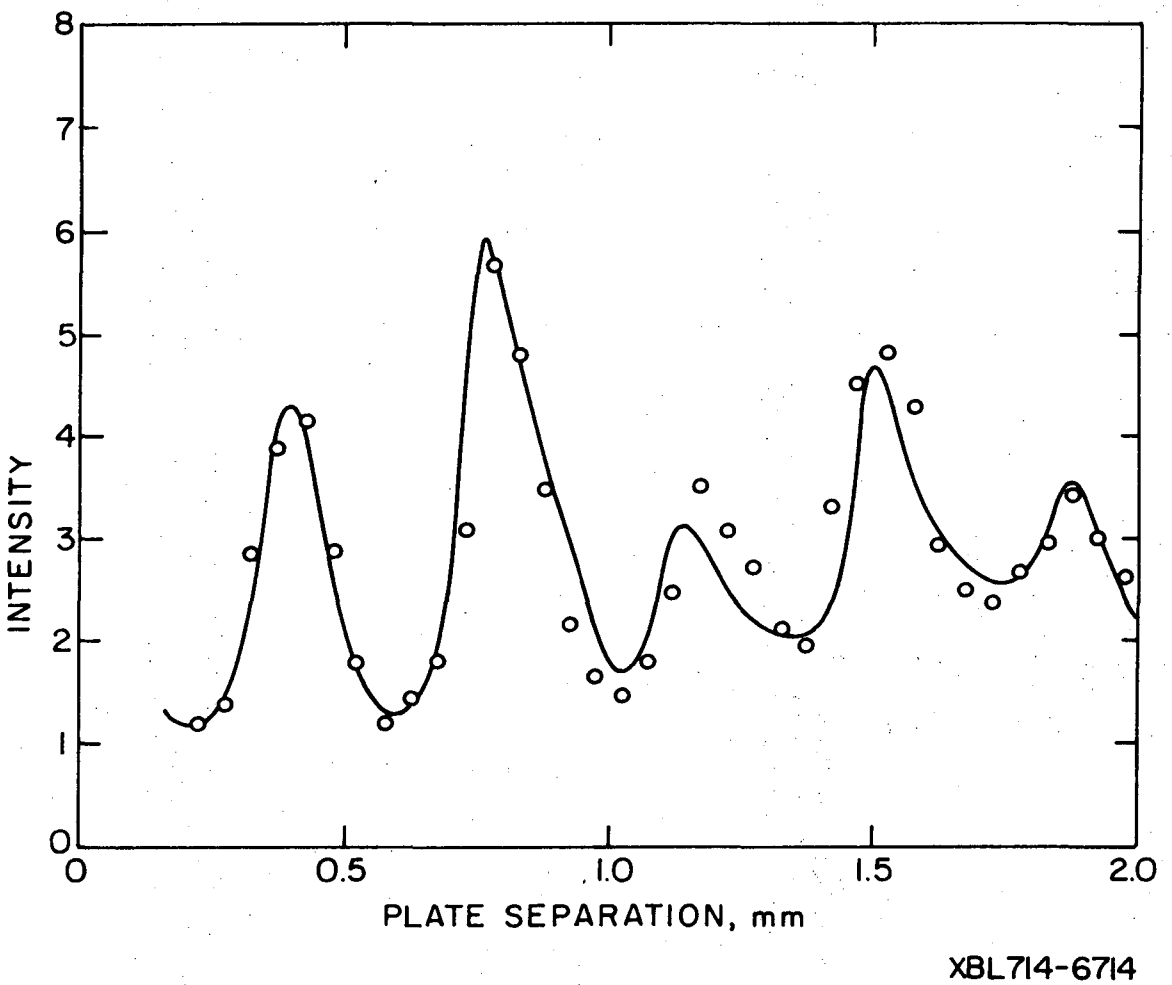
8
7
6
5
4
3
2
1
0
INTENSITY
0
0.5
1.0
1.5
2.0
PLATE SEPARATION, mm
XBL714-6714

Fig. 7

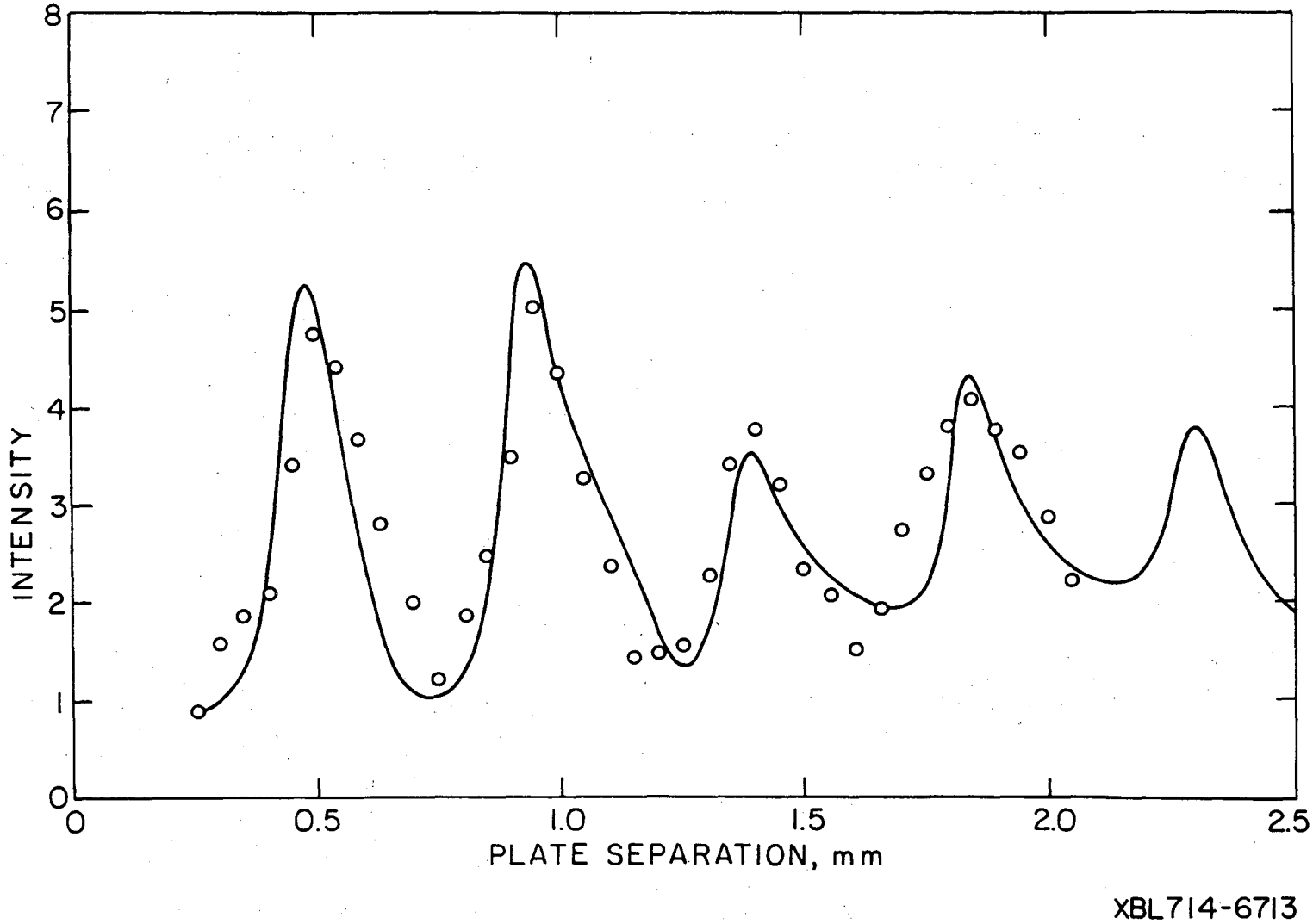
INTENSITY
0
1
2
3
4
5
6
7
8
0
0.5
1.0
1.5
2.0
2.5
PLATE SEPARATION, mm
XBL714-6713

Fig. 8

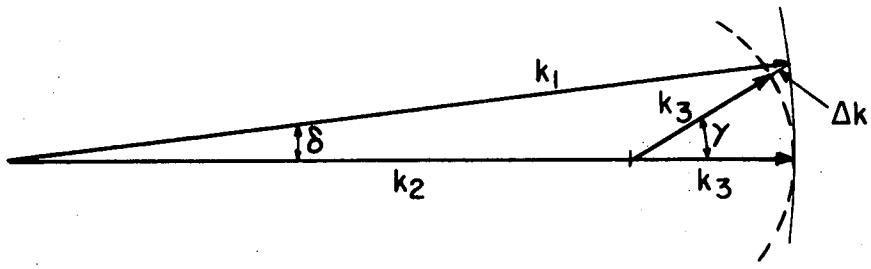

$$\Delta k = \sqrt{k_3^2 + (k_1\delta)^2} - k_3 \cong \frac{(k_1\delta)^2}{2k_3}$$

$$\gamma = \delta \frac{k_1}{k_3}$$

(a) Collinear Case

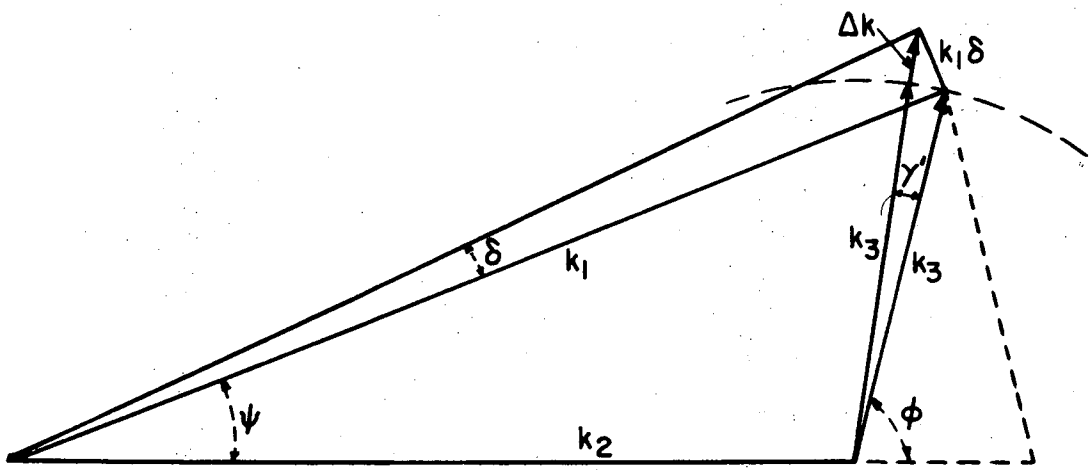

$$\Delta k \cong k_1\delta \sin\phi \cong 137\ \mathrm{cm}^{-1}$$

(b) Non-collinear Case

XBL 739-1918

Fig. 9

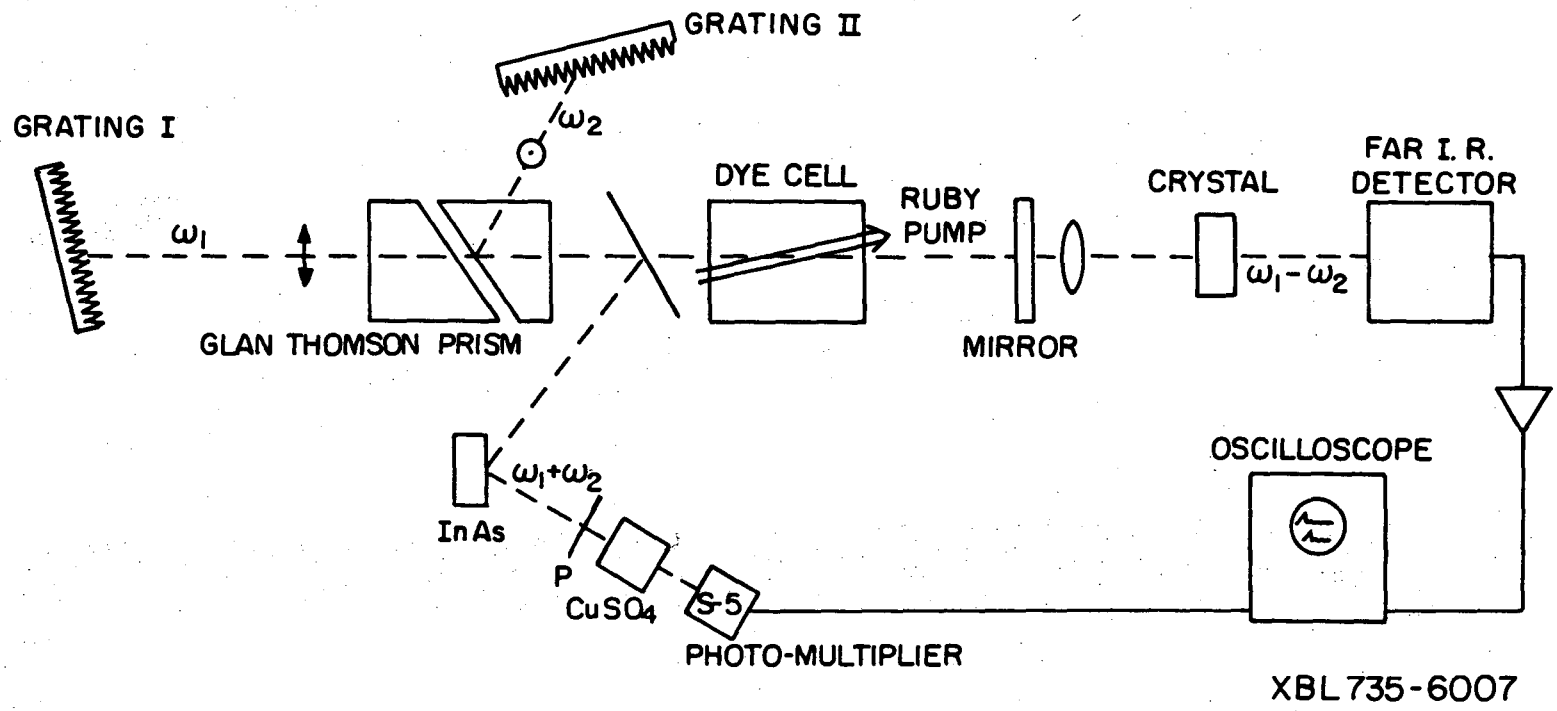
GRATING II
GRATING I
ω_2
ω_1
DYE CELL
RUBY
PUMP
CRYSTAL
FAR I. R.
DETECTOR
$\omega_1 - \omega_2$
GLAN THOMSON PRISM
MIRROR
OSCILLOSCOPE
$\omega_1 + \omega_2$
InAs
P
$CuSO_4$
S-5
PHOTO-MULTIPLIER
XBL 735-6007

Fig. 10

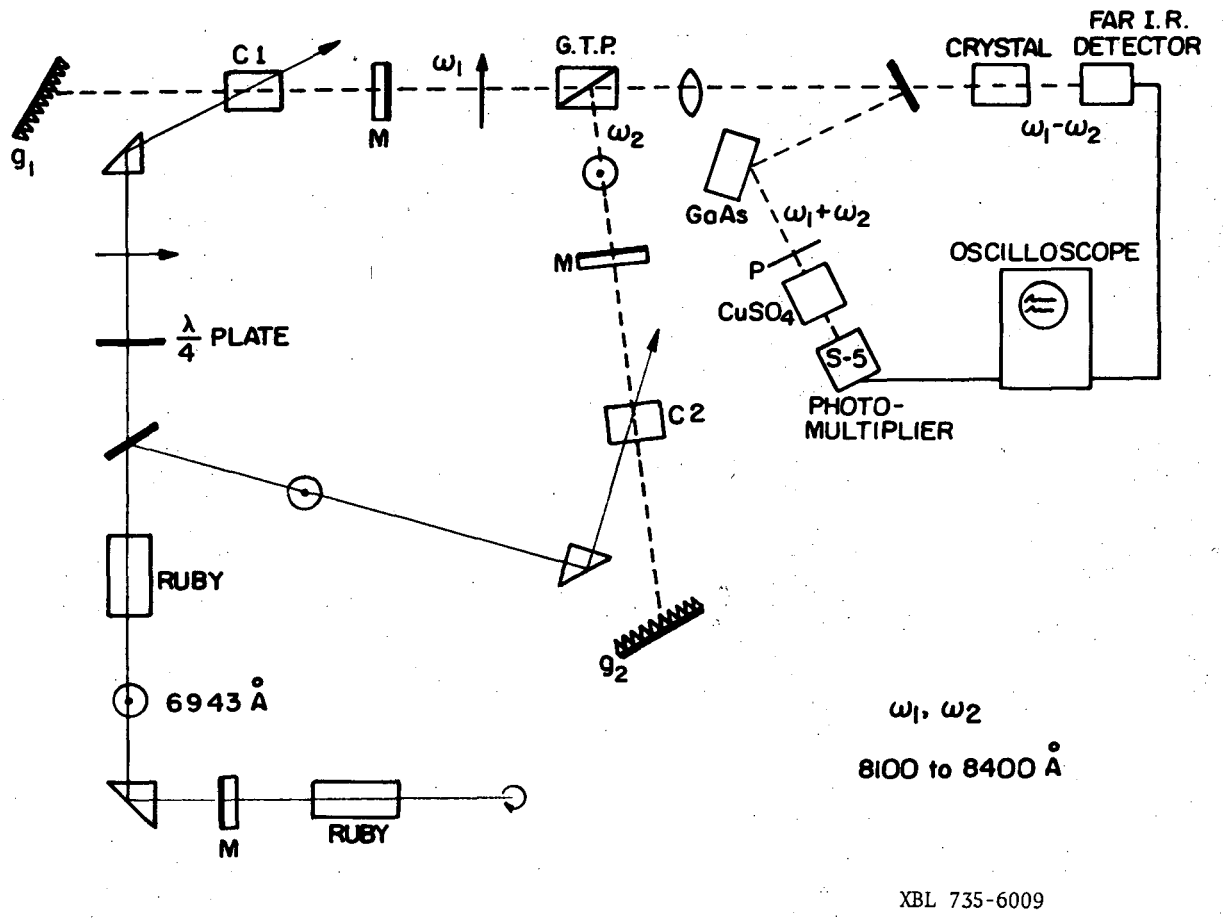
C1
M
ω_1
G.T.P.
ω_2
CRYSTAL
FAR I.R. DETECTOR
$\omega_1-\omega_2$
g_1
GaAs
$\omega_1+\omega_2$
M
P
$CuSO_4$
OSCILLOSCOPE
$\frac{\lambda}{4}$ PLATE
S-5
PHOTO-MULTIPLIER
C2
RUBY
g_2
6943 Å
ω_1, ω_2
8100 to 8400 Å
M
RUBY
XBL 735-6009

Fig. 11

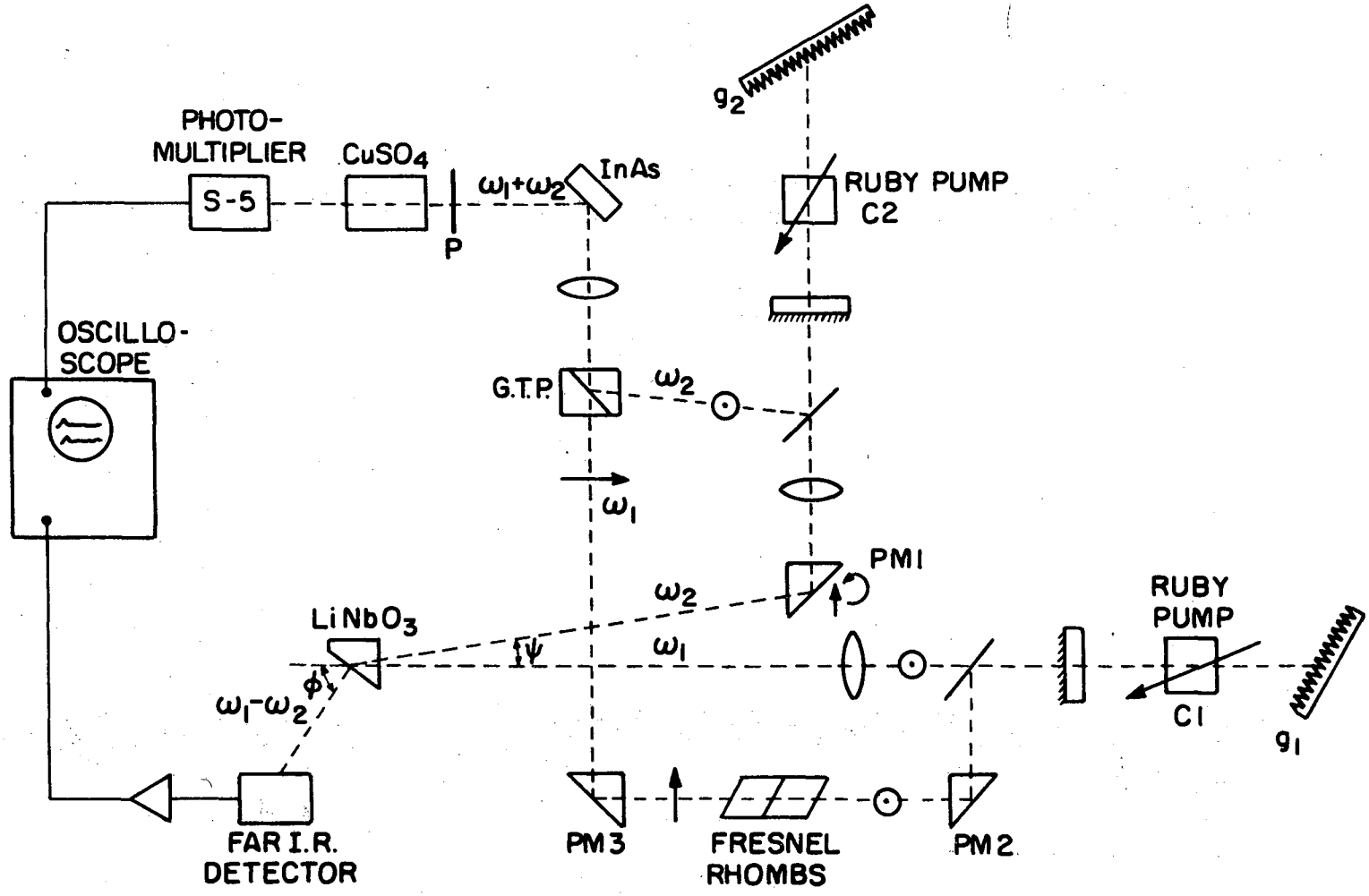

XBL 736-6306

Fig. 12

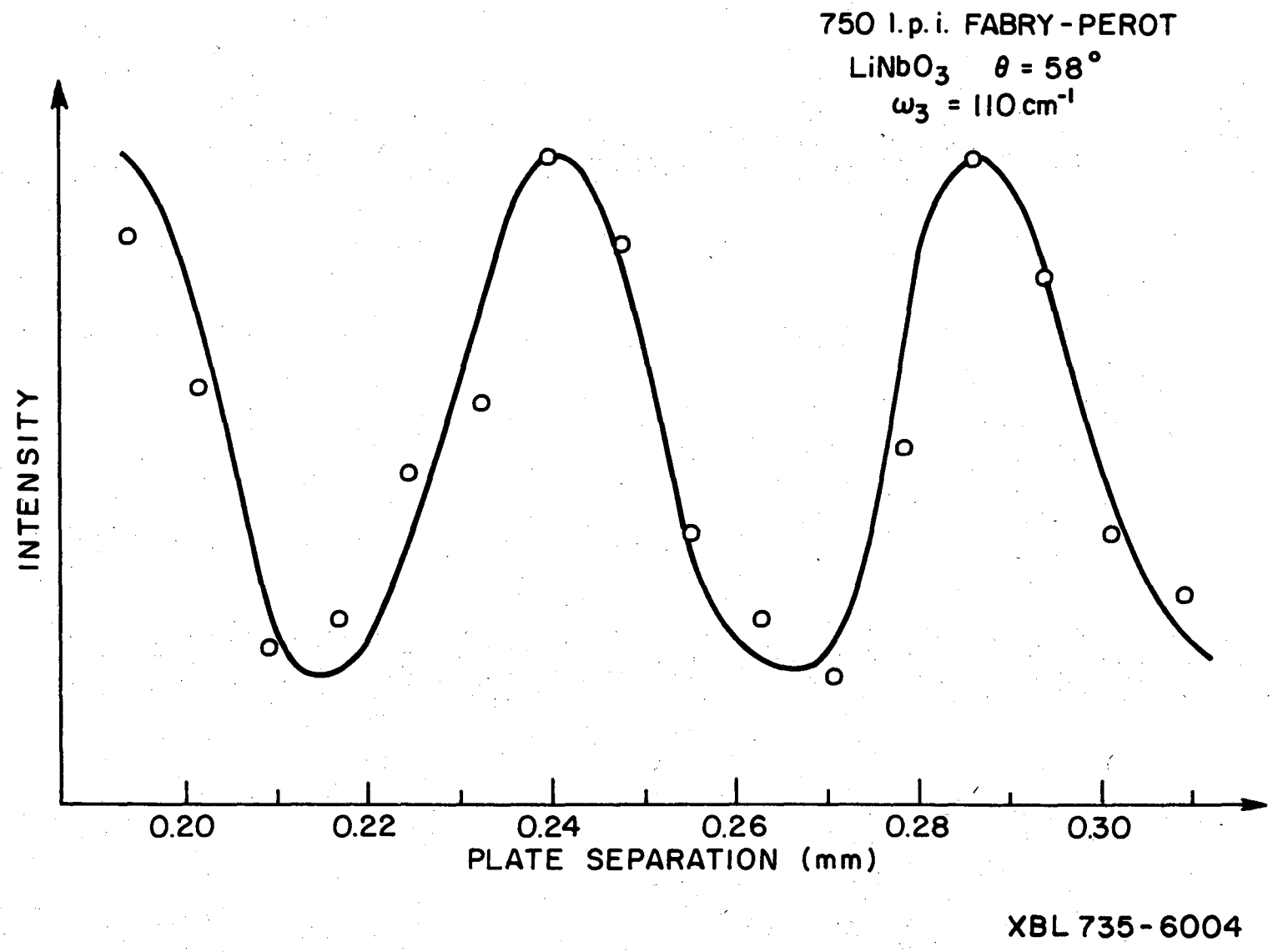

XBL 735-6004

Fig. 13

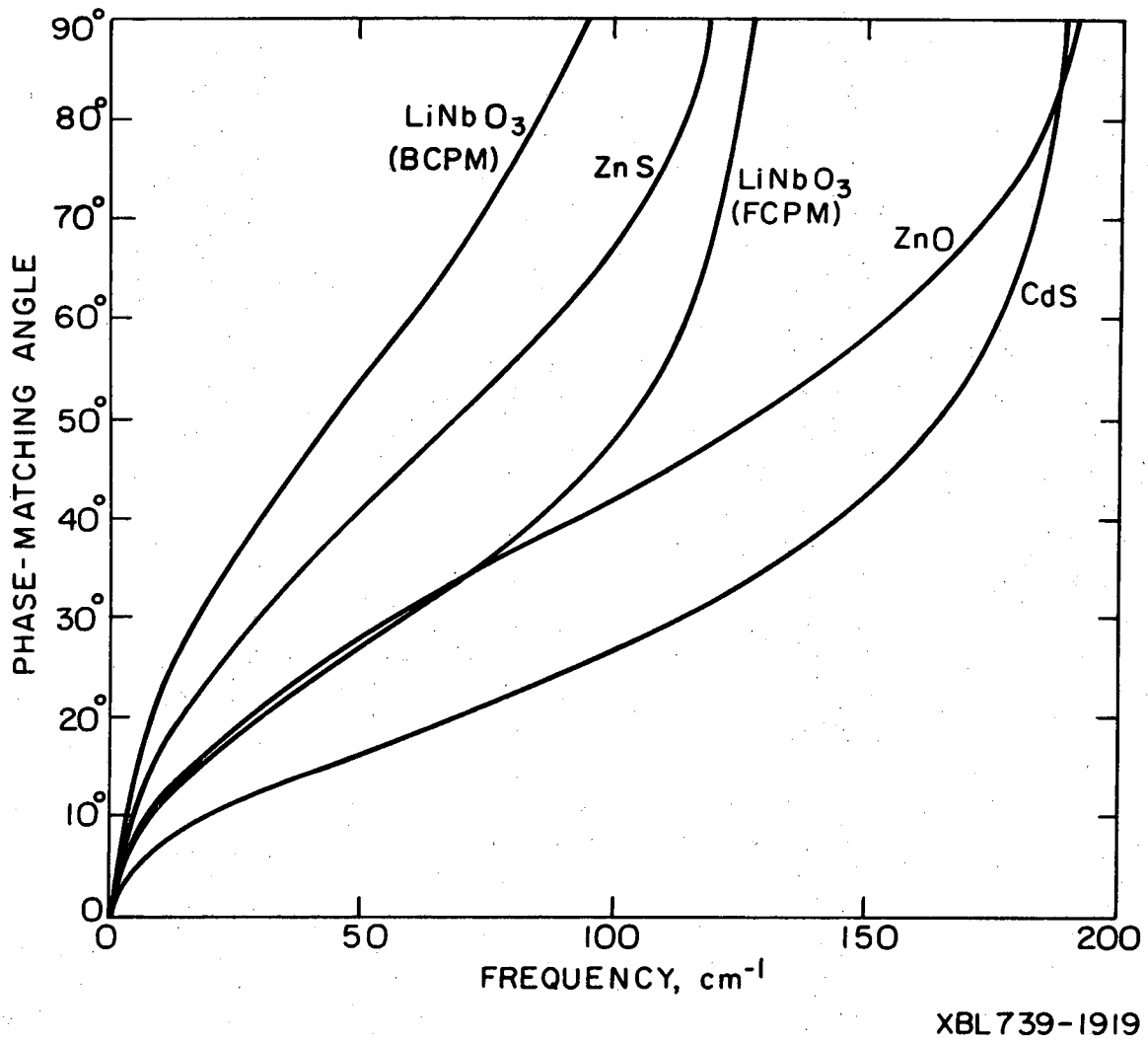
90°
80°
70°
60°
50°
40°
30°
20°
10°
0
PHASE-MATCHING ANGLE
LiNbO3
(BCPM)
ZnS
LiNbO3
(FCPM)
ZnO
CdS
0
50
100
150
200
FREQUENCY, cm-1
XBL739-1919

Fig. 14

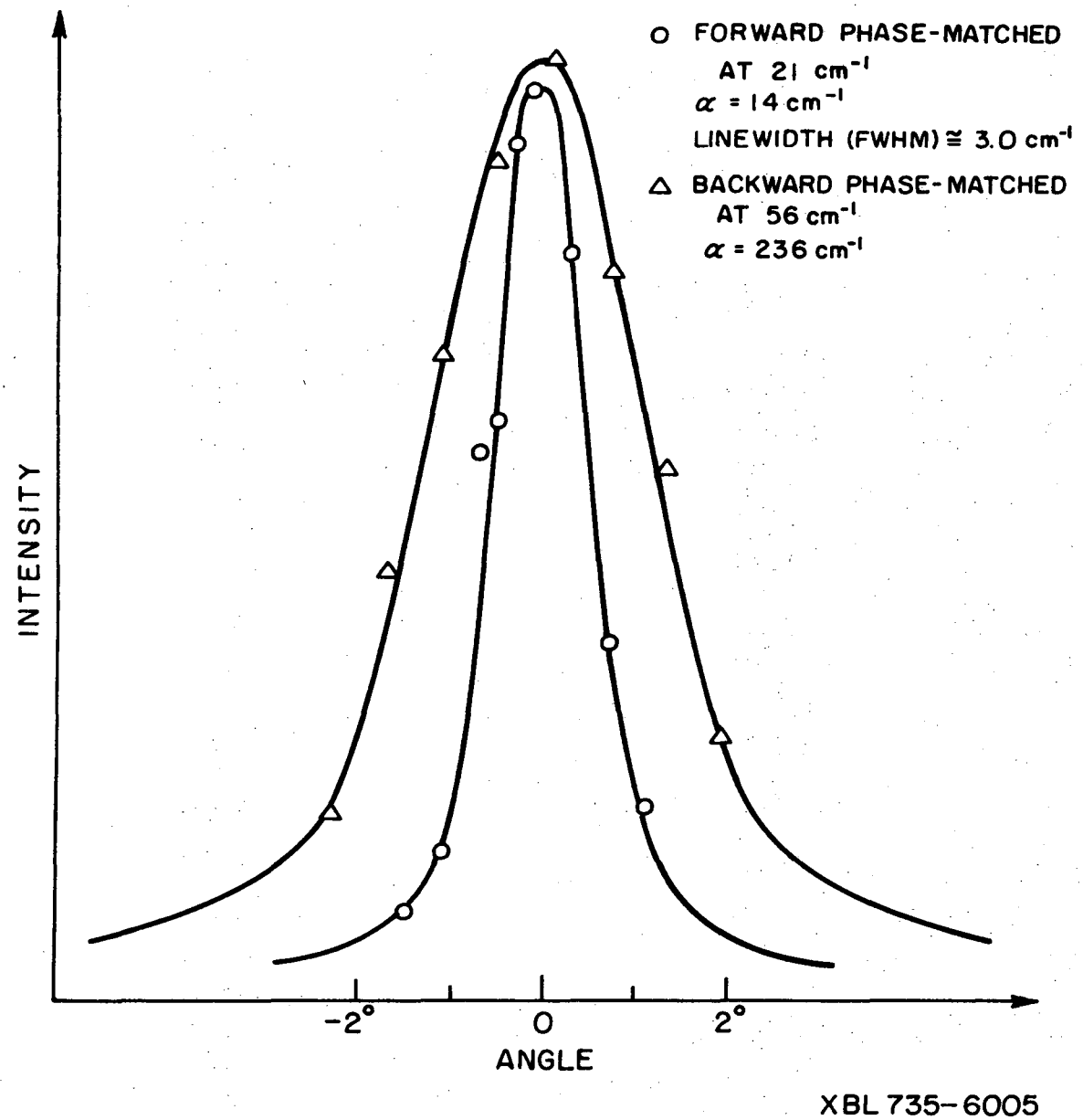
O FORWARD PHASE-MATCHED
AT 21 cm⁻¹
α = 14 cm⁻¹
LINEWIDTH (FWHM) ≅ 3.0 cm⁻¹
△ BACKWARD PHASE-MATCHED
AT 56 cm⁻¹
α = 236 cm⁻¹
INTENSITY
-2°
0
2°
ANGLE
XBL 735-6005

Fig. 15

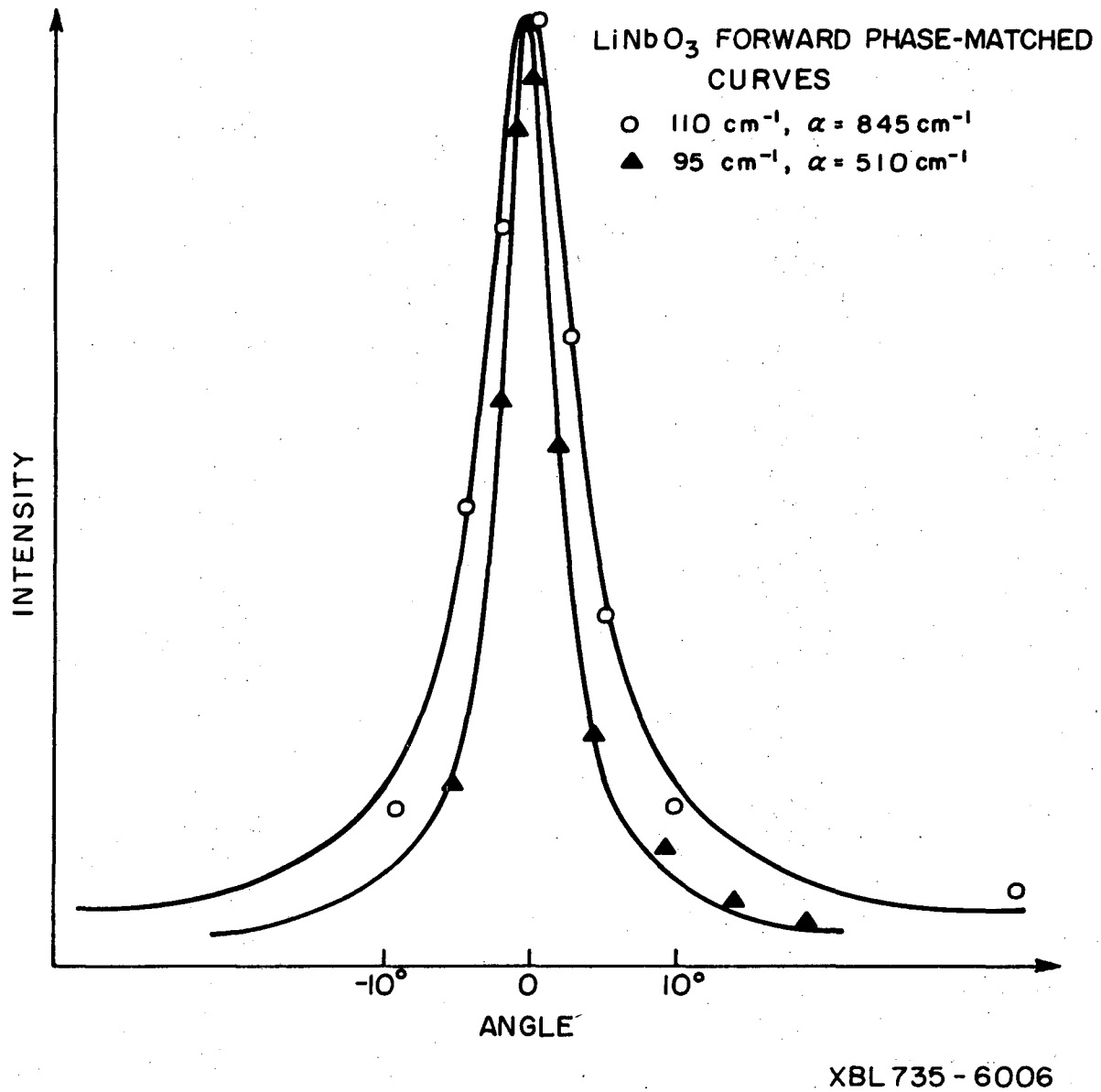
LiNbO3 FORWARD PHASE-MATCHED CURVES
110 cm-1, α = 845 cm-1
95 cm-1, α = 510 cm-1
INTENSITY
-10°
0
10°
ANGLE
XBL 735-6006

Fig. 16

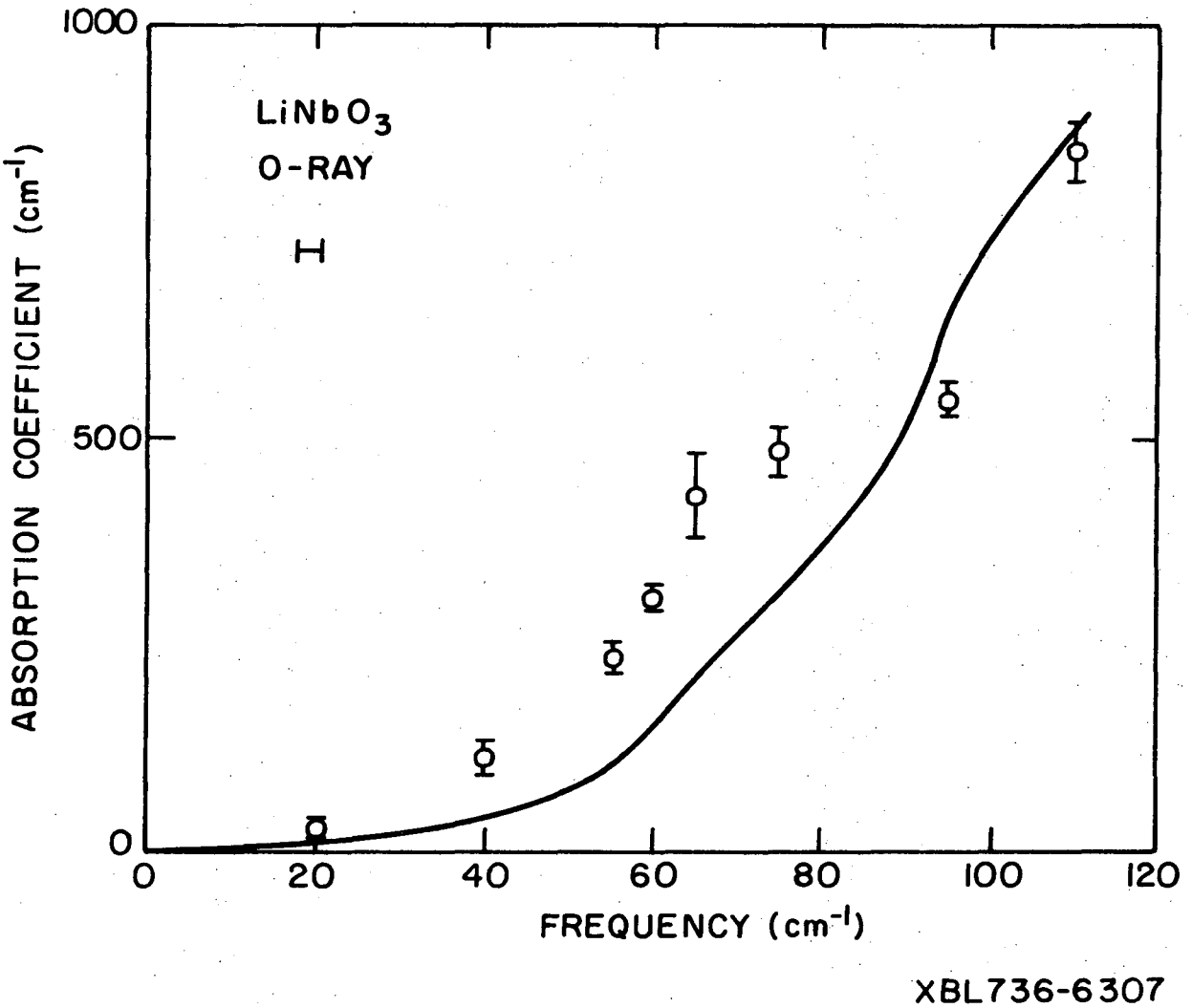
1000
500
0
ABSORPTION COEFFICIENT (cm⁻¹)
LiNbO3
O-RAY
0
20
40
60
80
100
120
FREQUENCY (cm⁻¹)
XBL736-6307

Fig. 17

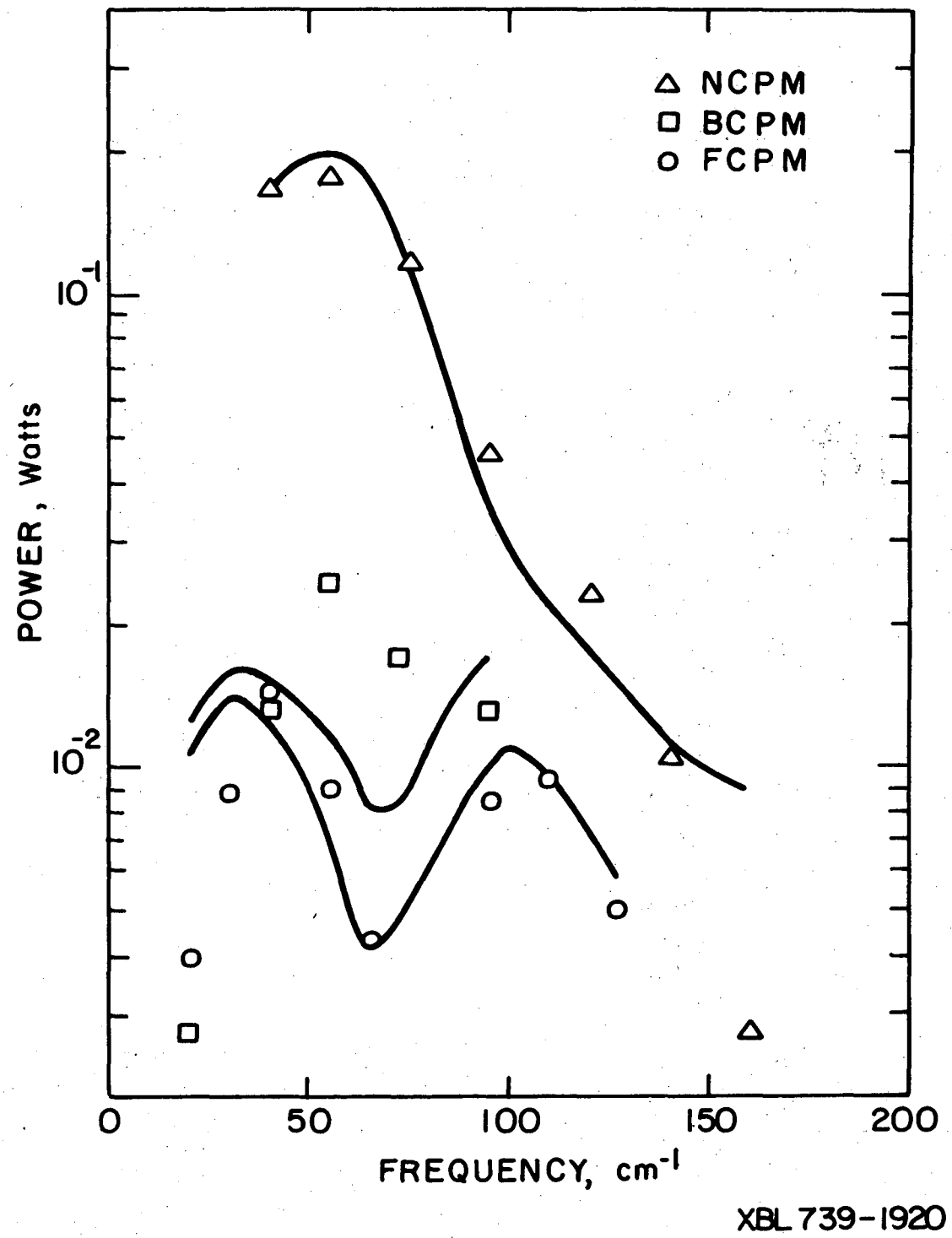
NCPM
BCPM
FCPM
10^{-1}
10^{-2}
POWER, Watts
0
50
100
150
200
FREQUENCY, cm^{-1}
XBL 739-1920

Fig. 18

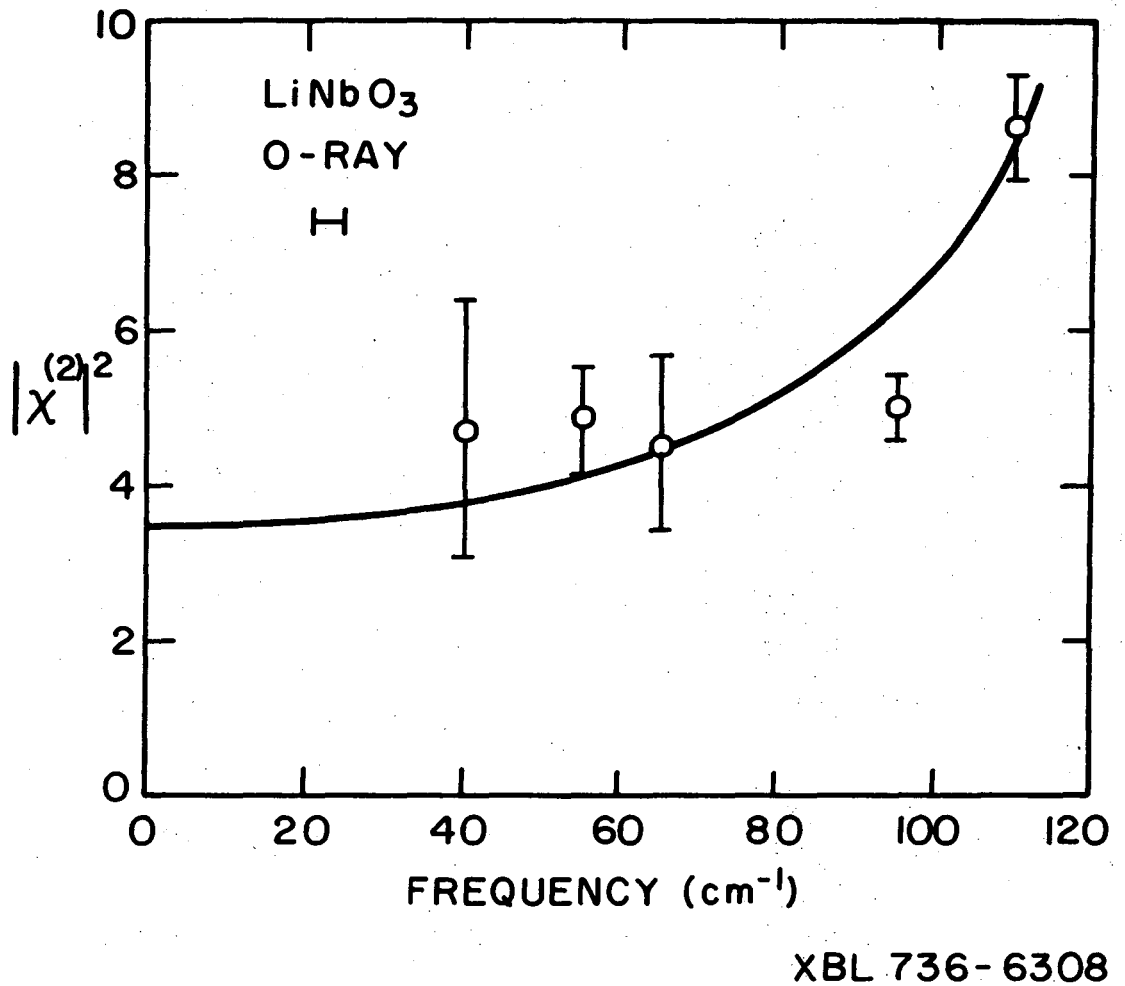
LiNbO3
O-RAY
H
$|\chi^{(2)}|^2$
0
2
4
6
8
10
0
20
40
60
80
100
120
FREQUENCY (cm^{-1})
XBL 736-6308

Fig. 19

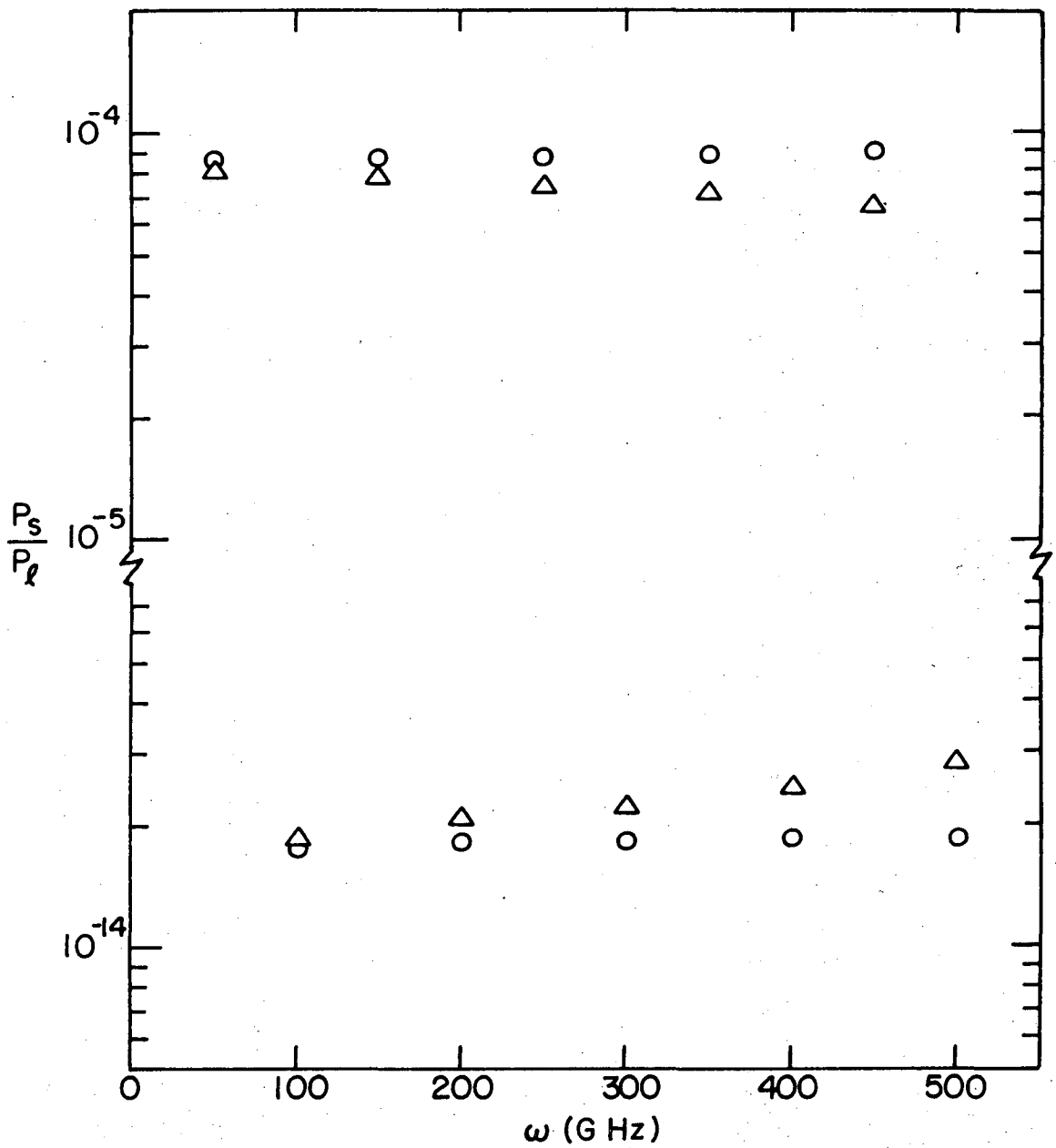

XBL 726-6467

Fig. 20

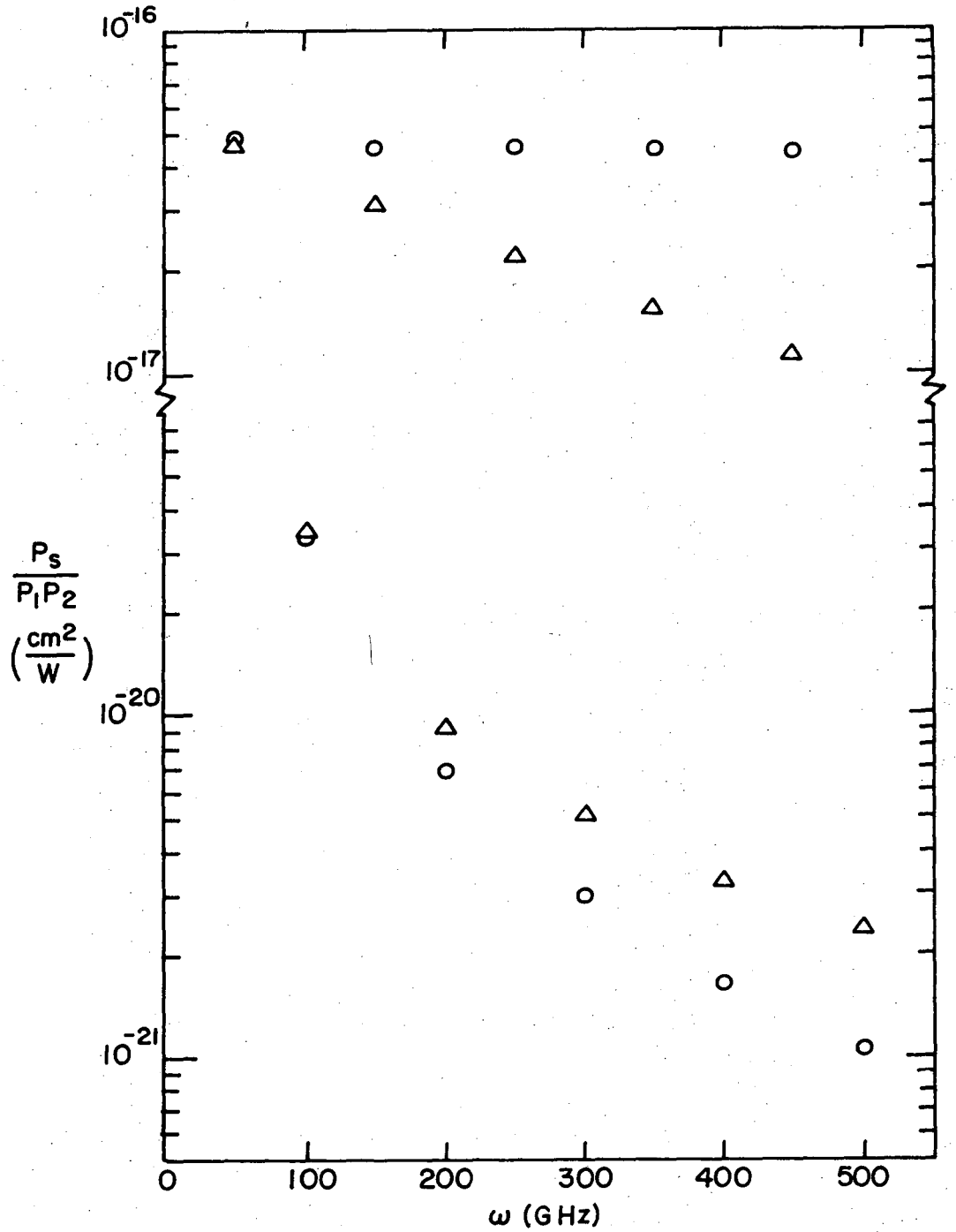

XBL726-6468

Fig. 21

LEGAL NOTICE

This report was prepared as an account of work sponsored by the United States Government. Neither the United States nor the United States Atomic Energy Commission, nor any of their employees, nor any of their contractors, subcontractors, or their employees, makes any warranty, express or implied, or assumes any legal liability or responsibility for the accuracy, completeness or usefulness of any information, apparatus, product or process disclosed, or represents that its use would not infringe privately owned rights.

TECHNICAL INFORMATION DIVISION
LAWRENCE BERKELEY LABORATORY
UNIVERSITY OF CALIFORNIA
BERKELEY, CALIFORNIA 94720